ENGINEERING THE SURFACES OF GROUP IV MATERIALS FOR ENERGY APPLICATIONS

by

Rohan P. Chaukulkar

A thesis submitted to the Faculty and the Board of Trustees of the Colorado School of Mines in partial fulfillment of the requirements for the degree of Doctor of Philosophy (Chemical and Biological Engineering).

Golden, Colorado

Date ____________________

Signed _______________________

Rohan P. Chaukulkar

Signed _______________________

Dr. Sumit Agarwal

Thesis Advisor

Signed _______________________

Dr. Pauls Stradins

Thesis Advisor

Golden, Colorado

Date ____________________

Signed _______________________

Dr. David W.M. Marr

Professor and Head

Department of Chemical and Biological Engineering

ABSTRACT

A majority of our energy needs today is met by fossil fuels. The combustion of fossil fuels leads to the release of greenhouse gases which adversely affect our environment. This has prompted significant efforts to harness the various sources of renewable energy available to us. Solar energy is the only source of renewable energy capable of meeting our ever-increasing energy demands. Of the various solar technologies, photovoltaic (PV) technology promises to be an attractive option for the generation of electricity due to no emissions of greenhouse gases and various additional socio-economic benefits. A major obstacle in the implementation of PV technology on a large scale is the cost. This has led to an increased interest in research directed towards reducing the cost of electricity generated through PV. Si based PV holds majority of the market share. Therefore, a major challenge in the field of PV is the reduction of cost of electricity generated via Si based PV technologies. This goal can be achieved by the development of high-efficiency solar cells based on Si. Surface passivation is one of the reasons often cited for low efficiencies observed in solar cells. Hence, as a part of the work completed in this dissertation, we have studied the surface passivation in *c*-Si solar cells.

Specifically, we have used infrared spectroscopy techniques and minority carrier lifetime measurements to study the mechanism of surface passivation of *c*-Si by Al_2O_3. The passivation of the Si surface via Al_2O_3, deposited by atomic layer deposition (ALD), is achieved by a reduction in the defect density at the interface (D_{it}) (chemical passivation) and an increase in the fixed negative charge (Q_f) associated with the Al_2O_3 films (field effect passivation). A post-deposition annealing step is required to achieve this high level of passivation. We have

investigated the effect of the annealing step in order to understand the mechanism of chemical passivation. Specifically, we have studied the role of H and O in the chemical passivation of *c*-Si by Al_2O_3. Our results indicate that it is the restructuring at the interface, and not the migration of H from Al_2O_3 to the *c*-Si interface, that contributes to the reduction in the interface defect density.

In addition to Al_2O_3, TiO_2 has also been proposed as a surface passivant for *c*-Si. TiO_2, due to its optical properties, has the added advantage of acting as an anti-reflection coating in addition to the surface passivation. Atomic layer deposition (ALD) technique is often used to deposit these TiO_2 thin films. However, the low growth per cycle observed for typical ALD processes makes it unfeasible to be used on a large scale. Therefore, we have developed a novel ALD chemistry for the deposition of TiO_2 with a high growth per cycle. We use a metal-alkoxide metal-chloride precursor combination to deposit the TiO_2 thin films wherein the metal-alkoxide acts as the oxygen source. We have used *in situ* IR spectroscopy to study the surface reaction mechanism during the deposition process. We found that the reaction follows a alkyl-tranfer mechanism over the range of 150-250 °C. The use of metal-alkoxide as the oxygen source would also potentially mitigate the problem of interfacial oxide formation and hence, enable deposition of TiO_2 on oxygen sensitive substrates.

Renewable energy sources such as solar energy, have an intermittent nature which increases the importance of an efficient energy storage system. Due to their high energy and power density, low self-discharge and maintenance, lithium-ion batteries (LIBs) are attractive candidates to meet this challenge. However, the LIB technology needs significant improvements before it can be implemented as an effective storage system. One of the factors which would improve the capacity of the LIB is the anode material. Group IV materials such as Si, Ge and Sn,

all have higher capacities than the current conventional anode material, graphite. The use of these materials as anodes in LIBs is however unfeasible due to the significant volume expansion these materials undergo upon lithiation. The volume expansion leads to electrode pulverization and a loss in battery capacity after just the first few charging and discharging cycles. A way to circumvent this issue is the use of nanomaterials. Specifically, carbon-coated Group IV nanomaterials have shown enhanced capacities as compared to graphite. To this end, we have developed a single-step technique to synthesize carbon-coated Si, Ge, and Sn nanoparticles. In this technique, we use two non-thermal plasmas in series to first synthesize the nanoparticles, and then coat them with carbon. We have studied the effects of varying the plasma parameters on the nature of the coating we employ on these nanoparticles. We have shown that the use of two plasmas allow us to independently control the synthesis and coating of these nanoparticles.

Efficient use of energy also contributes to the reduction of fossil fuel emissions. Artificial lighting consumes a significant portion of the electricity we generate. Hence the use of LEDs, which have been shown to be more efficient that traditional lighting sources, can greatly impact the fossil fuel emissions. Silicon carbide, due to its high band-gap has been proposed as a material for the manufacture of blue LEDs. The use of nanomaterials has been shown to enhance the luminescence properties of silicon carbide. Therefore, as a part of the work completed in this dissertation we propose a low-temperature technique to synthesize silicon carbide nanoparticles. We use a dual-plasma setup similar to the one used to synthesize the carbon-coated Group IV nanoparticles. The Si nanoparticles are synthesized in the upstream plasma and then carburized in the downstream plasma to form crystalline silicon carbide nanoparticles.

Table of Contents

ABSTRACT iii

LIST OF FIGURES ix

ACKNOWLEDGEMENT xvi

CHAPTER 1 INTRODUCTION 1

1.1 WHY IS SOLAR ENERGY IMPORTANT? 1

1.1.1 CRYSTALLINE-SI PV FOR ELECTRICITY GENERATION 2

1.1.2 SURFACE PASSIVATION IN *C*-SI PVS 3

1.2 STORAGE AND EFFICIENT USE OF ELECTRICAL ENERGY 7

1.2.1 LI-ION BATTERIES 7

1.2.2 GROUP IV NANOSTRUCTURES IN LIBS 8

1.2.3 EFFICIENT USE OF ELECTRICAL ENERGY 9

1.3 REFERENCES 10

CHAPTER 2 MECHANISM OF CHEMICAL PASSIVATION OF *C*-SI BY AL2O3 STUDIED USING *IN SITU* INFRARED SPECTROSCOPY 17

2.1 INTRODUCTION 18

2.2 EXPERIMENTAL SETUP 20

2.3 RESULTS AND DISCUSSION 23

2.4 CONCLUSIONS 26

2.5 ACKNOWLEDGEMENTS 26

2.6 REFERENCES 26

CHAPTER 3 ATOMIC LAYER DEPOSITION OF TITANIUM DIOXIDE USING TITANIUM TETRACHLORIDE AND TITANIUM TETRAISOPROPOXIDE AS PRECURSORS 29

3.1 INTRODUCTION 30

3.2 EXPERIMENTAL DETAILS 32

3.3 RESULTS AND DISCUSSION 35

3.4 CONCLUSIONS 41

3.5 ACKNOWLEDGEMENTS 42

3.6 REFERENCES 42

CHAPTER 4 SINGLE-STEP PLASMA SYNTHESIS OF CARBON-COATED SILICON NANOPARTICLES 46

4.1 INTRODUCTION 47
4.2 EXPERIMENTAL DETAILS 50
4.2.1 PLASMA SYNTHESIS SETUP 50
4.2.2 PLASMA AND SURFACE DIAGNOSTICS 51
4.3 RESULTS AND DISCUSSION 53
4.4 CONCLUSIONS 66
4.5 ACKNOWLEDGEMENTS 67
4.6 REFERENCES 67
CHAPTER 5 PLASMA-ASSISTED SYNTHESIS OF CARBON-COATED GE AND SN NANOPARTICLES 75
5.1 INTRODUCTION 76
5.2 EXPERIMENTAL SETUP 78
5.2.1 NANOPARTICLE SYNTHESIS SETUP 78
5.2.2 SYNTHESIS OF GE@C NPS 79
5.2.2 SYNTHESIS OF SN@C NPS 79
5.2.2 NP CHARACTERIZATION 80
5.3 RESULTS AND DISCUSSION 81
5.4 CONCLUSIONS 86
5.5 ACKNOWLEDGEMENTS 87
5.6 REFERENCES 87
CHAPTER 6 SINGLE-STEP NON-THERMAL PLASMA SYNTHESIS OF 3C-SIC NANOPARTICLES 91
6.1 INTRODUCTION 92
6.2 EXPERIMENTAL SETUP 94
6.3 RESULTS 97
6.4 DISCUSSION 99
6.5 SUMMARY 103
6.6 ACKNOWLEDGEMENTS 104
6.7 REFERENCES 104
CHAPTER 7 CONCLUSIONS AND FUTURE WORK 111
7.1 CHEMICAL PASSIVATION OF *C*-SI BY AL_2O_3 111

7.2 ALD OF TIO_2 USING METAL-ALKOXIDE AS THE OXYGEN SOURCE 112

7.3 SINGLE-STEP SYNTHESIS OF CARBON-COATED GROUP IV NANOPARTICLES 112

APPENDIX A QUANTITATIVE XRD ANALYSIS 114

APPENDIX B LOW TEMPERATURE HYDROGEN PLASMA-ASSISTED ATOMIC LAYER DEPOSITION OF COPPER STUDIED USING IN SITU INFRARED REFLECTION ABSORPTION SPECTROSCOPY 117

B.1 INTRODUCTION 118

B.2 EXPERIMENTAL DETAILS 121

B.2.1 INFRARED REFLECTION ABSORPTION SPECTROSCOPY 121

B.2.2 IN SITU IRAS SETUP 127

B.2.3 CU ATOMIC LAYER DEPOSITION 128

B.3 RESULTS AND DISCUSSION 130

B.4 CONCLUSIONS 136

B.5 ACKNOWLEDGEMENTS 137

B.6 REFERENCES 137

LIST OF FIGURES

Figure 1.1: Schematic representation of PERT architecture based on *n*-type Si 4

Figure 2.2: Schematic representation of Li-ion battery 7

Figure 2.1: Cross section schematic representation of the multiple internal reflections of the IR beam in the IRC and the decay of the electric field associated with IR beam. (b) IR difference spectrum of the SiH_x region for a H-terminated Si IRC. The spectrum is deconvoluted to show the various silicon hydrides present on the surface. The deconvolution was performed using Gaussian line shapes. 20

Figure 2.2: (a) IR difference spectrum collected after the deposition of Al_2O_3 on H-terminated Si IRC (b) IR difference spectrum collected after annealing the Al_2O_3 covered IRC at 400 °C in a N2 atmosphere for 15 minutes. Inset is the zoomed in view of the SiH_x region which shows the increase in absorbance in the region assigned to the $OSiH_x$ species 22

Figure 2.3: IR difference spectra collected before and after anneal for $Si/SiO_2/Al_2O_3$ test structures.. 24

Figure 3.1: Schematic representation of the reactions during TiO_2 ALD using TTIP and $TiCl_4$. (a) The alkyl-transfer process, which involves a simple ligand-exchange reaction of the surface isopropoxy ligands with $TiCl_4$ to produce isopropyl chloride as the reaction product. (b) The β-hydride elimination process, which proceeds via decomposition of the surface isopropoxy ligands to create a hydroxyl-terminated surface followed by reaction of $TiCl_4$ to produce HCl as the reaction product. In both cases, the Cl-terminated surface obtained after the $TiCl_4$ cycle reacts with TTIP to produce isopropyl chloride, thus restoring the initial isopropoxy-ligand-terminated surface. Reaction (b) is more likely to occur at $\geq$ 250 °C, which is reported to be the temperature for the onset of TTIP thermal decomposition...31

Figure 3.2: IR difference spectra showing the absorbance due to the various surface species involved in the ligand exchange reactions during TTIP (black) and $TiCl_4$ (red) half-reaction cycles at a substrate temperature of (a) 150, (b) 175 and (c) 200 °C. The almost identical change in absorbance during the two half-reaction cycles suggests a one-to-one ligand-exchange characteristic of an ALD process. 34

Figure 3.3: IR difference spectra showing the absorbance due to the various surface species involved in the ligand exchange reactions during TTIP (black) and $TiCl_4$ (red) half-reaction cycles at a substrate temperature of (a) 150, (b) 175 and (c) 200 °C. The almost identical change in absorbance during the two half-reaction cycles suggests a one-to-one ligand-exchange characteristic of an ALD process. 36

Figure 3.4: High-resolution XPS scans of TiO_2 films deposited via ALD. (a) Ti 2p, O 1s, and (b) Cl 2p regions for a film grown at 200 °C. (c) The Cl 2p region for a film grown at 225 °C. The O 1s peak was deconvoluted using Gaussian-Lorentzian (GL) peaks at 530.0 (red) and 531.4 (blue) eV corresponding to O boned to Ti and C, respectively. The Cl 2p region was fitted with four GL peaks corresponding to Cl bonded to Ti at 198.6 and 200.2 eV (red) and Cl bonded to C at 200.4 and 202.0 eV (blue). The energy scale in all the spectra was calibrated with respect to the adventitious C 1s peak at 285.0 eV.. 37

Figure 3.5: UV-Vis transmission spectra for TiO_2 films deposited at a substrate temperature of 200 (red) and 225 °C (black) plotted as (a) $(Ahv)^{1/2}$ and (b) $(Ahv)^2$ versus hv to obtain the indirect and direct band gaps, respectively. At both temperatures, the indirect and direct band gaps were ~3.0 and ~3.8 eV, respectively, which are close to the values for amorphous TiO_2 reported in the literature..39

Figure 4.1: Schematic of the tubular reactor equipped with two radio-frequency, capacitively-coupled plasma sources used to synthesize carbon-coated *c*-Si NPs. The *c*-Si NPs were synthesized in the upstream plasma using SiH_4 heavily diluted in Ar. C_2H_2 was injected into the tube beyond the afterglow region of the SiH_4/Ar plasma. The as-synthesized *c*-Si NPs were transported by gas flow to the downstream C_2H_2 plasma,

where they were coated in flight with amorphous carbon and collected onto a ZnSe internal reflection crystal for characterization using surface infrared spectroscopy ...49

Figure 4.2: Optical emission spectra showing the effect of C_2H_2 injection on the upstream *c*-Si NP synthesis plasma. The emission intensities for the Ar and C_2 radical lines at 750.4 and 516.5 nm, respectively, were monitored in the upstream plasma prior to and after downstream C_2H_2 injection. 51

Figure 4.3: *In situ* infrared difference spectra for carbon-coated *c*-Si NPs grown at (a) 40 and (b) 90 W rf power to the downstream C_2H_2 plasma. 53

Figure 4.4: Infrared difference spectra showing the CH_x stretching region for carbon-coated *c*-Si NPs synthesized at (a) 40 W, (b) 60 W, and (c) 90 W rf power to the downstream C_2H_2 plasma. The spectra were deconvoluted with four Gaussian line shapes. The ratio of the integrated absorbance of the sp^2-hybridized carbon to that of the sp^3-hybridized carbon increased with increasing downstream plasma rf power. 55

Figure 4.5: Normalized PL spectra for uncoated (black) and carbon-coated (red) c-Si NPs. The carbon coating was accompanied with the formation of a 3C-SiC at the c-Si/a-C interface, which led to the consumption of surface Si, and a reduction in the size of the NP core. In the quantum confinement regime, this causes a blue-shift in the PL peak position 57

Figure 4.6: XRD patterns for the *c*-Si NPs grown at (a) 0, (b) 105, and (c) 135 W rf power to the downstream C_2H_2 plasma, but identical upstream plasma conditions. As the C_2H_2 plasma rf power was increased, the amount of 3C-SiC formed at the *c*-Si/*a*-C interface increased, which is indicated by the increase in the relative intensity of the 3C-SiC (111) diffraction peak compared to the Si (111) diffraction peak. 59

Figure 4.7. (a) Raman spectrum showing the presence of *c*-Si NPs, *a*-C, and 3C-SiC for carbon-coated *c*-Si NPs grown at 135 W rf power to the C_2H_2 plasma. (b) The *c*-Si region was fit using a Lorentzian line shape centered at 510 cm^{-1}, while the shoulder attributed to *a*-C, was fit with a Gaussian line shape centered at ~450 cm^{-1}. The *a*-C

region was fit with a Lorentzian centered at ~1345 cm^{-1} (D band), and a Breit-Wigner-Fano line shape centered at ~1576 cm^{-1} (G band). 63

Figure 4.8. TEM images of carbon-coated *c*-Si NPs grown at 135 W rf power to the downstream C_2H_2 plasma. Image (b), which is a zoomed-in view of a particle that was observed in image (a), clearly shows a *c*-Si core of ~3.7 nm with a ~1.5-nm-thick coating. 64

Figure 4.9. High resolution XPS scan of the Si 2p region for carbon-coated *c*-Si NPs synthesized at 135 W rf power to the C_2H_2 plasma...65

Figure 5.3: Schematic of the tubular quartz reactor used to synthesize *a*-C:H coated Ge and Sn NPs. The Ge and Sn NPs were synthesized in the upstream plasma using $GeCl_4$ and $SnCl_4$, respectively, diluted in a H_2-Ar gas mixture. The NPs are coated with *a*-C:H in the downstream C_2H_2-Ar plasma. 77

Figure 5.4: Infrared difference spectra of *a*-C coated Ge NPs synthesized at a downstream rf plasma power of (a) 60 W, and (b) 90 W. 80

Figure 5.5: Infrared difference spectra of the CH_x stretching region for *a*-C coated Ge NPs synthesized at a downstream rf plasma power of (a) 60 W, and (b) 90 W. The peaks were fit using a Gaussian line shape. The ratio of the integrated absorbance of the sp^2 region to that of the sp^3 region was found to increase with an increase in downstream plasma power.. 83

Figure 5.6: X-ray diffraction pattern of *a*-C coated *c*-Ge NPs synthesized at a downstream plasma power of 90 W. The position of the peaks corresponding to the (111), (220) and (311) crystallographic planes is similar to that in bulk *c*-Ge. The size of the NPs was estimated using Scherrer analysis. 84

Figure 7.5: X-ray diffraction pattern of *a*-C coated 10 nm *c*-Sn NPs. Scherrer analysis was used to estimate the size of the NPs. 85

Figure 5.8. Raman spectrum of the *a*-C coating around the Sn NPs, synthesized at a downstream rf plasma power of 90 W. The two peaks were fit using the Lorentzian line shape

centered at ~1390 cm^{-1} (D band), and a Breit-Wigner-Fano line shape centered at ~1585 cm^{-1} (G band)...86

Figure 6.9: Schematic of the quartz tube plasma reactor used for the synthesis of 3C-SiC NPs using SiH_4 and C_2H_2 as precursors. The reactor is equipped with two capacitively-coupled rf plasma sources. *c*-Si NPs grow in the upstream SiH_4/Ar plasma, and are carburized in the downstream C_2H_2/Ar plasma to 3C-SiC NPs. 95

Figure 6.10: Infrared difference spectrum for 3C-SiC NPs. The formation of SiC is indicated by the transverse optical phonon mode of SiC in the 750-950 cm^{-1} region. Various vibrational modes assigned to the C-C and CH_x bonds show that an *a*-C:H coating exists around the NPs with a partial alkenyl termination. The structure of the *a*-C:H coating can be further characterized based on the hybridization of the C atoms as shown in the inset...97

Figure 6.11: XRD pattern for *a*-C:H-coated 3C-SiC NPs. The (111) and (220) crystallographic planes of 3C-SiC indicate that the NPs are crystalline. The size of the NPs was estimated to be ~4.2 nm using Scherrer analysis. Inset shows the peak fit for the (111) peak using Gaussian line shapes. The sharp peak is due to the (200) reflection for the Si(100) wafer used as the substrate..98

Figure 6.12: High-resolution XPS scan of the Si 2p region for *a*-C:H-coated 3C-SiC NPs synthesized using the dual-plasma setup.. 100

Figure 6.5: TEM images of *a*-C:H coated 3C-SiC nanoparticles. Image (b), which is a zoomed in view of a particle in image (a), shows a ~4.4 nm 3C-SiC core with a ~1.3 nm thick *a*-C:H coating.. 102

Figure B.1. (a) Schematic showing the *s* and *p* components of the electric field associated with the incident and reflected light. (b) A plot of the reflectance, *R*, as a function of the angle of incidence, ϕ, using the expression in Eqns. 3 and 4 with $n = 3$ and $k = 30$. The plot in (b) shows that $R_s \approx 1$ for all angles of incidence, while R_p shows a minimum for near-grazing values of □. (c) The graph shows phase shift, *d*, upon reflection for the *s* and *p* polarized light plotted as a function of the angle of

incidence, ϕ, using Eqns. 5 and 6. The *s* component of the electric field undergoes an almost constant phase shift of ~180° resulting in a negligible electric field parallel to the surface for all angles of incidence. 119

Figure B.2. (a) A plot of the ratio of the perpendicular component of the electric field to the total incident electric field for the *p* component of light ($E_p^{\perp}/E_{ip}$) as a function of the angle of incidence, ϕ. The quantity $(E_p^{\perp}/E_{ip})^2\sec\phi$, which is proportional to the experimentally-observed infrared absorbance, is also plotted as a function of ϕ. (b) Absorbance or change in reflectance, $\Delta R/R$ plotted as a function of the angle of incidence, ϕ, for an Al (n = 6.8, k = 32) film coated with ~10 nm of Al_2O_3 (n = 1.3, k = 0.1).. 121

Figure B.3. (a) Schematic top view of the reactor equipped with the *in situ* IRAS setup. The chamber is also equipped with a remote inductively coupled plasma source. The infrared beam from the spectrometer is focused onto the first substrate stage at grazing incidence. The reflected beam from the first mirror is then collected and focused onto a MCT-A detector after reflection from a second redirecting mirror. (b) A zoomed-in view of the schematic showing the substrate stage and the diverting mirror. Both reflecting surfaces can be heated using the cartridge heaters mounted inside the stages.. 126

Figure B.4. Infrared difference spectra showing the absorbance change for the $Cu(hfac)_2$ half-reaction cycle collected (a) after a 10-s precursor exposure, (b) after an additional 10-s precursor exposure and (c) after a 30-s purge-step using a gas mixture of Ar and H_2. The identical absorbance in the three spectra suggests self-saturating chemisorption of $Cu(hfac)_2$ onto the substrate, and the lack of reactivity between surface-chemisorbed $Cu(hfac)_2$ and molecular H_2 at a substrate temperature of 80 °C. The inset in Fig. 4 shows the CH bending region in detail. 129

Figure B.5. Infrared difference spectra showing the change in absorbance due to different surface

species in the two half-reaction cycles during the ALD of Cu using $Cu(hfac)_2$ and a H_2 plasma. The almost identical change in absorbance during the two half-reaction cycles suggests a one-to-one ligand exchange typical of an ALD process...............131

Figure B.6. Infrared difference spectra showing the absorbance change for the $Cu(hfac)_2$ (black) and the D_2 plasma (red) half-reaction cycles at a substrate temperature of 80 °C.....132

Figure B.7. Infrared difference spectra showing the absorbance change for $Cu(hfac)_2$ half-reaction cycles collected following 80 complete ALD cycles. The spectra (a), (b), (c) and (d) are for the 81st, 82nd, 83rd, and 84th $Cu(hfac)_2$ half-reaction cycle, respectively. Similar absorbance in all the spectra indicates that IRAS can be used to study the surface reactions during ALD of metals well beyond the initial nucleation stage. The corresponding spectra for the H_2-plasma half-reaction cycle show a one-to-one ligand exchange, and are not shown here for clarity.. 133

ACKNOWLEDGEMENT

These past 5 years have been a tremendous learning experience for me, and for that I would like to sincerely thank my advisors, Sumit Agarwal and Pauls Stradins, for all their help and guidance. They have always been supportive and encouraging at every step of my PhD work, and it has been a pleasure and an honor working under them.

I would also like to thank my coworkers at Colorado School of Mines and those that visited our lab from the Eindhoven University of Technology. A special thanks to the members of the Si group at National Renewable Energy Laboratory with whom I had the pleasure of working for nearly a year. All of them were extremely helpful, especially with the various equipment trainings, and always accommodated my work in spite of their busy schedules.

I would like to thank my family and friends for their love and support. They have always believed in me and encouraged me which has helped me a lot throughout my PhD work.

This work was financially supported by the NSF CAREER program (Grant No. CBET-0846923), the Colorado Revolutionary Solar Photoconversion, the NCPV Fellowship Program and U.S. Department of Energy, Office of Energy Efficiency and Renewable Energy, under Contract No. DE-AC36-08GO28308 with the National Renewable Energy Laboratory.

CHAPTER 1

INTRODUCTION

This chapter outlines the motivation and scope of the research completed in this Ph.D. dissertation related to the generation, storage, and efficient use of renewable energy. In particular, we focus on Group IV semiconductors in various energy-related applications.

1.1 Why is solar energy important?

As mankind continues to make significant progress in the fields of science and technology, there is an ever-increasing demand for a stable, reliable supply of energy.[1] Indeed, the *International Energy Outlook 2013 (IEO2013)* projects a 56% increase in world energy-consumption between 2010 and 2040. Currently, combustion of fossil fuels remains the primary source for generation of energy around the world.[2] Combustion of fossil fuels leads to the release of greenhouse gases such as CO_2, which adversely affect the climate system.[1,3,4] The growth rate for emissions from combustion of fossil fuels increased from 1.5%/year over 1980-2000 to 3%/year over 2000-2012.[5] With continued efforts towards expanding fossil fuel extractions, the fossil fuel emissions will continue to rise leading to global warming and adverse effects on sea levels and weather patterns.[2,5] Therefore, the United Nations Framework Convention on Climate Change has called for the terawatt challenge, an effort to supply 30 TW of carbon-free power by 2050.[2,4] Solar energy is the most abundant source of energy, and the only renewable energy source amongst wind, hydroelectric, biomass, and geothermal, to be capable of meeting the estimated energy requirements.[2,6] Of the various solar technologies,

photovoltaics (PV) is of particular interest for the generation of electricity due to no emission of greenhouse gases, and scalability.[6–8] Additionally, PV also has some socio-economic benefits like reclamation of degraded land, increase in regional energy independence, and acceleration of rural electrification in developing countries.[6,8] Currently, one of the major drawbacks of the PV technology is the high cost of electricity generation. The price for electricity generated by PV is about 2-5 times higher than the conventional grid supplied electricity.[2,7–10] Continued research in the field targets the price of electricity generated by PV to be reduced to ~US $ 1/watt by 2020.[2,7] Increasing the conversion efficiency, reducing the material consumption, application of cheaper materials etc, are some of the ways this goal can be achieved.

1.1.1 Crystalline-Si PV for electricity generation

Si is nontoxic and one of the most abundant elements on Earth. Therefore, inspite of the recent advances in thin-film PV technologies, such as CdTe or CuInGeSe, crystalline Si based PV technologies still hold the majority of market share in the PV industry. [2,8,11] Si based PVs are manufactured from either single-crystal or polycrystalline Si substrates. Due to the low quality of the substrate wafers owing to the high dislocation and impurity densities, polycrystalline Si solar cells generally demonstrate lower efficiencies as compared to their single-crystal counterparts.[11] Single-crystal Si PVs are manufactured using either *n*- or *p*-type substrate wafers. High-lifetime substrate wafers are cut from high purity ingots grown either by the Czochralski (CZ) or the float-zone (FZ) technique. *p*-type Si grown by the CZ method, which has been commonly used in the industry, may suffer from light-induced degradation in bulk-lifetime by the formation of boron-oxygen complexes.[11] Although the mechanism for this degradation in bulk-lifetime is well understood, industrial scale processes to mitigate the issue have not yet been developed. On the

other hand, *p*-type Si grown by the FZ method is not susceptible to this degradation in bulk-lifetime, but the high cost of the FZ technique makes it unfeasible to use on an industrial scale. Therefore, *n*-type CZ wafers are preferred for high-efficiency solar cells.[9,11] The price of the Si substrate still remains one of the biggest factors which influences the cost of electricity generation. Therefore, it is imperative to manufacture high-efficiency solar cells to reach the goal of low-cost electricity via PV. William Shockley and Hans Queisser calculated that the maximum theoretical efficiency a single-juntion Si solar cell can achieve is ~29%.[12] This limit in efficiency is due to the inherent bandgap observed in semiconductors. Absorption of photons in the solar spectrum with energies higher than the bandgap leads to thermalization losses while the photons with energy less than the bandgap are not absorbed. Radiative and Auger recombination losses further limit the cell efficiency. While laboratory-based Si solar cells have demonstrated efficiencies close to 25%, industrially manufactured cell efficiencies lag considerably, and are usually over the range of 16-18%.[11,13,14] Therefore, the current challenge is to reduce this difference in solar cell efficiencies. This can be achieved by improving light trapping, emitter profile, metallization process or the surface passivation quality.[14] As part of the work completed in this dissertation, we have studied the surface passivation with an aim to improve the solar cell efficiency.

1.1.2 Surface Passivation in *c*-Si PVs

Figure 1.1 shows a schematic representation of a proposed high-efficiency solar cell architecture known as passivated emitter, rear totally diffused (PERT) solar cell based on a *n*-type Si substrate.[15] The efficiency of light-trapping is increased by applying an antireflection coating on the front side. The front side is a p^+ emitter which requires surface passivation. This

surface passivation layer is important since recombination losses at defects on the p^+ emitter surface significantly impacts the cell efficiency. The most common passivants for Si solar cells are SiO_2 and SiN_x.[14,16] Recently, Al_2O_3 deposited by atomic layer deposition (ALD) has been shown to be an excellent alternative. The effectiveness of this passivation layer is attributed to a combination of chemical and field-effect passivation.[17–19] A key difference is that while most other dielectrics like SiO_2 and SiN_x store positive charge at the interface with Si, Al_2O_3 forms fixed negative charges with a density of ~10^{12}–10^{13} cm^{-2}.[17] Si surfaces passivated with Al_2O_3 show low surface recombination velocities, (S_{eff} < 5 cm/s),[17] but this effect is only observed after a post-deposition annealing step carried out at ~400 ºC.[17] It has been shown that annealing reduces the interface defect density, D_{it} (chemical passivation), and increases the fixed negative charge Q_f (field-effect passivation).[20]

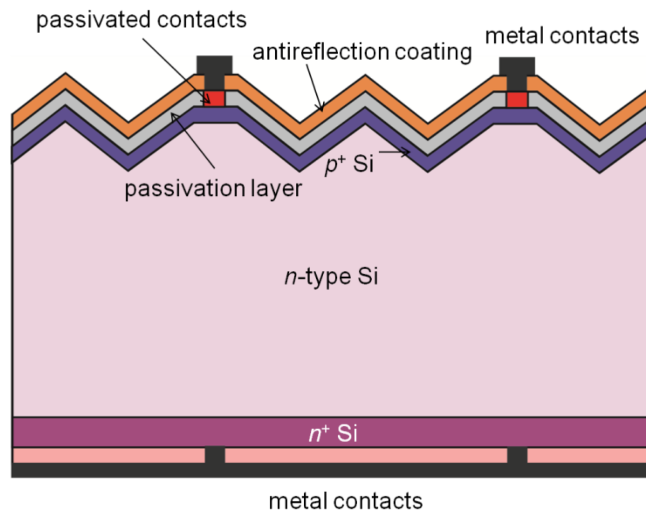

Figure 1.1. Schematic representation of PERT architecture based on *n*-type Si

The specific focus of this part of the dissertation was the study of the chemical passivation of *c*-Si by Al_2O_3 deposited by ALD. There have been numerous reports on the mechanism for chemical passivaiton of *c*-Si by Al_2O_3.[21–23] The post-deposition annealing step has been shown to lead to the formation of an interfacial SiO_x layer.[18,24] One theory suggests, that during the annealing step, the restructuring at the interface to form the interfacial SiO_x is accompanied by the migration of H from the Al_2O_3 to the *c*-Si interface. The H atoms passivate Si dangling bonds at the interface thereby reducing the D_{it}.[17,21,22] On the other hand some reports in literature suggest that since the as-deposited *c*-Si/Al_2O_3 interface resembles a low-temperature *c*-Si/SiO_2 interface, an oxygen environment is needed during the annealing step to improve the interface quality.[23,25] This suggests that the mechanism of chemical passivation of *c*-Si by Al_2O_3 may not be completely understood. This motivated us to study the chemical passivation mechanism using *in situ* attenuated total reflection Fourier transform infrared (ATR-FTIR) spectroscopy. Studies were carried out on high-lifetime Si internal reflection crystals (IRCs). The use of these Si IRCs provided us with a unique opportunity to correlate the observed changes in the passivation quality with the corresponding changes observed in the chemical composition of *c*-Si/Al_2O_3 interface as the IRC undergoes different processing steps. The ATR-FTIR spectroscopy setup provides us with a sub-monolayer sensitivity and enabled us to study the chemical composition of the bulk of the Al_2O_3 films in addition to the *c*-Si/Al_2O_3 interface. The detailed results of the study are presented in Chapter 2.

As mentioned above, efficient light management is essential for high efficiency solar cells. The refractive index of Al_2O_3 thin films (~1.6) makes it unsuitable for efficient light trapping.[26] Therefore, it requires an additional anti-reflection coating (Fig. 1), usually SiN_x which adds additional steps in the manufacturing process. TiO_2 due to its high refractive index (~2.3)

has been proposed as an anti-reflection coating. TiO_2 has also been shown to provide decent surface passivation for *c*-Si.[27–29] Thus, the use of TiO_2 thin films may simultaneously enable surface passivation and light trapping. Additionally, Al_2O_3/TiO_2 stacks have also been investigated for the passivation of *c*-Si.[26] ALD is increasingly being used to deposit these thin films since it provides the ability to deposit excellent quality pin-hole-free films with high conformality.[30,31] One of the drawbacks of the ALD process is the low growth per cycle (GPC) of the films which makes it unfeasible to grow thick films needed for antireflection coatings. TiO_2 films grown by thermal ALD processes typically result in a GPC of ~0.2-0.4 Å.[32,33] Although plasma-based processes have a higher GPC, ~0.7 Å/cycle,[34] surface damage due to high-energy ion/photon bombardment may be an issue.[18,35] To this end, as part of the work in this dissertation, we have developed a novel thermal ALD process to deposit TiO_2 films with a GPC comparable to the plasma-based processes. ALD processes of metal-oxides typically involve the use of a metal-precursor and an oxidizing agent like H_2O,[33] O_3[36] or O_2-plasma.[34] We use a unique metal-alkoxide metal-chloride precursor combination to deposit the TiO_2 thin films wherein the metal-alkoxide acts as the oxygen source. The use of metal-alkoxide as the oxygen source can potentially mitigate the formation of interfacial oxide observed in typical ALD processes.[37] Thus, this process can also be extended to deposit TiO_2 on oxygen sensitive substrates for other applications such as Ge-based semiconductor devices. We have studied the surface reaction mechanism for the ALD process using *in situ* ATR-FTIR spectroscopy and the quality of the films has been determined by various *ex situ* characterization techniques. The experimental techniques and results are described in detail in Chapter 3 of this dissertation.

1.2 Storage and Efficient use of Electrical Energy

The inherent intermittent nature of renewable energy sources like solar and wind makes it imperative to have an efficient storage system to ensure a stable and reliable supply of energy.[38–41] The function of the energy storage system would entail storage of energy from the grid during peak generation and supply of energy to the grid during fluctuations. A large portion of the harmful emissions is from burning of fossil fuels in transportation vehicles. Therefore, the use of electric vehicles can significantly help reduce emissions.[42–44] However, this requires batteries with enough capacity to power the vehicles over long distances.

1.2.1 Li-ion batteries

Amongst the various rechargeable battery technologies, Li-ion batteries (LIBs) are attractive candidates for energy storage. LIBs have a very high energy and power density, high operating voltage, and low self-discharge and maintenance.[40,41,45–47] As a result, LIBs are

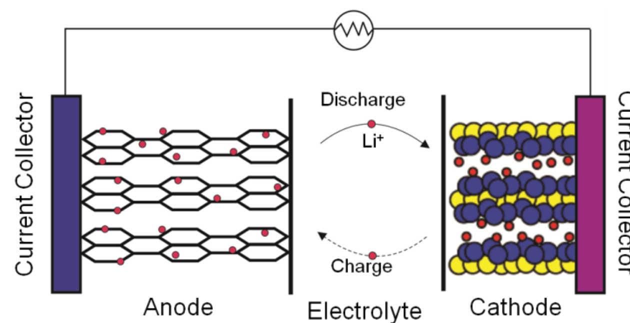

Figure 1.2. Schematic representation of Li-ion battery

extensively used in portable and handheld electronics. However, LIB technology needs significant improvements in areas like capacity, cost and durability before it can be used in energy intensive applications such as electric vehicles.[40] The answer to improving the LIB

technology lies in the materials used in the battery. Figure 1.2 shows a schematic representation of the LIB architecture. The charging and discharging of the battery involves shuttling of Li-ions across the two electrodes.

The total capacity of a LIB, expressed in mAh/g is given by,[48]

$$C_T = \frac{1}{\left(\frac{1}{C_A}\right)+\left(\frac{1}{C_C}\right)+\left(\frac{1}{Q_M}\right)} \qquad (1.1)$$

where, C_T is the total cell capacity, C_A and C_C are the theoretical specific capacities of the anode and cathode materials respectively, and Q_M is dependent on the electrolyte, separator, current collectors etc. [48] Thus, the total battery capacity is dependent on all the components, but the scope of this work is limited to the anode.

1.2.2 Group IV nanostructures in LIBs

Currently, graphite is used as the anode material in LIBs which has a theoretical specific capacity of ~372 mAh/g.[48–50] Other group IV elements like Si, Ge, and Sn, all have theoretical specific capacities significantly higher than graphite.[48–54] However, Si, Ge, and Sn undergo a ~300% volume expansion upon lithiation.[48–54] As a result, the electrode pulverizes due to the resulting mechanical stress leading to a loss in battery capacity in the first few cycles. The electrode pulverization can be avoided by the use of nanostructures. In nanoscale materials, the increase in surface energy due to the formation of new surfaces upon cracking is more than the energy released due to the relieving of mechanical stress. Thus, cracking becomes energetically unfavorable.[55–58] Additionally, it has been shown that to sustain battery capacity over large number of cycles, it is required to disperse these nanostructures in a conducting matrix, such as

graphite. Thus, carbon-coated Group IV nanostructures have been proposed as anode materials for high-capacity LIBs.[51,54,59,60] The synthesis of these nanostructures is often complex and involves multiple steps.[51,60,61] Therefore, a simple technique is required to synthesize carbon-coated Group IV nanostructures. This motivated us to develop a single-step technique based on non-thermal plasmas for the synthesis of carbon-coated Group IV nanoparticles (NPs). Non-thermal plasma synthesis has been shown to be a scalable technique that provides high yields of NPs with a narrow size distributions.[62–65] In this technique, we use two non-thermal plasmas in series to first synthesize the group IV NPs, and then coat them in-flight with carbon. We have used this technique to synthesize carbon-coated Si NPs. The Si NPs were synthesized using SiH_4 as the precursor gas and were coated with carbon using a C_2H_2 plasma. The setup is designed such that the two plasmas operate practically independent of each other and, thus enable us to independently control the core size and coating structure. The detailed results for synthesis of carbon-coated Si NPs using this technique are described in Chapter 4. We have extended this technique to synthesize carbon-coated Ge and Sn NPs. The Ge and Sn NPs were synthesized from chloride-based precursors, which emphasizes the versatility of this setup. The detailed results for the synthesis of carbon-coated Ge and Sn NPs using this setup are described in Chapter 5. To our knowledge, this is also the first report on the synthesis of Sn NPs using a non-thermal plasma setup.

1.2.3 Efficient use of electrical energy

In addition to generation of electricity via renewable sources, an additional aspect contributing to the reduction of fossil fuel emissions is the efficient use of electrical energy, specifically, for lighting. In the US, one-fifth of the electrical power is used for artificial

lighting.[66] Hence, improving the energy efficiency in artificial lighting would greatly impact fossil fuel emissions.[67] Historically, artificial lighting started with the invention of Edison's incandescent lamp. The efficiency of incandescent lamp is limited due to the upper limit of the filament temperature which results in emission dominated by the infrared.[68] The introduction of fluorescent lamps improved lighting efficiency, but the presence of Hg is undersirable. In addition, the efficiency of fluorescent lamps too is limited due to conversion of UV-photon to a photon in the visible range.[68] Light emitting diodes (LEDs) on the other hand, do not use toxic elements and have higher efficiencies compared to the incandescent and fluorescent lamps.[68,69] Silicon carbide (SiC), due to its high bandgap has been proposed as a potential material for blue LEDs.[70–72] Moreover, quantum confinement effects have been observed experimentally in SiC NPs.[73] Quantum confinement effects, observed when the dimensions of the NP become comparable to the Bohr exciton radius of the material, would enable tuning the bandgap of the NPs. In addition to LEDs, luminescent properties combined with the excellent chemical resistance of SiC make these NPs ideally suited for various biological labeling applications.[74,75]

Synthesis techniques for SiC NPs either use energy-intensive high-temperature processes, or complex, multi-step solution-based methods. Hence, we have developed a low-temperature synthesis technique based on non-thermal plasmas to synthesize crystalline 3C-SiC NPs. The synthesis setup is very similar to the one used to synthesize the carbon-coated Group IV NPs. The 3C-SiC NPs are synthesized via the complete carburization of Si NPs using a non-thermal C_2H_2 plasma. The synthesis technique is described in detail in Chapter 6 of this dissertation.

References

[1] M.S. Dresselhaus and I.L. Thomas, Nature **414**, 332 (2001).

[2] C. A. Wolden, J. Kurtin, J.B. Baxter, I. Repins, S.E. Shaheen, J.T. Torvik, A. a. Rockett, V.M. Fthenakis, and E.S. Aydil, J. Vac. Sci. Technol. A **29**, 030801 (2011).

[3] L.R. Kump, Nature **419**, 188 (2002).

[4] M. Hoffert, K. Caldeira, A. Jain, and E. Haites, Nature **395**, 881 (1998).

[5] J. Hansen, P. Kharecha, M. Sato, V. Masson-Delmotte, F. Ackerman, D.J. Beerling, P.J. Hearty, O. Hoegh-Guldberg, S.-L. Hsu, C. Parmesan, J. Rockstrom, E.J. Rohling, J. Sachs, P. Smith, K. Steffen, L. Van Susteren, K. von Schuckmann, and J.C. Zachos, PLoS One **8**, e81648 (2013).

[6] S. Bhattacharya and S. Kumar, Energy Syst. Direct Sol. Energy 333 (2004).

[7] F. Dinçer, Renew. Sustain. Energy Rev. **15**, 713 (2011).

[8] K.H. Solangi, M.R. Islam, R. Saidur, N. A. Rahim, and H. Fayaz, Renew. Sustain. Energy Rev. **15**, 2149 (2011).

[9] T.M. Razykov, C.S. Ferekides, D. Morel, E. Stefanakos, H.S. Ullal, and H.M. Upadhyaya, Sol. Energy **85**, 1580 (2011).

[10] G.R. Timilsina, L. Kurdgelashvili, and P. A. Narbel, Renew. Sustain. Energy Rev. **16**, 449 (2012).

[11] T. Saga, NPG Asia Mater. **2**, 96 (2010).

[12] W. Shockley and H.J. Queisser, J. Appl. Phys. **32**, 510 (1961).

[13] M.A. Green, Prog. PHOTOVOLTAICS **17**, 183 (2009).

[14] M.Z. Rahman and S.I. Khan, Mater. Renew. Sustain. Energy **1**, 1 (2012).

[15] J. Zhao, A. Wang, and M.A. Green, Sol. Energy Mater. Sol. Cells **66**, 27 (2001).

[16] A. Aberle, Prog. Photovoltaics Res. Appl. **8**, 362 (2000).

[17] G. Dingemans and W.M.M. Kessels, J. Vac. Sci. Technol. A **30**, 040802 (2012).

[18] B. Hoex, J.J.H. Gielis, M.C.M. van de Sanden, and W.M.M. Kessels, J. Appl. Phys. **104**, 113703 (2008).

[19] B. Hoex, S.B.S. Heil, E. Langereis, M.C.M. van de Sanden, and W.M.M. Kessels, Appl. Phys. Lett. **89**, 042112 (2006).

[20] F. Werner, B. Veith, D. Zielke, L. Kühnemund, C. Tegenkamp, M. Seibt, R. Brendel, and J. Schmidt, J. Appl. Phys. **109**, 113701 (2011).

[21] G. Dingemans, W. Beyer, M.C.M. van de Sanden, and W.M.M. Kessels, Appl. Phys. Lett. **97**, 152106 (2010).

[22] G. Dingemans, F. Einsele, W. Beyer, M.C.M. van de Sanden, and W.M.M. Kessels, J. Appl. Phys. **111**, 093713 (2012).

[23] F. Kersten, A. Schmid, S. Bordihn, J.W. Müller, and J. Heitmann, Energy Procedia **38**, 843 (2013).

[24] V. Naumann, M. Otto, R.B. Wehrspohn, M. Werner, and C. Hagendorf, Energy Procedia **27**, 312 (2012).

[25] A. Stesmans and V. V. Afanas'ev, J. Vac. Sci. Technol. B Microelectron. Nanom. Struct. **20**, 1720 (2002).

[26] D. Suh, D.-Y. Choi, and K.J. Weber, J. Appl. Phys. **114**, 154107 (2013).

[27] B.S. Richards, Prog. Photovoltaics Res. Appl. **12**, 253 (2004).

[28] B.S. Richards, J.E. Cotter, and C.B. Honsberg, Appl. Phys. Lett. **80**, 1123 (2002).

[29] A. Thomson and K. McIntosh, Prog. Photovoltaics Res. Appl. **20**, 343 (2012).

[30] S.M. George, Chem. Rev. **110**, 111 (2010).

[31] M. Leskelä and M. Ritala, Angew. Chem. Int. Ed. Engl. **42**, 5548 (2003).

[32] J. Aarik, A. Aidla, T. Uustare, K. Kukli, V. Sammelselg, M. Ritala, and M. Leskelä, Appl. Surf. Sci. **193**, 277 (2002).

[33] A. Rahtu and M. Ritala, Chem. Vap. Depos. **8**, 21 (2002).

[34] V.R. Rai and S. Agarwal, J. Phys. Chem. C **113**, 12962 (2009).

[35] G. Dingemans, N.M. Terlinden, D. Pierreux, H.B. Profijt, M.C.M. van de Sanden, and W.M.M. Kessels, Electrochem. SOLID STATE Lett. **14**, H1 (2011).

[36] V.R. Rai and S. Agarwal, J. Phys. Chem. C **112**, 9552 (2008).

[37] M. Ritala, K. Kukli, A. Rahtu, P. Raisanen, M. Leskelä, T. Sajavaara, and J. Keinonen, Science **288**, 319 (2000).

[38] A. Poullikkas, Renew. Sustain. Energy Rev. **27**, 778 (2013).

[39] H. Chen, T.N. Cong, W. Yang, C. Tan, Y. Li, and Y. Ding, Prog. Nat. Sci. **19**, 291 (2009).

[40] J. Chen, Materials (Basel). **6**, 156 (2013).

[41] J.B. Goodenough and Y. Kim, Chem. Mater. **22**, 587 (2010).

[42] M.M. Thackeray, C. Wolverton, and E.D. Isaacs, Energy Environ. Sci. **5**, 7854 (2012).

[43] V. Etacheri, R. Marom, R. Elazari, G. Salitra, and D. Aurbach, Energy Environ. Sci. **4**, 3243 (2011).

[44] X. Su, Q. Wu, J. Li, X. Xiao, A. Lott, W. Lu, B.W. Sheldon, and J. Wu, Adv. Energy Mater. **4**, 130082 (2014).

[45] M. Armand and J.-M. Tarascon, Nature **451**, 652 (2008).

[46] J.-M. Tarascon and M. Armand, Nature **414**, 359 (2001).

[47] J.B. Goodenough and K.-S. Park, J. Am. Chem. Soc. **135**, 1167 (2013).

[48] U. Kasavajjula, C. Wang, and A.J. Appleby, J. Power Sources **163**, 1003 (2007).

[49] H. Wu and Y. Cui, Nano Today **7**, 414 (2012).

[50] J. Graetz, C.C. Ahn, R. Yazami, and B. Fultz, J. Electrochem. Soc. **151**, A698 (2004).

[51] G. Cui, L. Gu, L. Zhi, N. Kaskhedikar, P. a. van Aken, K. Müllen, and J. Maier, Adv. Mater. **20**, 3079 (2008).

[52] J. Graetz, C.C. Ahn, R. Yazami, and B. Fultz, Electrochem. Solid-State Lett. **6**, A194 (2003).

[53] M. Noh, Y. Kwon, H. Lee, and J. Cho, Chem. Mater. **796**, 1926 (2005).

[54] W.-M. Zhang, J.-S. Hu, Y.-G. Guo, S.-F. Zheng, L.-S. Zhong, W.-G. Song, and L.-J. Wan, Adv. Mater. **20**, 1160 (2008).

[55] A. Griffith, Philos. Trans. R. Soc. London **221**, 163 (1921).

[56] K.E. Aifantis, S.A. Hackney, and J.P. Dempsey, J. Power Sources **165**, 874 (2007).

[57] K.E. Aifantis and J.P. Dempsey, J. Power Sources **143**, 203 (2005).

[58] Z. Ma, T. Li, Y. Huang, J. Liu, Y. Zhou, and D. Xue, RSC Adv. **3**, 7398 (2013).

[59] S.-H. Ng, J. Wang, D. Wexler, K. Konstantinov, Z.-P. Guo, and H.-K. Liu, Angew. Chem. Int. Ed. Engl. **45**, 6896 (2006).

[60] L. Cui, Y. Yang, C. Hsu, and Y. Cui, 1 (2009).

[61] N. Liu, H. Wu, M.T. McDowell, Y. Yao, C. Wang, and Y. Cui, Nano Lett. **12**, 3315 (2012).

[62] U. Kortshagen, J. Phys. D. Appl. Phys. **42**, 113001 (22 pp) (2009).

[63] R. Gresback, Z. Holman, and U. Kortshagen, Appl. Phys. Lett. **91**, 093119 (2007).

[64] O. Yasar-Inceoglu and L. Mangolini, Mater. Lett. **101**, 76 (2013).

[65] L. Mangolini, E. Thimsen, and U. Kortshagen, Nano Lett. **5**, 655 (2005).

[66] S. Pimputkar, J.S. Speck, S.P. DenBaars, and S. Nakamura, Nat. Photonics **3**, 180 (2009).

[67] A. Bergh, G. Craford, A. Duggal, and R. Haitz, Phys. Today 42 (2001).

[68] E.F. Schubert and J.K. Kim, Science **308**, 1274 (2005).

[69] M.-H. Chang, D. Das, P.V. Varde, and M. Pecht, Microelectron. Reliab. **52**, 762 (2012).

[70] H. Mimura, T. Matsumoto, and Y. Kanemitsu, Appl. Phys. Lett. **65**, 3350 (1994).

[71] T. Matsumoto, J. Takahashi, T. Tamaki, T. Futagi, H. Mimura, and Y. Kanemitsu, Appl. Phys. Lett. **64**, 226 (1994).

[72] F. Fuchs, V. A. Soltamov, S. Väth, P.G. Baranov, E.N. Mokhov, G. V Astakhov, and V. Dyakonov, Sci. Rep. **3**, 1637 (2013).

[73] X. Wu, J. Fan, T. Qiu, X. Yang, G. Siu, and P. Chu, Phys. Rev. Lett. **94**, 026102 (2005).

[74] J. Fan, H. Li, J. Jiang, L.K.Y. So, Y.W. Lam, and P.K. Chu, Small **4**, 1058 (2008).

[75] J. Botsoa, V. Lysenko, A. Géloën, O. Marty, J.M. Bluet, and G. Guillot, Appl. Phys. Lett. **92**, 173902 (2008).

CHAPTER 2

MECHANISM OF CHEMICAL PASSIVATION OF *c*-SI BY AL_2O_3 STUDIED USING *IN SITU* INFRARED SPECTROSCOPY

Rohan Chaukulkar[1], William Nemeth,[2] Arrelaine Dameron,[2] Paul Stradins,[2] and Sumit Agarwal[1]

[1]Colorado School of Mines, Golden, CO, 80401, USA

[2]National Renewable Energy Laboratory, Golden, CO, 80401, USA

Abstract

Al_2O_3 has been shown to provide excellent surface passivation for *c*-Si. Here, we have studied the mechanism of chemical passivation of *c*-Si by Al_2O_3 using attenuated total reflection Fourier transform infrared (ATR-FTIR) spectroscopy. Al_2O_3 was deposited on high lifetime *c*-Si substrates via atomic layer deposition, using a precursor combination of trimethyl aluminum (TMA) and H_2O. This was followed by the annealing step which activates the passivation. ATR-FTIR spectroscopy allows us to monitor the *c*-Si/Al_2O_3 interface, as well as the bulk of the Al_2O_3 thin films during the entire process. Our results indicate that surface Si-H bonds are not completely consumed during the deposition of Al_2O_3 on H-terminated Si. Additionally, during the annealing step, it is the restructuring at the interface, to form the interfacial SiO_x that contributes to the decrease in interface defect density. We have used deuterated precursors to differentiate between the various sources of atomic H present in the process. Within the sensitivity of our IR setup, we do not observe any migration of atomic H from Al_2O_3 to the *c*-Si/Al_2O_3 interface. We have used Al_2O_3/SiO_2/Si stacks to isolate the effects of chemical and

field-effect passivation of Al_2O_3 thin films. We anneal these stacks in different atmospheres to test the influence of annealing atmospheres on the chemical passivation of *c*-Si by Al_2O_3.

2.1 Introduction

Si-based single-junction solar cells, under 1 Sun illumination, have a maximum theoretical efficiency of ~29%.[1] While laboratory-based solar cells have demonstrated efficiencies ~25%, industrial solar cells lag considerably behind.[2] Inefficient surface passivation leading to recombination losses, is one of the main reasons attributed for this difference in efficiencies.[3] Al_2O_3 has been shown to be an excellent surface passivant for *c*-Si with surface recombination velocities (S_{eff}) <5 cm/s reported.[4,5] This reduction in recombination losses, activated after a post-deposition annealing step, is achieved by a combination of chemical and field effect passivation.[6] The recombination losses at the semiconductor interface are proportional to the interface defect density (D_{it}). Thus a reduction in D_{it}, known as chemical passivation, leads to a reduction in the recombination losses. D_{it} values as low as $\sim 3\times10^{10}$ have been reported for *c*-Si surfaces passivated by Al_2O_3.[4,7] Additionally, Al_2O_3 thin films form a fixed negative charge with density $\sim 10^{12}$-10^{13} cm^{-2}, which reduces the negative carrier concentration at the interface leading to a further reduction in recombination losses. Although the exact origin of the fixed negative charge in Al_2O_3 thin films has not been accurately determined,[4,8] there have been numerous studies which propose a mechanism for the chemical passivation.[5,6,9–11] It has been shown via transmission electron microscopy (TEM) studies[8,9] that the annealing step leads to the formation of an interfacial SiO_x layer through restructuring at the *c*-Si/Al_2O_3 interface. To explain the chemical passivation some reports suggest that, in addition to restructuring at the interface, H from Al_2O_3 migrates to the *c*-Si interface during the annealing

step, which passivates the Si dangling bonds leading to a reduction in D_{it}.[6,10] Since Al_2O_3 acts as the reservoir of H, annealing in N_2 or H_2 atmospheres leads to a similar level of passivation. On the other hand, Stesmans and coworkers studied the *c*-Si/Al_2O_3 interface and concluded that the as-deposited *c*-Si/Al_2O_3 interface resembles a low-temperature *c*-Si/SiO_2 interface in an enhanced stress state and needs a O_2 atmosphere anneal to attain a relaxed state.[12,13] Kersten and coworkers studied the role of annealing conditions of the passivation of *c*-Si by Al_2O_3 and reported that annealing in an O_2 atmosphere leads to a lower D_{it}.[5] This suggests that the exact mechanism of chemical passivation of *c*-Si by Al_2O_3 may not be fully understood.

Here, we have studied the chemical passivation of *c*-Si by Al_2O_3 using attenuated total reflection Fourier transform infrared (ATR-FTIR) spectroscopy. Al_2O_3 is deposited on high-lifetime Si internal reflection crystals (IRCs) using precursor combinations of trimethylaluminum (TMA) and H_2O. Then the substrates are annealed in various atmospheres at 400 °C for 15 minutes. The IR measurements are complemented by minority carrier lifetime measurements which enable us to determine the quality of passivation. We have carried out the IR studies on H- as well as D-terminated Si surfaces. The use of D-terminated Si surfaces allow us to differentiate between the various sources of H in the process thus enabling us to track the migration of H during the annealing step. Within the sensitivity of our IR setup of $\sim 10^{12}$ cm^{-2} we do not observe any migration of H from Al_2O_3 to the *c*-Si/Al_2O_3 interface during the annealing step. Our IR data also indicates that H is preserved at the interface upon deposition of Al_2O_3 on H-terminated Si surface. Upon annealing restructuring to form interfacial SiO_x was observed. Annealing *c*-Si/SiO_2/Al_2O_3 stacks in different atmospheres indicated that annealing in an oxidizing environment leads to a better passivation quality.

2.2 Experimental Setup

The ATR-FTIR setup used in this study is explained in detailed elsewhere.[14] The studies are carried out on trapezoidal Si IRCs (50 × 10 × 1 mm) machined out of 1 mm thick

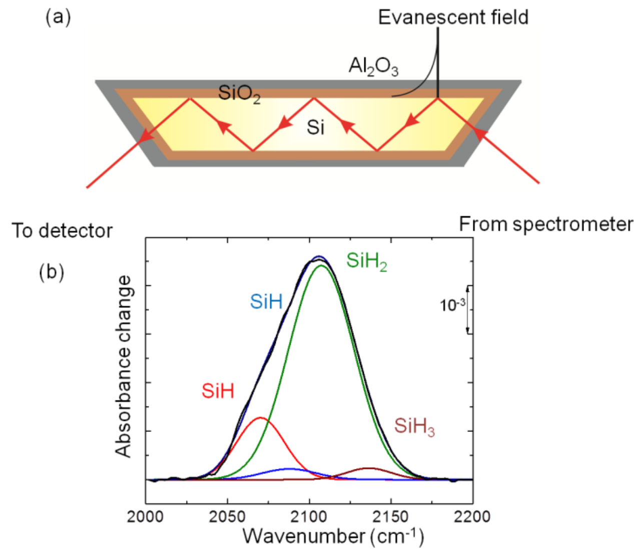

Figure 2.1. (a) Cross section schematic representation of the multiple internal reflections of the IR beam in the IRC and the decay of the electric field associated with IR beam. **(b)** IR difference spectrum of the SiH_x region for a H-terminated Si IRC. The spectrum is deconvoluted to show the various silicon hydrides present on the surface. The deconvolution was performed using Gaussian line shapes.

high-lifetime Si wafers (bulk lifetime > 2 ms). These substrates allow us to correlate the changes in chemical composition, studied using IR spectroscopy, with the passivation quality determined using minority carrier lifetime measurements. Figure 2.1(a) is a schematic representation of the cross section of the IRC showing the multiple internal reflections. Due to the difference in refractive indices of Si and Al_2O_3, the total internal reflection occurs at the Si/Al_2O_3 interface.

However, the evanescent electric field, which decays exponentially, extends into the bulk of the Al_2O_3 film. The penetration depth of the evanescent field is related to the refractive indices of Si and Al_2O_3, and can be calculated from the expression,[15]

$$d_p = \frac{\lambda}{2\pi n_{Si}\sqrt{\sin^2\theta - (n_{Al2O3}/n_{Si})^2}} \tag{2.1}$$

where, d_p is the penetration depth, n_{Si} and n_{Al2O3} are the refractive indices of Si and Al_2O_3 respectively, θ is the angle of incidence and λ is the wavelength. The penetration depth calculated at a wavelength of 2000 cm^{-1} and an angle of incidence of 45 ° for the Si/Al_2O_3 system using the above expression is ~450 nm. Therefore, the setup allows us to probe not only the Si/Al_2O_3 interface but also the bulk of the Al_2O_3 films. In addition, the multiple internal reflections (50 in total), provide us with sub-monolayer sensitivity.[14,15] Figure 2.1(b) shows the IR spectrum for a H-terminated Si IRC. The surface is predominantly terminated with SiH_2 as expected for a Si (100) substrate.[16,17] Based on the signal-to-noise ratio calculated using this spectrum the sensitivity of the ATR-FTIR setup was determined to be ~10^{12} cm^{-2} for Si-H bonds.

H-terminated Si surface was obtained by etching the native oxide covered IRC in a 2% HF solution. Al_2O_3 was then deposited on the H-terminated IRC at a temperature of 200 °C, using a precursor combination of trimethyl aluminum (TMA) and H_2O in a commercial Beneq reactor. The IRC was annealed at 400 °C for 15 minutes in a N_2 atmosphere. An IR reference spectrum was collected before and after each of the processing steps. This allowed us to monitor the effect of the processing step on the chemical composition of the interface. The IR data was collected over the range of 1700-4000 cm^{-1} with a resolution of 4 cm^{-1} using 1000 averages. Si/SiO_2/Al_2O_3 test structures were used to study the role of H in the chemical passivation of *c*-Si

by Al_2O_3. To differentiate between the various sources of H present in the system, the studies were carried out on a D-terminated Si IRC. The D-termination was achieved by etching the

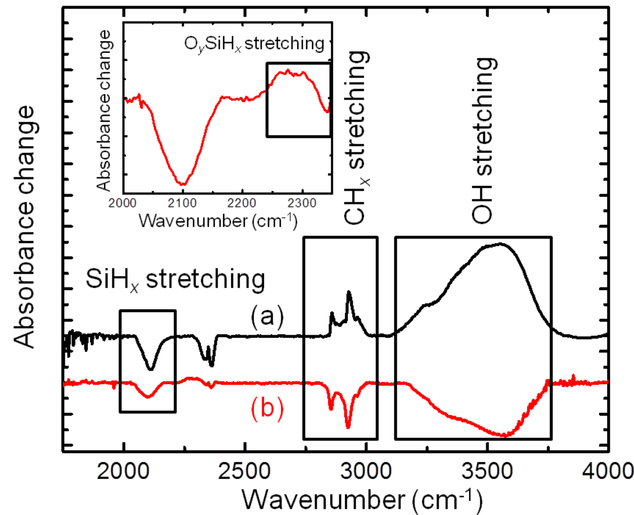

Figure 2.2. (a) IR difference spectrum collected after the deposition of Al_2O_3 on H-terminated Si IRC **(b)** IR difference spectrum collected after annealing the Al_2O_3 covered IRC at 400 °C in a N2 atmosphere for 15 minutes. Inset is the zoomed in view of the SiH_x region which shows the increase in absorbance in the region assigned to the $OSiH_x$ species

native oxide covered substrate in a solution of ~5g KF (Sigma Aldrich, >99%) in ~30 mL D_2O (Sigma Aldrich, 99.9 atom% D).[18,19] 0.5 mL of 35 wt% DCl in D_2O was added to manipulate the D-concentration of the etching solution.[18,19] ~50 nm of SiO_2 was then grown on the D-terminated substrate via dry thermal oxidation at ~850 °C. This was followed by the deposition of ~30 nm of Al_2O_3 using the TMA-H_2O process. The sample was then annealed at 400 °C in a N_2 atmosphere for 15 minutes. IR reference spectra were collected before and after each processing step to track the H content at the interface. The test structures were also used to study the effect

of the annealing atmosphere on the chemical passivation of *c*-Si by Al_2O_3. The structures were annealed in N_2, ambient and O_2 atmospheres and the passivation quality was evaluated using WCT-120 Sinton lifetime tester.

2.3 Results and Discussion

Figure 2.2(a) shows the IR difference spectrum collected after the deposition of Al_2O_3 on H-terminated Si IRC. We observe changes in absorbance in the 2000-2200, 2700-3000 and 3200-3700 cm^{-1} regions which have been assigned to the SiH_x, CH_x and OH stretching modes respectively.[16,20] The decrease in absorbance in the SiH_x stretching region indicates consumption of the surface hydrides during Al_2O_3 deposition. The increase in absorbance in the CH_x and OH stretching regions indicate the present of impurities in the Al_2O_3 film in the form of hydrocarbons and hydroxyls. The spectrum in Fig. 2.2 (b) is collected after annealing the Al_2O_3-coated-Si IRC at 400 °C, in an N_2 atmosphere for 15 minutes. Upon annealing, a decrease in absorbance in the region assigned to the SiH_x stretching mode is observed. This suggests that the initial surface hydrides are not completely consumed during Al_2O_3 deposition. This observation is similar to the one reported previously in literature,[21] where Si-H bonds were found to be preserved at the interface upon deposition of Al_2O_3 on H-terminated Si substrates. We also observe a decrease in absorbance in the CH_x and OH stretching regions which indicates that some of the impurities in the Al_2O_3 film are lost during thermal annealing. Previously, CO_2, H_2O, CO and H_2 have been reported as effusion products during thermal annealing of Al_2O_3 films.[6,22] The inset in Figure 2.2 shows the zoomed in view of the 2000-2400 cm^{-1} region. In addition to the decrease in absorbance in the SiH_x stretching region, we also observe an increase in the 2250-2350 cm^{-1} region which has been assigned to the O_ySiH_x stretching modes.[23] This

indicates restructuring at the interface leading to the formation of interfacial SiO_x, which has been previously observed during the thermal annealing of Al_2O_3 films on *c*-Si.[8,9] Although these results conclusively prove restructuring at the interface during the annealing step, they do not

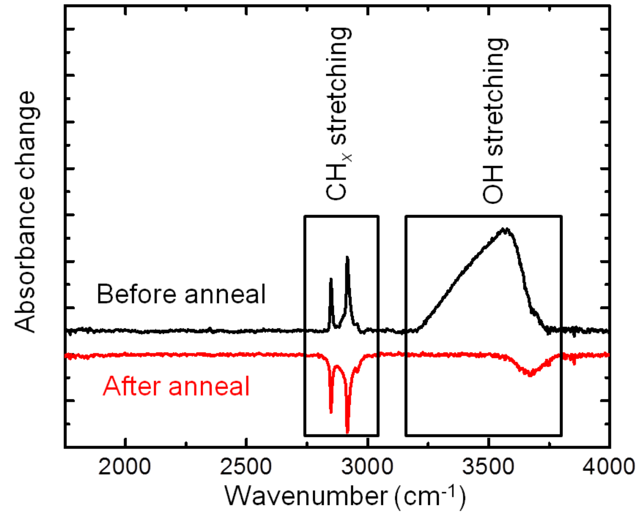

Figure 2.3. IR difference spectra collected before and after anneal for $Si/SiO_2/Al_2O_3$ test structures.

elucidate the role of H from Al_2O_3, in the chemical passivation. For example, the thermal desorption of interfacial H and restructuring could be accompanied by the migration of H from Al_2O_3 resulting in a net decrease in the interfacial H content. Therefore, to differentiate between the various sources of H present in the system, we use D-terminated Si substrates which allow us to differentiate between interfacial H and the H originating from Al_2O_3. The migration of H from Al_2O_3 to the *c*-Si interface would also lead to an increase in the H content of the interfacial SiO_x layer,[10] which would lead to the formation of O_ySiH_x species. Therefore, we grow ~50 nm of SiO_2 on D-terminated Si IRC. The thicker SiO_2 gives us increased sensitivity in detecting the migration of H from Al_2O_3 to the *c*-Si interface via the detection of O_ySiH_x species.[15]

Figure 2.3 shows the IR difference spectra collected for the $Si/SiO_2/Al_2O_3$ test structures before and after annealing. The annealing was carried out at 400 °C in a N_2 atmosphere for 15 minutes. As observed in the previous experiment, impurities in the form of hydrocarbons and hydroxyls are present in the Al_2O_3 film, and after annealing we see a decrease in the impurity content of the film. But more importantly, we do not observe any increase in absorbance in the SiH_x or O_ySiH_x stretching region. Thus, we do not observe any migration of H from Al_2O_3 to the *c*-Si interface during the thermal annealing step. We can therefore conclude that the restructuring at the interface to form the interfacial SiO_x layer is the dominant factor which contributes to the chemical passivation of *c*-Si by Al_2O_3.

Our conclusion was further supported by additional annealing studies carried out on the $Si/SiO_2/Al_2O_3$ test structures. The structures were annealed in different atmospheres and minority carrier lifetime measurements were used to determine the passivation quality. We found that annealing in ambient/O_2 atmospheres leads to a better level of passivation as compared to annealing in a N_2 atmosphere. We obtained implied open circuit voltage (iV_{oc}) values of ~635-650 mV for ambient and O_2 atmospheres while the annealing in a N_2 atmosphere lead to iV_{oc} values of ~615 mV. Our previous studies on Al_2O_3 coated Si, as well as various reports in literature[4,6] have indicated a similar level of passivation for annealing performed in a N_2 or a forming gas environment. Therefore, the $Si/SiO_2/Al_2O_3$ test structures were annealed only in a N_2 atmosphere. These annealing studies thus indicate that an oxidizing environment leads to a better passivation level as compared to a N_2 environment further emphasizing the importance of the interfacial SiO_x layer.

2.4 Conclusions

We have studied the mechanism of chemical passivation of *c*-Si by Al_2O_3 using ATR-FTIR spectroscopy and minority carrier lifetime studies. Our IR data indicates that H is preserved at the interface after deposition of Al_2O_3 on H-terminated Si. The H is then lost during the thermal annealing via thermal desorption and restructuring. Thermal annealing also leads to the formation of an interfacial SiO_x layer through restructuring. We have used deuterated precursors to study the role of H in the chemical passivation. The IR studies indicate we do not observe migration of H from Al_2O_3 to the *c*-Si interface during the annealing step. We have used $Si/SiO_2/Al_2O_3$ test structures to study the effect of the annealing atmosphere on the passivation quality and our studies suggest a better passivation quality is observed under oxidizing environments further emphasizing the importance of the interfacial SiO_x layer.

Acknowledgements

We gratefully acknowledge the support from the NCPV Fellowship Program and U.S. Department of Energy, Office of Energy Efficiency and Renewable Energy, under Contract No. DE-AC36-08GO28308 with the National Renewable Energy Laboratory.

References

[1] W. Shockley and H.J. Queisser, J. Appl. Phys. **32**, 510 (1961).

[2] M.A. Green, Prog. PHOTOVOLTAICS **17**, 183 (2009).

[3] M.Z. Rahman and S.I. Khan, Mater. Renew. Sustain. Energy **1**, 1 (2012).

[4] G. Dingemans and W.M.M. Kessels, J. Vac. Sci. Technol. A Vacuum, Surfaces, Film. **30**, 040802 (2012).

[5] F. Kersten, A. Schmid, S. Bordihn, J.W. Müller, and J. Heitmann, Energy Procedia **38**, 843 (2013).

[6] G. Dingemans, F. Einsele, W. Beyer, M.C.M. van de Sanden, and W.M.M. Kessels, J. Appl. Phys. **111**, 093713 (2012).

[7] R. Hezel and K. Jaeger, J. Electrochem. Soc. **136**, 518 (1989).

[8] V. Naumann, M. Otto, R.B. Wehrspohn, M. Werner, and C. Hagendorf, Energy Procedia **27**, 312 (2012).

[9] B. Hoex, J.J.H. Gielis, M.C.M. van de Sanden, and W.M.M. Kessels, J. Appl. Phys. **104**, 113703 (2008).

[10] G. Dingemans, W. Beyer, M.C.M. van de Sanden, and W.M.M. Kessels, Appl. Phys. Lett. **97**, 152106 (2010).

[11] Y. Zhao, C. Zhou, X. Zhang, P. Zhang, Y. Dou, W. Wang, X. Cao, B. Wang, Y. Tang, and S. Zhou, Nanoscale Res. Lett. **8**, 114 (2013).

[12] A. Stesmans and V. V. Afanas’ev, J. Vac. Sci. Technol. B **20**, 1720 (2002).

[13] A. Stesmans and V. V. Afanas’ev, Appl. Phys. Lett. **80**, 1957 (2002).

[14] V.R. Rai and S. Agarwal, J. Vac. Sci. Technol. A **30**, 01A158 (2012).

[15] D.C. Marra, Plasma Deposition of Hydrogenated Amorphous Silicon Studied Using In Situ Multiple Total Internal Reflection Infrared Spectroscopy, University of California, Santa Barbara, 2000.

[16] Y. Chabal, J. Mol. Struct. **292**, 65 (1993).

[17] P. Dumas, Y.J. Chabal, and P. Jakob, Surf. Sci. **269/270**, 867 (1992).

[18] H. Luo and C.E.D. Chidsey, Appl. Phys. Lett. **72**, 477 (1998).

[19] G. Ferguson, K. Raghavachari, D.J. Michalak, and Y. Chabal, J. Phys. Chem. C **112**, 1034 (2008).

[20] V. Rai, V. Vandalon, and S. Agarwal, Langmuir **26**, 13732 (2010).

[21] K.Y. Gao, F. Speck, K. Emtsev, T. Seyller, and L. Ley, J. Appl. Phys. **102**, 094503 (2007).

[22] G. Dingemans, P. Engelhart, R. Seguin, F. Einsele, B. Hoex, M.C.M. van de Sanden, and W.M.M. Kessels, J. Appl. Phys. **106**, 114907 (2009).

[23] B.N. Jariwala, O.S. Dewey, P. Stradins, C. V Ciobanu, and S. Agarwal, ACS Appl. Mater. Interfaces **3**, 3033 (2011).

CHAPTER 3

ATOMIC LAYER DEPOSITION OF TITANIUM DIOXIDE USING TITANIUM TETRACHLORIDE AND TITANIUM TETRAISOPROPOXIDE AS PRECURSORS

Based on a paper published in The Journal of Vacuum Science & Technology A

Rohan P Chaukulkar[1] and Sumit Agarwal[1]

[1]Department of Chemical and Biological Engineering, Colorado School of Mines, Golden, Colorado 80401

Abstract

Most atomic layer deposition (ALD) processes for metal oxides involve the use of a metal precursor and an oxygen source, such as H_2O, O_3, or an O_2 plasma. These ALD processes lead to the formation of an undesirable interfacial oxide during deposition on semiconductor surfaces. As an alternative, some metal oxides other than TiO_2 have been deposited using metal alkoxides as the oxygen source. In this article, we report on the ALD of TiO_2 using $TiCl_4$ and titanium tetraisopropoxide (TTIP) as precursors. Our surface infrared spectroscopy data shows that over the temperature range of 150-250 °C and the duration of a typical ALD cycle (~1-10 s), in both half-reaction cycles, the surface reaction mechanism is dominated by alkyl-transfer from the TTIP ligands to Ti-Cl species. At 250 °C, which is the onset for TTIP thermal decomposition, the contribution of the direct decomposition reaction to film growth is negligible. The growth per cycle, ~0.7 Å at 200 °C, is higher than H_2O-based ALD of TiO_2 from either $TiCl_4$ or TTIP, but similar to O_2-plasma-based processes. X-ray photoelectron spectroscopy data show TiO_2 films

with only the +4 oxidation state of Ti, and the Cl content is estimated to be 2.5-3.5%. UV-Vis spectroscopy shows a band gap of ~3.0 eV, which is comparable to the values reported in the literature for amorphous TiO_2 thin films.

3.1 Introduction

The continued scaling of microelectronic devices has led to an increased interest in high-κ dielectric materials, and the development of techniques to deposit thin layers of these materials onto semiconductor substrates.[1,2] In particular, TiO_2, due to its high dielectric constant (~80), has been proposed as the gate dielectric material for Ge-based electronic devices.[3,4] Amongst the various thin-film deposition methods, atomic layer deposition (ALD) has been widely used to deposit ultra-thin, highly-conformal films of metal oxides on high-aspect-ratio structures with digital control over the film thickness.[5-8] The ALD of metal oxides typically involves two self-saturating half-reaction cycles, one consisting of a metal precursor such as a halide, metal-organic, or an organometallic, which is followed by exposure of the surface to an oxygen source, such as H_2O, O_3, H_2O_2, or an O_2-plasma.[9–13] The growth per cycle in most ALD processes is typically a fraction of a monolayer, which causes the underlying substrate to be exposed to the oxygen source for several half-reaction cycles: in the case of semiconductor substrates, this can lead to the formation on an undesirable interfacial oxide. Specifically, during deposition of TiO_2 on Ge, an interfacial GeO_2 layer can form, which is known to lead to a high-defect-density interface with Ge. Due to the small conduction band offset between Ge and TiO_2, a ~1 nm-thick interlayer of another dielectric material is desired.[3,14] However, this thin interlayer would still not be sufficient to prevent the diffusion of oxygen precursors such as H_2O or atomic O to the Ge surface in the ALD process, and would lead to the formation of a poorly controlled GeO_2 interfacial layer. Ritala and coworkers proposed a method for ALD of metal oxides, which

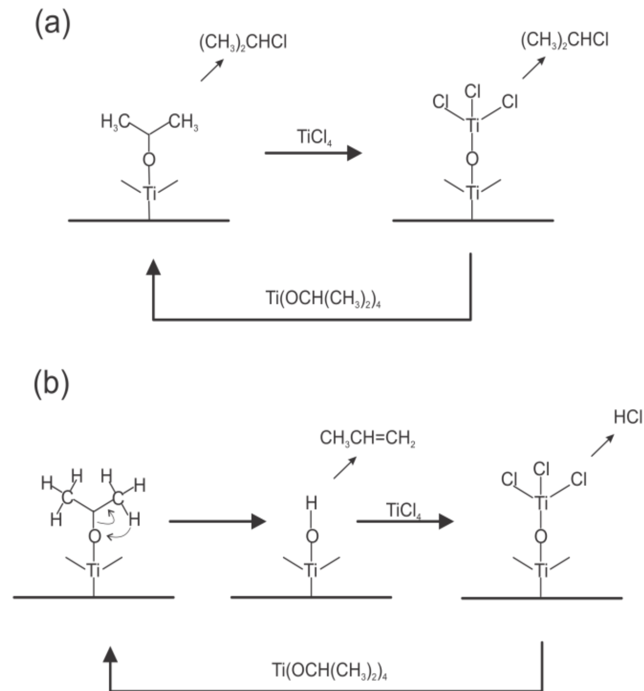

Figure 3.1. Schematic representation of the reactions during TiO_2 ALD using TTIP and $TiCl_4$. (a) The alkyl-transfer process, which involves a simple ligand-exchange reaction of the surface isopropoxy ligands with $TiCl_4$ to produce isopropyl chloride as the reaction product. (b) The β-hydride elimination process, which proceeds via decomposition of the surface isopropoxy ligands to create a hydroxyl-terminated surface followed by reaction of $TiCl_4$ to produce HCl as the reaction product. In both cases, the Cl-terminated surface obtained after the $TiCl_4$ cycle reacts with TTIP to produce isopropyl chloride, thus restoring the initial isopropoxy-ligand-terminated surface. Reaction (b) is more likely to occur at ≥ 250 °C, which is reported to be the temperature for the onset of TTIP thermal decomposition.

involves a metal halide and a metal alkoxide as the oxygen source.[15] In fact, the authors reported a native oxide-free interface between Si and Al_2O_3 during ALD using aluminum isopropoxide

and aluminum chloride.[15] Surface reaction mechanisms during the ALD with metal alkoxides as the oxygen source has been previously studied experimentally and computationally by Ritala,[16] and Musgrave[17] respectively. The ALD process has been reported to proceed through two possible surface reaction pathways – the alkyl-transfer and the β-hydride elimination mechanism, shown schematically in Fig. 3.1. Several metal oxides including Ta_2O_5, and other mixed-metal oxides have been deposited by this technique; however, deposition of TiO_2 using this method has not been reported in the literature.[15,18–21] Herein, we have used *in situ* attenuated total reflection Fourier transform infrared (ATR-FTIR) spectroscopy to study the surface reaction mechanism during the ALD of TiO_2 using $TiCl_4$ and titanium tetraisopropoxide [$Ti(OCH(CH_3)_2)_4$, TTIP] as the precursors. Further, *ex situ* analysis using X-ray photoelectron spectroscopy (XPS), UV-Vis spectroscopy, and spectroscopic ellipsometry (SE) shows that film deposition occurs over a temperature range of 150-250 °C with a growth per cycle of ~0.7 Å at 200 °C.

3.2 Experimental Details

The surface reactions were studied in an in-house-built, cold-wall reactor maintained at a base pressure of ~5 mTorr and equipped with an *in situ* ATR-FTIR spectroscopy setup, described previously.[22] TTIP (Sigma Aldrich, ≥97%) was delivered using N_2 as the carrier gas via a bubbler maintained at 70-75 °C, while $TiCl_4$ (Sigma Aldrich, 99.95%) was delivered without a carrier gas through a bubbler maintained at ~30 °C. The vapor delivery lines were heated to ~40-50 °C to avoid precursor condensation. The precursors were pulsed into the reactor through solenoid valves. Ar was used as the purge gas: a constant flow of 80 standard cm^3/min (sccm) was maintained throughout the ALD process, which provided a background pressure of ~35 mTorr. TTIP and $TiCl_4$ were pulsed for 5 and 10 s, respectively, to ensure complete surface

reactions. The chamber pressure during the TTIP and $TiCl_4$ cycles was ~360 and ~100 mTorr, respectively. The precursor delivery cycles were separated by a 30-s Ar purge step.

The IR studies were performed on 50 × 10 × 1 mm ZnSe trapezoidal internal reflection crystals (IRCs) with the short faces beveled at 45°. To ensure that we were studying surface reactions directly relevant to TiO_2 ALD from TTIP and $TiCl_4$ on a TiO_2 surface, and not the initial nucleation phase on a foreign substrate, the surface of the IRC was carefully coated with a thin layer of TiO_2 using a two-step procedure. First, a ~15-nm-thick layer of TiO_2 was deposited onto the ZnSe IRC using O_2-plasma-assisted ALD of TiO_2 from TTIP at a substrate temperature of 150 °C.[23] Second, to obtain an initial starting surface that was representative of the TTIP/$TiCl_4$ ALD process, for 10-15 ALD cycles, prior to collection of the IR data, we switched to TTIP and $TiCl_4$ as precursors while the IRC was maintained at the temperature of the experiment. The IR spectra were recorded as difference spectra, where a fresh reference spectrum was collected before each half-cycle. Thus, an IR spectrum collected with respect to this reference, enabled us to directly probe the changes in the surface composition in a given half-reaction cycle. The IR spectra were recorded with a 4 cm^{-1} resolution and averaged over 1000 scans.

The surface analysis chamber described above was not suitable for conducting ALD experiments over several 100s of cycles. Therefore, to deposit ~20-30-nm-thick films for *ex situ* characterization, we also deposited TiO_2 films in a small tubular, hot-wall (75 °C), ALD reactor, also described previously.[22] These set of experiments were also carried out with a constant 120 sccm Ar purge. TTIP and $TiCl_4$ were pulsed for 1 s, with the cycles separated by a 20-s Ar purge. The TiO_2 film growth was studied for these ALD conditions on three different surfaces: (a) Native-oxide-free, HF-treated Si wafers with an H-terminated surface; (b) Si wafers coated with

~20-30 nm of TiO_2 grown using TTIP-O_2 plasma ALD,[23] followed by UV exposure at 253.7 nm for ~5 min under ambient conditions to provide an –OH-terminated TiO_2 surface;[24] and (c) glass slides (VWR soda-lime glass) treated with a Piranha solution (3:1 mixture by volume of 98% H_2SO_4 and 30% H_2O_2), which provided an –OH-terminated surface.[25] We were not able to characterize the films grown on HF-treated Si wafers, due to the poor nucleation of TiO_2 on H-

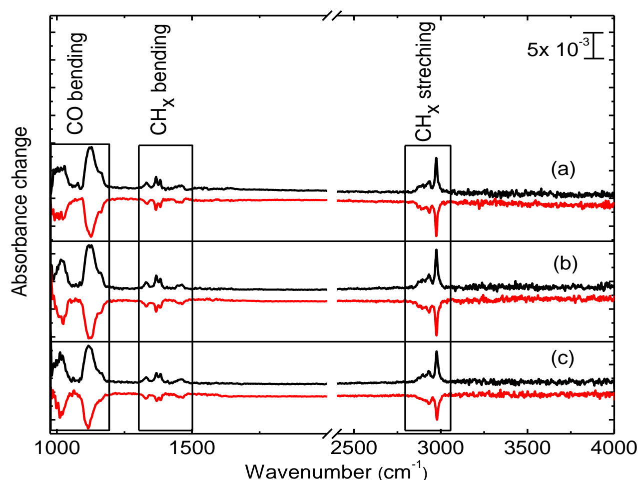

Figure 3.2. IR difference spectra showing the absorbance due to the various surface species involved in the ligand exchange reactions during TTIP (black) and $TiCl_4$ (red) half-reaction cycles at a substrate temperature of (a) 150, (b) 175 and (c) 200 °C. The almost identical change in absorbance during the two half-reaction cycles suggests a one-to-one ligand-exchange characteristic of an ALD process.

terminated Si, which led to films that were <5 nm thick. TiO_2 films deposited on TiO_2-pre-coated Si wafers were characterized using spectroscopic ellipsometry (SE, Woollam M-44). We modeled the dielectric function of TiO_2 using a Cauchy model over the range of 450-1300 nm, where TiO_2 has negligible absorption.[26] To separate the contribution of the TiO_2 film deposited by TTIP-O_2 plasma ALD from the TTIP-$TiCl_4$ ALD films, first, we recorded SE data for the

TiO_2-pre-coated Si substrates. Second, we fixed the optical constants and thickness for this underlayer and fit the TiO_2 overlayer with the Cauchy model to obtain the film thickness and refractive index. The band gap of the TiO_2 films was determined by UV-Vis spectroscopy (Cary 5G) using films deposited on the piranha-treated glass slides. The absorbance for the films, A, was then calculated using the relation, $A = 2 - \log(\% T)$, where $\% T$ is the measured percent transmittance referenced to the substrate. The elemental composition of the films grown on TiO_2-pre-coated Si and piranha-treated glass slides was determined using XPS (Kratos Analytical, Al $K\alpha$ X-ray source). Specifically, we conducted high-resolution scans (0.1 eV) for the C 1s, O 1s, Cl 2p, and Ti 2p regions. To obtain the elemental composition of the film, we used the relative sensitivity factors incorporated in the software, Casa XPS. The XPS scans were sensitive to only the ~20-30-nm-thick TiO_2 overlayer.

3.3 Results and Discussion

Figure 3.2 shows the IR difference spectra collected after the TTIP and $TiCl_4$ half-reaction cycles at a substrate temperature of (a) 150, (b) 175 and (c) 200 °C. In these difference spectra, an increase in absorbance is due to the chemisorption of the incoming precursor or the creation of new species due to surface reactions, while a decrease in absorbance is due to the consumption of the chemisorbed species in surface reactions during a half-reaction cycle. Specifically, for the TTIP half-reaction cycle, at each substrate temperature, we observed an increase in absorbance over 975-1200, 1300-1500, and 2800-3000 cm^{-1} regions, which have been assigned to the CO symmetric and anti-symmetric stretching modes, CH_x (x = 1,3) bending modes, and CH_x (x = 1,3) stretching modes, respectively, in the isopropoxy ligands of TTIP.[6,23] This indicates that over the temperature range of 150-200 °C, TTIP chemisorbs onto a Cl-terminated TiO_2 surface created during the previous $TiCl_4$ cycle. However, we were not able to

observe a corresponding decrease in the Ti-Cl stretching region at ~400 cm^{-1} [Ref. [27]], which was below the cutoff frequency for the MCT-A detector and the ZnSe IRC (~700 cm^{-1}). Thus, our IR

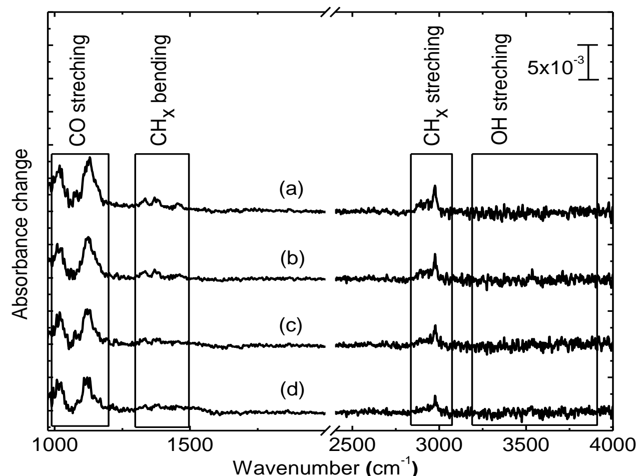

Figure 3.3. IR difference spectra showing the absorbance due to the various surface species involved in the ligand exchange reactions during TTIP (black) and $TiCl_4$ (red) half-reaction cycles at a substrate temperature of (a) 150, (b) 175 and (c) 200 °C. The almost identical change in absorbance during the two half-reaction cycles suggests a one-to-one ligand-exchange characteristic of an ALD process.

data is consistent with a surface reaction that produces isopropyl chloride ($(CH_3)_2CH$-Cl) as the primary product. Using a quadrupole mass spectrometer, Rahtu and Ritala also identified isopropyl chloride as a surface reaction product during the ALD of $Zr_xTi_yO_z$ using $ZrCl_4$ and TTIP as precursors.[16] In the following $TiCl_4$ half-reaction cycle (see Fig. 3.2) we observed a decrease in absorbance in the regions assigned to surface-chemisorbed TTIP and, as expected, there was no increase in absorbance in any other region of the IR spectrum. Therefore, we infer that the film's surface was again terminated with Ti-Cl, with isopropyl chloride being the surface

reaction product. The almost identical change in absorbance in both half-reaction cycles suggests a one-to-one ligand exchange, typical of an ALD process.

The onset of TTIP thermal decomposition is at 250 °C,[28] and therefore, direct decomposition of the isopropxy ligands can occur during ALD at the highest surface temperature studied (250 °C), especially during the purge period prior to the $TiCl_4$ cycle. Thermal

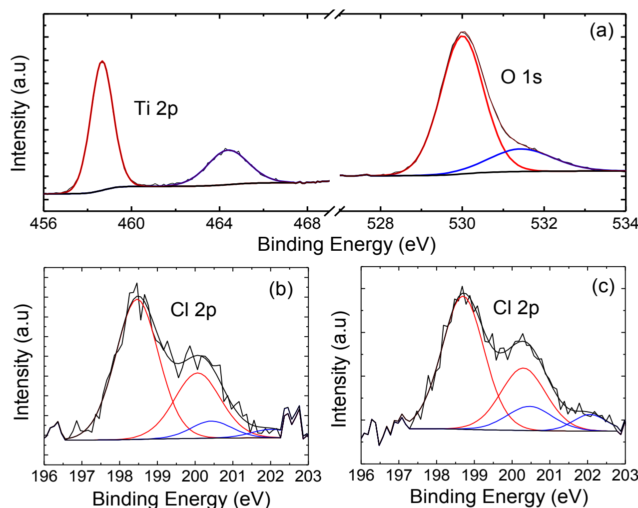

Figure 3.4. High-resolution XPS scans of TiO_2 films deposited via ALD. (a) Ti 2p, O 1s, and (b) Cl 2p regions for a film grown at 200 °C. (c) The Cl 2p region for a film grown at 225 °C. The O 1s peak was deconvoluted using Gaussian-Lorentzian (GL) peaks at 530.0 (red) and 531.4 (blue) eV corresponding to O boned to Ti and C, respectively. The Cl 2p region was fitted with four GL peaks corresponding to Cl bonded to Ti at 198.6 and 200.2 eV (red) and Cl bonded to C at 200.4 and 202.0 eV (blue). The energy scale in all the spectra was calibrated with respect to the adventitious C 1s peak at 285.0 eV.

decomposition of TTIP has been extensively studied on various surfaces: propene, acetone, isoprpopyl alcohol, water, and hydrogen have been reported as the major decomposition

products.[28] Furthermore, these studies conclude that TTIP decomposition depends on the carrier gas,[29] type of surface,[30–33] surface ligand coverage, and dose.[28,34] These factors influence the decomposition products as well as the decomposition temperature. To study the effect of TTIP decomposition on the reaction mechanism of the ALD process, we recorded IR difference spectra at regular intervals over a 10-min period after the completion of a TTIP cycle at 225 and 250 °C. While the surface was thermally stable at 225 °C, at 250 °C we observed a decrease in absorbance in the IR spectra in Fig. 3.3 in the CH_x ($x = 1,3$) and CO stretching regions indicating the thermal decomposition of the chemisorbed isopropoxy ligands. After 10 min, the surface isopropoxy ligands were not completely decomposed as can be seen by the IR absorbance in Fig. 3.3(d): if the isopropoxy ligands were indeed completely decomposed, absorbance in the CH_x and CO stretching regions in Fig. 3.3(d) would decrease down to the baseline. Thus, while thermal decomposition occurs at 250 °C, it is a slow process, and should not have a significant effect on the overall reaction over the time-scale of ALD half-reaction cycles. One of the decomposition pathways for TTIP is via the β-hydride elimination mechanism, which is expected to lead to the formation of surface –OH groups (see Fig. 3.1) and release of propene as a gas-phase product. However, in Fig. 3.3, we do not observe any surface -OH groups (3200-3800 cm^{-1}), which are known to be stable on a TiO_2 surface at 250 °C in H_2O-based ALD processes. [28,35] Thus, we further conclude that under our experimental conditions, the surface –OH groups could be eliminated via a reaction with undecomposed isopropoxy ligands to form isopropanol. Therefore, in our experiments propene and isopropanol should be the primary surface reaction products during the thermal decomposition of TTIP at 250 °C. Finally, based on our IR data, we conclude that over the temperature range of 150-250 °C, the ALD of TiO_2 from TTIP and $TiCl_4$

proceeds via a simple alkyl-transfer ligand-exchange mechanism (see Fig 3.1(a)) with isopropyl chloride as the surface reaction product during both ALD cycles.

To determine the film composition, growth rate, and optical properties, films deposited

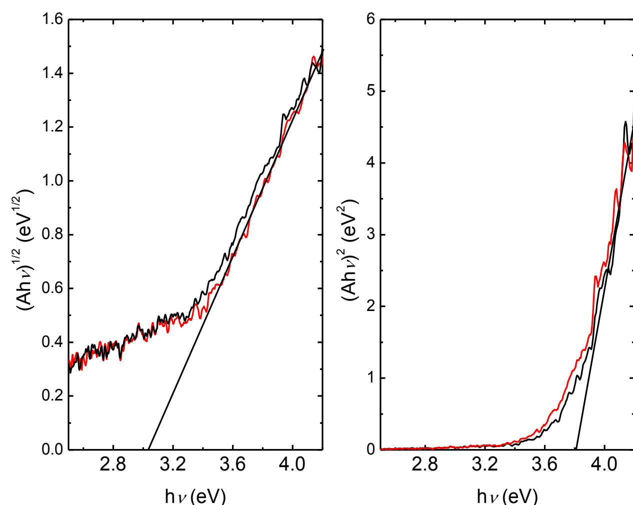

Figure 3.5. UV-Vis transmission spectra for TiO_2 films deposited at a substrate temperature of 200 (red) and 225 °C (black) plotted as (a) $(Ah\nu)^{1/2}$ and (b) $(Ah\nu)^2$ versus $h\nu$ to obtain the indirect and direct band gaps, respectively. At both temperatures, the indirect and direct band gaps were ~3.0 and ~3.8 eV, respectively, which are close to the values for amorphous TiO_2 reported in the literature.

on piranha-treated glass slides and TiO_2-pre-coated Si wafers were characterized *ex situ*. Using SE, we determined a growth per cycle of 0.7 Å at 200 °C for ALD on –OH terminated TiO_2 surfaces. Our data showed no significant nucleation period and a refractive index of 2.3 at 580 nm, which is comparable to TiO_2 ALD from other precursors. The growth per cycle for TTIP-$TiCl_4$ ALD was higher than what has been reported for TTIP-H_2O[36] and $TiCl_4$-H_2O[10] ALD, but comparable to TTIP-O_2 plasma ALD.[23] This is consistent with previous observation of Ritala and coworkers who also reported a higher growth per cycle when metal alkoxides were used at the

oxygen source during ALD of other metal oxides: A higher growth per cycle is expected for the TTIP-$TiCl_4$ ALD process as Ti is incorporated into the film during both half-reaction cycles.[19]

Figure 3.4 shows the XPS data for films deposited at 200 and 225 °C on piranha-treated glass slides. The energy scale in each spectrum was calibrated with respect to the adventitious C peak at 285.0 eV. Prior to data collection, the films were not sputtered with an Ar^+-ion beam to remove this adventitious surface C since preferential sputtering of O atoms over Ti results in a surface suboxide, which precludes accurate determination of the oxidation state of Ti in the film.[37] The Ti 2p, O 1s and Cl 2p peaks in Figure 3.4 were deconvoluted using Gaussian-Lozentian curves with a Shirley baseline.[37] Figure 3.4(a) shows the Ti 2p and O 1s region for a TiO_2 film deposited at 200 °C. The deconvolution of the Ti 2p region yielded two peaks centered at 458.7 and 464.4 eV assigned to Ti $2p_{3/2}$ and Ti $2p_{1/2}$, respectively,[38,39] for Ti atoms in the +4 oxidation state, indicating that there is no detectable suboxide. Deconvolution of the O 1s region also yielded two peaks centered at 530.0 and 531.4 eV, which were assigned to O atoms bonded to Ti and C, respectively.[38,40] We attribute the O 1s peak at 531.4 eV to primarily adventitious surface C as the IR data in Fig. 3.2 show complete removal of the TTIP ligands. Deconvolution of the Cl 2p region yielded four peaks consisting of two doublets ($2p_{3/2}$ and $2p_{1/2}$) separated by 1.6 eV [Fig. 3.4(b) and 3.4(c)]. The peaks centered at 198.6 and 200.4 eV were assigned to Cl bonded to Ti and C, respectively: [39] The Cl $2p_{3/2}$ peak at 200.4 eV can be attributed to surface hydrocarbons that react with a Cl-terminated surface, since the last ALD cycle in the growth process was a $TiCl_4$ dose. The Cl $2p_{3/2}$ peak at 198.6 eV was attributed primarily to the residual Cl in the bulk since it is expected that most surface Ti-Cl bonds would react with ambient species such as water and hydrocarbons. Therefore, a good estimate for the Cl content in the bulk film can be obtained based on the Cl $2p_{3/2}$ peak at 198.6 eV. The Cl content in the bulk film was

estimated to be 2.5 – 3.5% for films deposited over the range of 200 [Fig. 3.4(b)] to 225 °C [Fig. 3.4(c)]. The estimated percent Cl content in our TiO_2 films was within the range of 1-11% Cl reported by Ritala and coworkers for ALD of Al_2O_3 from $AlCl_3$ and $Al(OCH(CH_3)_2)_3$ over the temperature range of 225 – 275 °C.[19]

Finally, Figure 3.5 shows UV-Vis spectra for TiO_2 films deposited at 200 and 225 °C on piranha-treated glass slides. At both deposition temperatures, the indirect and direct band gaps of the films were determined to be ~3.0 and ~3.8 eV, respectively, which are very similar to the values previously reported in literature for amorphous TiO_2 films.[41]

3.4 Conclusions

We have demonstrated the ALD of TiO_2 using a combination of a metal halide and metal alkoxide as precursors without the use of an oxygen source such as H_2O, O_3, or an O_2 plasma. The surface reactions during the ALD process follow the alkyl-transfer mechanism over the temperature range of 150-250 °C. At 250 °C, TTIP starts to decompose thermally on the TiO_2 surface; however, this decomposition process is much slower than the alkyl-transfer reactions. The growth per cycle of 0.7 Å was higher than H_2O-based thermal ALD processes for TiO_2, since Ti atoms are incorporated into the film during both ALD cycles. The optical properties, such as the band gap and refractive index, of the deposited TiO_2 films were comparable to the values reported in the literature for amorphous TiO_2. This method of using a metal alkoxide as the oxygen source in ALD has been shown to mitigate the problem of interfacial oxide[15] and, hence, this ALD chemistry can enable deposition of TiO_2 on semiconductor substrates such as Ge that are susceptible to surface oxidation.

Acknowledgements

We gratefully acknowledge support from the NSF CAREER program (Grant No. CBET-0846923), the Colorado Revolutionary Solar Photoconversion, and the Eindhoven University of Technology. The authors would like to thank Dr. C. A. Wolden for support with the UV-Vis spectroscopy measurements and Dr. R. Morrish for the XPS measurements.

References

[1] S.M. George, Chem. Rev. **110**, 111 (2010).

[2] O. Sneh, R.B. Clark-Phelps, A.R. Londergan, J. Winkler, and T.E. Seidel, Thin Solid Films **402**, 248 (2002).

[3] Q. Xie, S. Deng, M. Schaekers, D. Lin, M. Caymax, A. Delabie, X. Qu, Y. Jiang, D. Deduytsche, and C. Detavernier, Semicond. Sci. Technol. **27**, 074012 (2012).

[4] P. Ardalan, E.R. Pickett, J.S. Harris, A.F. Marshall, and S.F. Bent, Appl. Phys. Lett. **92**, 252902 (2008).

[5] L. Wu and E. Eisenbraun, J. Vac. Sci. Technol. B **25**, 2581 (2007).

[6] V.R. Rai and S. Agarwal, J. Phys. Chem. C **112**, 9552 (2008).

[7] D. Kueck, P. Leber, A. Schmidt, G. Speranza, and E. Kohn, Diamond Relat. Mater. **19**, 932 (2010).

[8] A.A. Dameron, D. Seghete, B.B. Burton, S.D. Davidson, A. S. Cavanagh, J. A. Bertrand, and S.M. George, Chem. Mater. **20**, 3315 (2008).

[9] M. Leskelä and M. Ritala, Angew. Chem. Int. Ed. **42**, 5548 (2003).

[10] M. Ritala, P. Soininen, M. Leskel, E. Nykanen, L. Niinisto, E. Nykfinen, and L. Niinist, Thin Solid Films **225**, 288 (1993).

[11] V.R. Rai, V. Vandalon, and S. Agarwal, Langmuir **28**, 350 (2012).

[12] B.B. Burton, S.W. Kang, S.W. Rhee, and S.M. George, J. Phys. Chem. C **113**, 8249 (2009).

[13] V. Rai, V. Vandalon, and S. Agarwal, Langmuir **26**, 13732 (2010).

[14] Q. Xie, D. Deduytsche, M. Schaekers, M. Caymax, A. Delabie, X. Qu, and C. Detavernier, Appl. Phys. Lett. **97**, 112905 (2010).

[15] M. Ritala, K. Kukli, A. Rahtu, P. Raisanen, M. Leskelä, T. Sajavaara, and J. Keinonen, Science **288**, 319 (2000).

[16] A. Rahtu and M. Ritala, Langmuir **18**, 10046 (2002).

[17] C. Mui and C.B. Musgrave, J. Phys. Chem. B **108**, 15150 (2004).

[18] A. Rahtu, M. Ritala, and M. Leskelä, Chem. Mater. **13**, 1528 (2001).

[19] P. Raisanen, M. Ritala, and M. Leskelä, J. Mater. Chem. **12**, 1415 (2002).

[20] K. Kukli, M. Ritala, and M. Leskelä, Chem. Mater. **12**, 1914 (2000).

[21] W. Kim, S. Kang, and S. Rhee, J. Vac. Sci. Technol. A **21**, L16 (2003).

[22] V.R. Rai and S. Agarwal, J. Vac. Sci. Technol. A **30**, 01A158 (2012).

[23] V.R. Rai and S. Agarwal, J. Phys. Chem. C **113**, 12962 (2009).

[24] A. Kanta, R. Sedev, and J. Ralston, Langmuir **21**, 2400 (2005).

[25] Z. Huang, P. Wang, and A. MacDiarmid, Langmuir **7463**, 6480 (1997).

[26] N.G. Kubala, P.C. Rowlette, and C.A. Wolden, J. Phys. Chem. C **113,** 16307 (2009).

[27] Z. Wang and S. Sun, Chinese J. Polym. Sci. **6**, 359 (1988).

[28] A. Rahtu and M. Ritala, Chem. Vap. Deposition **8**, 21 (2002).

[29] K.L. Siefering and G.L. Griffin, J. Electrochem. Soc. **137**, 1206 (1990).

[30] Y.Y.-M. Wu, D.C. Bradley, and R.M. Nix, Appl. Surf. Sci. **64**, 21 (1993).

[31] K.L. Siefering and G.L. Griffin, J. Electrochem. Soc. **137**, 814 (1990).

[32] G. Battiston, R. Gerbasi, and M. Porchia, Thin Solid Films **239**, 186 (1994).

[33] H. Komiyama and T. Kanai, Chem. Lett. 1283 (1984).

[34] S. Cho, C. Chung, and S.H. Moon, J. Electrochem. Soc. **148**, C599 (2001).

[35] S. Bourgeois, F. Jomard, and M. Perdereau, Surf. Sci. **279**, 349 (1992).

[36] M. Ritala, M. Leskela, L. Niinisto, and P. Haussalo, Chem. Mater. **5**, 1174 (1993).

[37] A. Sonnenfeld, P.R. von Sonnenfeld, and R. Hauert, Plasma Chem. Plasma Process. **26**, 319 (2006).

[38] E. Magni and G. Somorjai, J. Phys. Chem. **3654**, 14786 (1996).

[39] S.R. Carlo, C.C. Perry, J. Torres, a. J. Wagner, C. Vecitis, and D.H. Fairbrother, Appl. Surf. Sci. **195**, 93 (2002).

[40] J.F. Moulder, W.F. Stickle, P.E. Sobol, and K.D. Bomben, *Handbook of X-ray Photoelectron Spectroscopy* (Physical Electronics, Inc, Minnesota 1995).

[41] V.M. Naik, D. Haddad, R. Naik, J. Benci, and G.W. Auner, Mat. Res. Soc. Symp. Proc. **755**, DD11.12.1 (2003).

CHAPTER 4

SINGLE-STEP PLASMA SYNTHESIS OF CARBON-COATED SILICON NANOPARTICLES

Based on a paper to be published in ACS Applied Materials & Interfaces

Rohan P. Chaukulkar,[1] Koen de Peuter,[2] Paul Stradins,[3] Svitlana Pylypenko,[4] Jacob P. Bell,[5] Yongan Yang,[5] and Sumit Agarwal[*1]

[1]Department of Chemical and Biological Engineering, Colorado School of Mines, Golden, Colorado, 80401

[2]Department of Applied Physics, Eindhoven University of Technology, 5600 MB Eindhoven, The Netherlands

[3]National Center for Photovoltaics, National Renewable Energy Laboratory, Golden, Colorado, 80401

[4]Department of Metallurgical and Materials Engineering, Colorado School of Mines, Golden, Colorado, 80401

[5]Department of Chemistry and Geochemistry, Colorado School of Mines, Golden, Colorado, 80401

Abstract

We have developed a novel single-step technique based on non-thermal, radio-frequency (rf) plasmas to synthesize sub-10-nm, core-shell, carbon-coated crystalline Si (*c*-Si) nanoparticles (NPs) for potential application in Li^+ batteries. Hydrogen-terminated *c*-Si NPs nucleate and grow in a SiH_4-containing, low-temperature plasma in the upstream section of a tubular quartz reactor. The *c*-Si NPs are then transported downstream by gas flow, and are coated with amorphous carbon (*a*-C) in a second C_2H_2-containing plasma. X-ray diffraction, X-ray photoelectron spectroscopy, and *in situ* attenuated total reflection Fourier transform infrared spectroscopy show that a thin, < 1 nm, 3C-SiC layer forms at the *c*-Si/*a*-C interface. By varying the downstream C_2H_2 plasma rf power, we can alter the nature of the *a*-C coating as well as the thickness of the interfacial 3C-SiC layer. The TEM analysis is in agreement with the Si NP core size determined by Raman spectroscopy, photoluminescence spectroscopy, and XRD analysis.

4.1. Introduction

Recent advances in portable electronics, mobile communication, and electric vehicles have increased the need for efficient energy storage and conversion devices.[1,2] Lithium-ion batteries (LIBs) due to their high energy and power density, high operating voltage, and low self-discharge and maintenance, are attractive candidates for energy storage.[1–8] To further improve the existing LIB technology, it is necessary to develop new materials that enable significantly higher charge capacities.[9,10] Silicon is considered one of the most promising anode materials for LIBs due to its high theoretical charge capacity (~4200 mAh/g), which is nearly ten times that for the conventional anode material, graphite (~372 mAh/g).[6–12] However, there are several challenges associated with the use of bulk Si as the anode material. Upon lithiation, Si

undergoes a significant volume expansion , ~300%,[6–15] and the resulting stress leads to electrode pulverization and a subsequent loss of electrical contact between the Si fragments.[6–15] Additionally, fresh electrode surfaces, created due to pulverization of Si during continuous expansion and contraction cycles, are exposed to the electrolyte resulting in electrolyte decomposition on the Si surface, and the formation of a thick solid electrolyte interface (SEI) layer.[7,8,11–14] These factors lead to a rapid decrease in battery capacity after the first few charging and discharging cycles. In addition, since the conductivity of Li^+ in Si is low, use of bulk Si leads to increased cycle duration.[16,17] Silicon nanostructures coated with carbon, have been proposed as a possible solution to circumvent these challenges, and numerous recent reports indicate promising results for carbon-coated Si nanostructures.[12,13,17–19] However, these nanostructures often require a complex synthesis route involving multiple steps.[12,13,18–20] Additionally, the critical size of the nanostructures under which crack initiation and propagation would become energetically unfavorable has not yet been accurately determined.[21–25] Recent reports suggest that sub-10-nm Si nanoparticles (NPs) may demonstrate better capacity retention.[25–27]

In this article, we describe a single-step, non-thermal, radio-frequency (rf) plasma synthesis technique for the growth of sub-10-nm, carbon-coated Si NPs. Previously, non-thermal plasma synthesis has been shown to be a scalable method for the synthesis of monodisperse, H-terminated, crystalline Si (*c*-Si) NPs with excellent control over their size.[28–31] To synthesize carbon-coated *c*-Si NPs, we employed two capacitively-coupled plasma sources in series in a tubular reactor. The *c*-Si NPs nucleate and grow in the upstream SiH_4-containing plasma with >90% feed gas depletion. These *c*-Si NPs were coated with amorphous carbon (*a*-C) downstream in flight in a C_2H_2-containing plasma. Optical emission spectroscopy (OES) data showed that the two plasma sources could be operated nearly independent of each other, which in turn enables

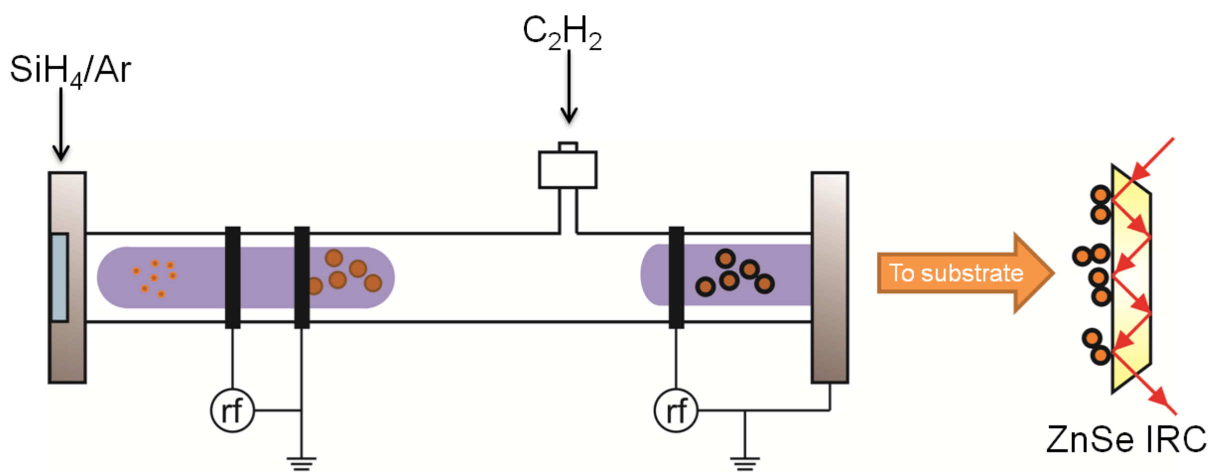

Figure 4.2. Schematic of the tubular reactor equipped with two radio-frequency, capacitively-coupled plasma sources used to synthesize carbon-coated *c*-Si NPs. The *c*-Si NPs were synthesized in the upstream plasma using SiH_4 heavily diluted in Ar. C_2H_2 was injected into the tube beyond the afterglow region of the SiH_4/Ar plasma. The as-synthesized *c*-Si NPs were transported by gas flow to the downstream C_2H_2 plasma, where they were coated in flight with amorphous carbon and collected onto a ZnSe internal reflection crystal for characterization using surface infrared spectroscopy.

independent control over the composition of the *a*-C coating. The size and size distribution of the H-terminated and carbon-coated *c*-Si NPs was determined using *ex situ* photoluminescence (PL) spectroscopy and transmission electron microscopy (TEM). Raman and *in situ* attenuated total reflection Fourier transform infrared (ATR-FTIR) spectroscopy show that the graphitic content of the *a*-C layer increased as rf power to the C_2H_2 plasma was increased. X-ray diffraction (XRD) and X-ray photoelectron spectroscopy (XPS) show that a 3C-SiC interlayer formed at the *c*-Si NP and *a*-C interface, and the thickness of this interlayer increased with increasing rf power to the downstream plasma source.

4.2. Experimental Details

4.2.1 Plasma synthesis setup

A schematic of the tubular quartz reactor used to synthesize the carbon-coated *c*-Si NPs is shown in Fig 4.1. The total length of the quartz tube between the two vacuum flanges, the external tube diameter, and the tube wall thickness were 340, 9.5, and 1 mm, respectively. The reactor was evacuated with a mechanical pump (Edwards E2M28) with a base pressure of ~6 mTorr. The two non-thermal, capacitively-coupled plasma sources were rf-powered at 13.56 MHz via π-type impedance matching networks. The *c*-Si NP synthesis technique was similar to the one reported previously by Kortshagen and coworkers.[28] The upstream plasma consisted of two Cu ring electrodes with an internal diameter and width of 9.5 and 10 mm, respectively. The rf-powered electrode was 50 mm from the upstream flange with the grounded electrode 30 mm further downstream from the rf-powered electrode. SiH_4 (1.4 standard cm^3/min (sccm)), heavily diluted in Ar (275 sccm), was injected upstream via mass flow controllers (see Fig. 4.1).[30–32] Previously, we have shown that at an rf power of 50 W in the upstream plasma, the depletion of SiH_4 was ~90%.[30] C_2H_2 (300 sccms) was injected through a MFC into the quartz tube beyond the afterglow region of the upstream SiH_4/Ar plasma, 18 cm from the upstream vacuum flange (see Fig. 4.1). The rf-powered Cu ring electrode for the second plasma source was placed 3 cm from the downstream vacuum flange, which was also used as the grounded electrode. The rf power to the C_2H_2 plasma was over the range of 40 - 135 W. The pressure was measured upstream using a capacitance manometer.

4.2.2 Plasma and surface diagnostics

OES data was recorded by sampling light through a quartz window placed upstream from the plasma (see Fig. 4.1). The emission intensities for the Ar ($2p_1 \rightarrow 1s_2$, 750.4 nm)[33] and C_2 radical ($A^3\Pi_g \rightarrow X^3\Pi_u$, 516.5 nm)[34] lines were monitored with and without downstream C_2H_2

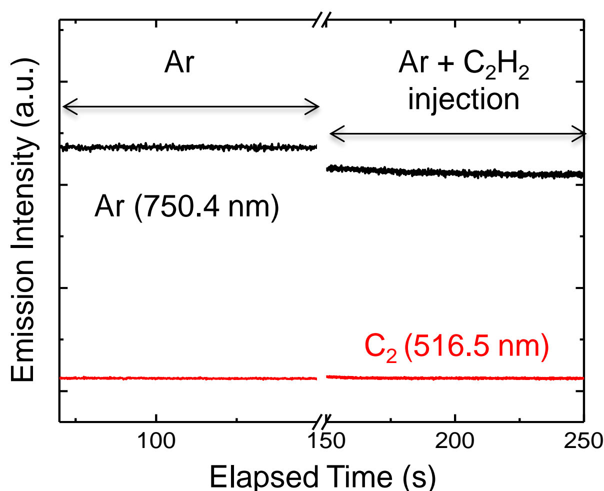

Figure 4.2. Optical emission spectra showing the effect of C_2H_2 injection on the upstream *c*-Si NP synthesis plasma. The emission intensities for the Ar and C_2 radical lines at 750.4 and 516.5 nm, respectively, were monitored in the upstream plasma prior to and after downstream C_2H_2 injection.

injection. The Si NPs were transported by gas flow into to an in-house-built surface analysis chamber equipped with an *in situ* ATR-FTIR spectroscopy setup.[35] The Si NPs were collected at room temperature onto a 50 × 10 × 1 mm trapezoidal ZnSe internal reflection crystal (IRC) with their short edges beveled at 45°. In the ATR mode, at room temperature, ZnSe is transparent in the infrared up to ~700 cm^{-1}. Infrared data was recorded over the spectral range of 700-4000 cm^{-1}

at a resolution of 4 cm^{-1} using 500 averages. All infrared spectra were recorded as difference spectra, where a reference spectrum was collected before the NPs were deposited onto the IRC. For *ex situ* characterization, the Si NPs were collected on to a *c*-Si(100) wafer placed adjacent to the ZnSe IRC. Photoluminescence studies were performed with excitation from a 365 nm laser diode (ThorLabs). PL from these Si NCs was collected through a 4.5" quartz viewport, and focused with a quartz lens into an Ocean Optics (QP1000-2-VIS-NIR) optical fiber that directed the light to a spectrometer (Si charge-coupled device, Ocean Optics) with a resolution of 0.36 nm. The PL spectra were corrected for the system response by calibrating with a tungsten lamp, which was at a temperature of 3100 K. The crystallinity of the carbon-coated Si NPs was characterized using XRD (Philips X'Pert Pro Diffractometer, Cu Kα source), the data was recorded with a resolution of 0.05º over $2\theta = 20 – 60º$. Raman spectroscopy (Jasco NRS-3100, 532 nm laser) and TEM (Philips (FEI) CM200) analysis were used to determine the size of the core of the Si NPs and the structure of the *a*-C coating. XPS analysis of the carbon-coated *c*-Si NPs was performed (Kratos Nova) with a monochromatic Al Kα source operated at 300 W. The *c*-Si NPs were pressed onto a non-conductive adhesive tape, and during acquisition of the spectra were subject to charge compensation using low energy electrons. Survey and high-resolution spectra of C 1s, O 1s, and Si 2p regions were acquired at pass energies of 160 and 20 eV, respectively. Data analysis was performed using the CasaXPS software, and included linear background subtraction, smoothing, charge referencing, and curve-fitting. The spectra were calibrated by setting the Au 4f to 84 eV. High-resolution Si 2p spectra were fitted with a series of Gaussian-Lorentzian functions. Each Si peak contains $2p_{3/2}$ and $2p_{1/2}$ components constrained to have ratio of 0.67 in area under the peak with a separation of 0.6 eV. Elemental concentrations

and distribution of species in the Si 2p spectra are reported as average values, based on analysis of three different areas on a sample.

4.3. Results and Discussion

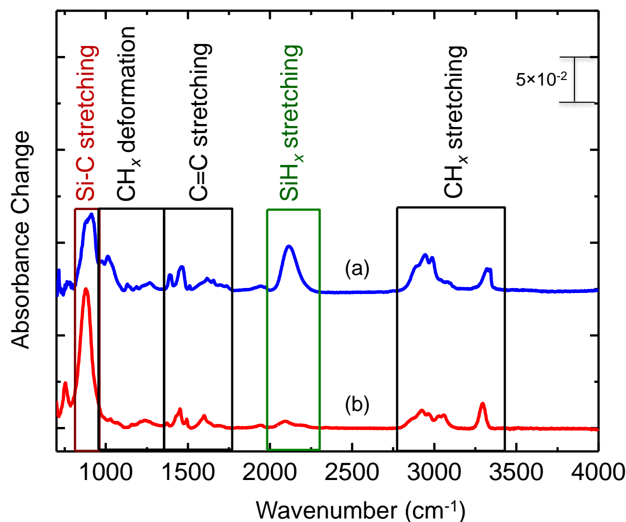

Figure 4.3. *In situ* infrared difference spectra for carbon-coated *c*-Si NPs grown at (a) 40 and (b) 90 W rf power to the downstream C_2H_2 plasma.

The OES data in Fig. 4.2 shows that injection of C_2H_2 downstream did not perturb the upstream SiH_4/Ar plasma significantly. The emission intensity of the C_2 line in the upstream plasma at 516.5 nm remained essentially unchanged suggesting minimal back diffusion of C_2H_2 or its radical fragments to the upstream *c*-Si NP synthesis plasma. Emission from the Ar line in the upstream plasma at 750.4 nm decreased in intensity by ~10%, most likely due to the change in the upstream pressure from 5.3 to 7.3 Torr upon injection of C_2H_2 downstream. Thus, the OES data in Fig. 4.2 confirms that the two plasma sources were operated nearly independent of each

other: H-terminated *c*-Si NPs were synthesized in the upstream plasma where SiH_4 was almost completely depleted, and these NPs were coated with *a*-C in the downstream C_2H_2 plasma. The size of the Si NPs synthesized using the non-thermal plasma technique has been shown to depend on the gas pressure.[29,36] To isolate the effects of the downstream C_2H_2 plasma, all the experiments in this work were performed at constant gas flow rates while varying only the C2H2 plasma rf power. Figure 4.3 shows in situ infrared spectra for carbon-coated c-Si NPs synthesized at 40 and 90 W rf power to the downstream C_2H_2 plasma. As reported previously, the surface of SiH_4-plasma-synthesized *c*-Si NPs is terminated with SiH_x ($x = 1, 2, 3$) groups.[30,37] As OES indicates no back diffusion of C_2H_2 to the upstream plasma, the *c*-Si NPs synthesized in the upstream plasma are also expected to be H-terminated. These H-terminated NPs are then carbon-coated in flight when exposed to reactive hydrocarbon radicals in the downstream C_2H_2 rf plasma. In addition to C_2H_2 gas, the downstream plasma contained Ar and a small fraction of SiH_4, which was injected upstream. When the C_2H_2 plasma was operated at 40 W rf power, the infrared spectrum (see Fig. 4.3, spectrum "a") shows a strong absorption band centered at ~2100 cm^{-1}, which was assigned to the SiH_x ($x = 1, 2, 3$) stretching mode.[30] This indicates that the surface of the *c*-Si NPs after carbon coating was still predominantly H-terminated. In addition, we also observed an increase in absorbance in the 750-950, 950-1400, 1400-1700, and 2800-3400 cm^{-1} regions, which have been assigned to the SiC stretching mode, CH_x deformation modes, C=C stretching modes, and CH_x stretching modes, respectively.[31,32,38–53] The presence of various C-containing species detected by infrared spectroscopy clearly suggests the formation of an *a*-C coating around the *c*-Si NPs in the downstream C_2H_2 plasma.[53–57] The CH_x stretching modes in the 2800-3400 cm^{-1} region were further categorized based on the hybridization of the C atom. The vibrational modes in the 2800-2980 and 2980-3100 cm^{-1} region were assigned to the

sp^3-and sp^2-hybridized CH_x species, respectively.[31,32,46–53,56] The CH_x stretching modes in the 3000-3100 cm^{-1} region were assigned to the aromatic sp^2-hybridized species. which indicates the formation of aromatic ring structures in the *a*-C coating around *c*-Si NPs.[32,46–48,50,53] The peak

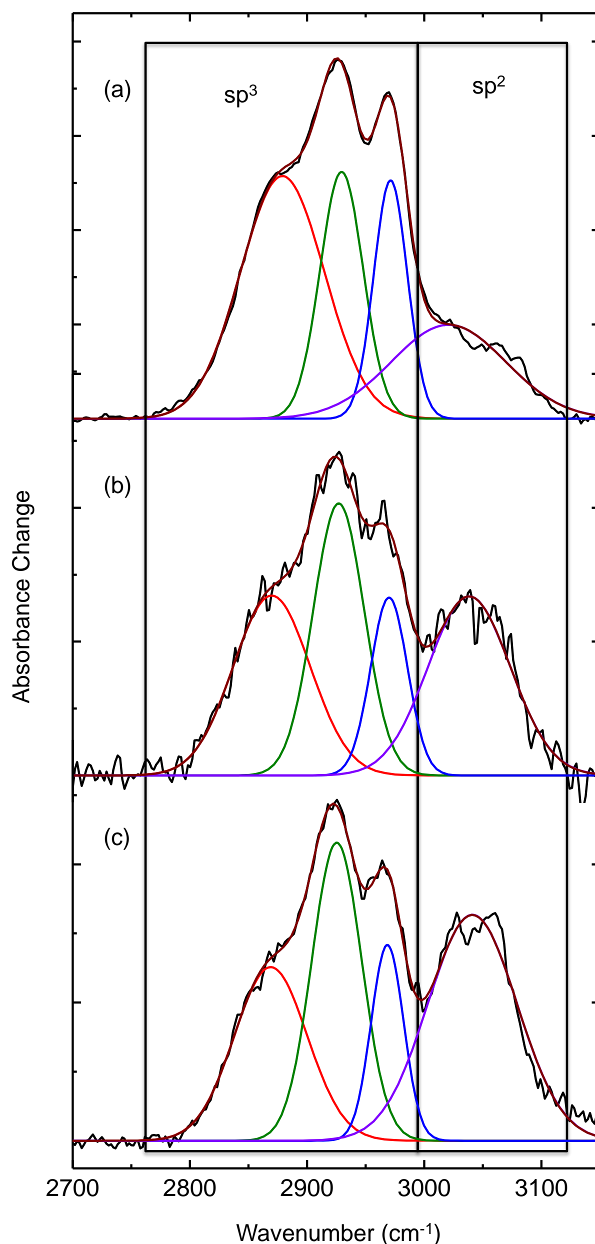

Figure 4.4. Infrared difference spectra showing the CH_x stretching region for carbon-coated *c*-Si NPs synthesized at (a) 40 W, (b) 60 W, and (c) 90 W rf power to the downstream C_2H_2 plasma.

The spectra were deconvoluted with four Gaussian line shapes. The ratio of the integrated absorbance of the sp^2-hybridized carbon to that of the sp^3-hybridized carbon increased with increasing downstream plasma rf power.

centered at ~3300 cm^{-1} was assigned to the CH stretching mode for sp-hybridized species indicating alkenyl termination of the surface of *c*-Si NPs, in addition to the SiH_x groups.[49,52] In addition, the SiC stretching vibration in the 750-950 cm^{-1} region was attributed to the transverse optical (TO) phonon mode of SiC.[38,39,41,42] Thus, the infrared spectrum in Figure 4.3 (spectrum "a") suggests that SiC is formed at the *c*-Si/*a*-C interface due to the reaction of hydrocarbon radicals with the H-terminated *c*-Si surface.

When the downstream C_2H_2 plasma was operated at higher rf power, 90 W, (see Fig 4.2, spectrum "b"), we observed almost no absorption in SiH_x stretching region at ~2100 cm^{-1} as compared to a strong absorption band in the 750-950 cm^{-1} region corresponding to the Si-C stretching mode in SiC. At higher rf power to the C_2H_2 plasma, the hydrocarbon radical density and the NP temperature are expected to be higher.[28,58] The reaction of these hydrocarbon radicals with the surface of *c*-Si NPs resulted in the formation of a significant amount of SiC on the NP surface at the *c*-Si/*a*-C interface, and almost complete consumption of surface SiH_x ($x = 1, 2, 3$) species. In addition, in spectrum "b" in Fig. 4.3, we also observed a change in the shape and relative intensities of the different CH_x and C=C stretching regions as compared to spectrum "a" in Fig. 4.3: this clearly indicates that changing the downstream plasma rf power from 40 to 90 W also affected the H-content and the sp^2/sp^3 hybridization ratio of the C atoms in the *a*-C coating. To study this effect of plasma power on the type of *a*-C layer deposited, we deconvoluted the CH_x stretching region for carbon-coated *c*-Si NPs synthesized at three different downstream

plasma rf powers – 40, 60, and 90 W (see Fig. 4.4). Deconvolution of the infrared spectra based on peak assignments in the literature enabled us to determine the relative changes in the concentration of the various hybridization states of the C atoms present in the *a*-C network. The infrared spectra were deconvoluted using four Gaussian line-shapes with peaks centered at ~2880, ~2930, ~2970, and ~3050 cm^{-1}. The peaks centered at ~2880 and ~2970 cm^{-1} were assigned to symmetric and antisymmetric stretching modes of CH_3, while the peak at ~2930 cm^{-1} was assigned to the symmetric stretching mode of sp^3-hybridized CH_2.[31,32,46–53,56] The peak at ~3050 cm^{-1} was assigned to the stretching mode for sp^2-hybridized CH.[32,46–48,50,53] The integrated absorbance for each of the deconvoluted vibrational modes (see Fig. 4.4) is directly proportional to corresponding bond density and its infrared absorption cross section.[31,32] Since the infrared absorption cross section of various CH stretching vibrations in *a*-C are not reported

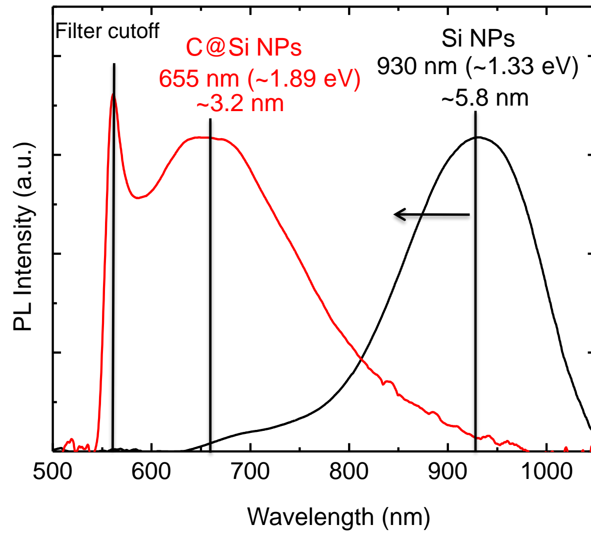

Figure 4.5. Normalized PL spectra for uncoated (black) and carbon-coated (red) c-Si NPs. The carbon coating was accompanied with the formation of a 3C-SiC at the c-Si/a-C interface, which

led to the consumption of surface Si, and a reduction in the size of the NP core. In the quantum confinement regime, this causes a blue-shift in the PL peak position.

in the literature, we estimated the sp^2-to-sp^3 hybridized C ratio in the *a*-C network by taking the ratio of total integrated absorbances of the sp^2 and sp^3 hybridized CH_x species. This ratio was 0.27, 0.43, and 0.60 at 40, 60, and 90 W, respectively, clearly indicating that the fraction of graphitic or aromatic sp^2 hybridized C content increased with the downstream plasma power, regardless of the infrared absorption cross section of the individual bands. According to previous reports in literature, the sp^2 content of *a*-C films was shown to increase upon thermal annealing due to the atomic H desorption from the sp^3-hybridized C atoms, and subsequent local restructuring to sp^2-hybridized C.[47,54,59–65] In our experiments, this observation can be explained based on the plasma-induced heating of the carbon-coated *c*-Si NPs due to the exothermic ion-electron and neutral-neutral recombination reactions that occur on the NP surface in a plasma environment.[28,30,58] Previous reports suggest that these exothermic reactions result in Si NP heating to temperatures that are sufficiently high for crystallization. The maximum temperature of the NPs in the plasma depends on the applied rf power.[28,30,58] Previously, we showed that heating of Si NPs in the plasma not only affects their crystallinity, but also affects the surface SiH_x (x = 1,2,3) composition, as the population of higher hydrides decreases due to their lower thermal stability.[30] Similarly, as the downstream C_2H_2 plasma rf power is increased, the core-shell NPs reach higher temperatures,[28,30,58] which leads to H-desorption from sp^3 C and thus a higher sp^2 C content in the *a*-C network. Our previous studies show that the PL emission energy from these *c*-Si NPs is consistent with quantum confinement effects, which results in a NP-size-dependent band gap.[30] Thus the emission energy can be used to estimate the average size of the *c*-Si NPs.[66–68] Figure 4.5 shows normalized PL spectra for *c*-Si NPs synthesized with the

downstream C_2H_2 plasma turned off, and carbon-coated *c*-Si NPs synthesized with the downstream C_2H_2 plasma operated at 90 W rf power. Since in both experiments the upstream NP

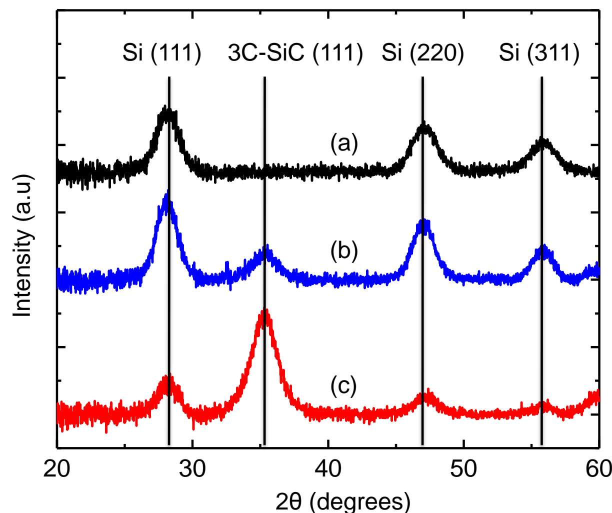

Figure 4.6. XRD patterns for the *c*-Si NPs grown at (a) 0, (b) 105, and (c) 135 W rf power to the downstream C_2H_2 plasma, but identical upstream plasma conditions. As the C_2H_2 plasma rf power was increased, the amount of 3C-SiC formed at the *c*-Si/*a*-C interface increased, which is indicated by the increase in the relative intensity of the 3C-SiC (111) diffraction peak compared to the Si (111) diffraction peak.

synthesis conditions were identical, we attribute the blueshift from 930 nm for the primarily H-terminated *c*-Si NPs to 655 nm for carbon-coated *c*-Si NPs to the consumption of the Si core due to reaction with *a*-C to form SiC: this is also consistent with the infrared data in Fig. 4.3, which shows infrared absorption due to the Si-C stretching vibrations.

Using accepted quantum confinement models for *c*-Si, this blueshift in emission corresponds to a reduction in the Si core size from ~5.8 to ~3.2 nm.[66] Additionally, when the

downstream C_2H_2 plasma was operated at the lowest rf power (40 W), we observed an absorbance band due to stretching vibrations of surface SiH_x (x = 1,2,3) (Fig 4.3, spectrum (a)) species suggesting all surface Si atoms in the core are not bonded to C atoms in the coating. However, when the C_2H_2 plasma power was increased to 90 W, almost all the surface SiH_x (x = 1,2,3) species were consumed indicating a denser shell structure (Fig 4.3, spectrum (a)). This suggests the C_2H_2 plasma has to be operated at high powers to ensure a dense coating. Hence, to determine the effect of the C_2H_2 plasma rf power on the carbon-coated Si NPs, all further characterization results presented below are for C_2H_2 plasma rf powers between 90-135 W.

To determine the structure of the interfacial SiC layer, we performed XRD analysis on Si NPs that were synthesized at different rf powers for downstream plasma, but otherwise identical process conditions. The diffractograms in Fig. 4.6 show that when the rf power to the downstream plasma was turned off, diffraction peaks appeared corresponding to the (111), (220), and (311) crystallographic planes of Si indicating the presence of *c*-Si NPs.[30] At 105 W rf power to the downstream C_2H_2 plasma (pattern (b)), we also observed an additional diffraction peak at $2\theta \approx 36°$, which corresponds to the (111) crystallographic plane of 3C-SiC.[44,69] Diffraction peaks corresponding to other crystallographic planes of 3C-SiC lie outside the range of measurements in Fig. 4.6. The presence of the 3C-SiC (111) peak in pattern "b" in Fig. 4.6 clearly suggests that a crystalline SiC layer forms at the *c*-Si/*a*-C interface in the downstream C_2H_2 plasma due to carburization of surface Si atoms in the Si NPs. When the downstream C_2H_2 plasma rf power was further increased to 135 W (see pattern (c)), we observes an increase in intensity for the 3C-SiC (111) peak as compared to the Si (111) peak showing that the extent of carburization of surface Si atoms increases at higher rf power to the C_2H_2 plasma: we attribute this increase in

surface carburization to a higher NP temperature[28,58] combined with a higher flux of hydrocarbon radicals to the NP surface. In multi-component mixtures, the integrated intensity of an XRD peak for a particular component depends upon its volume fraction in the mixture, the crystal structure parameters of the phase such as the structure and the multiplicity factors, and the linear absorption coefficient of the phase.[69] Therefore, by comparing the integrated intensities of the (111) peaks for Si and 3C-SiC we can quantitatively estimate the volume fractions of the two phases in the mixture using the expression in Eqn. 1.

$$\frac{I_{Si}(111)}{I_{SiC}(111)} = \left(\frac{|F_{Si}(111)|^2}{|F_{SiC}(111)|^2}\right)\left(\frac{L_{Si}}{L_{SiC}}\right)\frac{\mu_{SiC} v_{SiC}^2 V_{Si}}{\mu_{Si} v_{Si}^2 V_{SiC}}, \qquad (4.1)$$

In Eqn. 4.1 above, I is the integrated intensity of the diffraction peak, F is the structure factor, L is the Lorentz polarization factor, v is the volume of the unit cell, V is the volume fraction, and μ is the linear absorption coefficient. The subscripts in Eq. (1) indicate the crystalline material, and the parentheses contain the Miller indices for the crystallographic plane. The linear absorption coefficient for 3C-SiC, μ_{SiC}, was calculated based on the linear absorption coefficients of Si and C and their respective weight fractions in 3C-SiC according to Eq. (2) below,[69]

$$\left(\frac{\mu_{SiC}}{\rho_{SiC}}\right) = w_{Si}\left(\frac{\mu_{Si}}{\rho_{Si}}\right) + w_c\left(\frac{\mu_C}{\rho_C}\right), \qquad (4.2)$$

where, w is the weight fraction of Si or C in SiC, and ρ is the density. Thus, the expressions in Eq. (4.1) and (4.2), with $\mu_{Si}/\rho_{Si} = 65.32$ cm^2/g and $\mu_C/\rho_C = 4.219$ cm^2/g for Cu $K\alpha$ radiation,[69] can be used to determine the volume ratio of Si and 3C-SiC.

When the downstream C_2H_2 plasma rf power was turned off, using PL measurements (see Fig. 4.5), the average size of the *c*-Si NPs was estimated to be ~5.8 nm. As the two plasmas operate practically independent of each other, changing the downstream C_2H_2 plasma rf power would not affect the size of the *c*-Si NPs synthesized in the upstream plasma. Hence, the change in size of the *c*-Si NPs is almost entirely due to formation of the 3C-SiC shell in the downstream C_2H_2 plasma. Therefore, by calculating the volume fractions of the *c*-Si and 3C-SiC from the XRD patterns (see Eqns. (1) and (2)), we can estimate the size of the *c*-Si core and the thickness of the 3C-SiC shell. The quantitative XRD analysis shows that as the downstream C_2H_2 plasma rf power increased, the volume fraction of 3C-SiC also increased, which led to a decrease in the size of the *c*-Si core of the NPs. For the *c*-Si NPs synthesized at a C_2H_2 plasma rf powers of 105 and 135 W, we estimated the ~5.8-nm-diameter *c*-Si core was reduced to ~4.6 and 3.5 nm, respectively, due to carburization which results in a 3C-SiC layer of ~0.5 and 0.7 nm, respectively.

The *c*-Si NPs synthesized at 135 W C_2H_2 plasma rf power were further characterized via Raman spectroscopy (see Fig. 4.7 (a)). The Raman-active transverse optical phonon mode for bulk *c*-Si is at 521 cm^{-1}, which red-shifts in *c*-Si nanostructures due to phonon confinement.[70–72] Therefore, the position of the Raman band in nanostructured *c*-Si provides an estimate of the average size of the nanocrystals. The Raman spectrum in Figure 4.7(a) was deconvoluted over the 300-600 cm^{-1} region using a Lorentzian line shape for *c*-Si centered at ~510 cm^{-1} and a Gaussian line shape centered at ~450 cm^{-1} (see Fig. 4.7(b)). The red-shift in the *c*-Si phonon band from 521 to 510 cm^{-1} corresponds to *c*-Si NPs with an average core size of ~3.5 nm.[71,72] The peak at ~450 cm^{-1} was attributed to the bending modes of the sp-hybridized C present in the outermost *a*-C coating around the *c*-Si NPs.[73] Additionally, the Raman spectrum also contains a

distinct band over the 1100-2000 cm^{-1} region (see Fig. 4.7 (a)), which was deconvoluted using two Gaussian line shapes centered at ~1576 and ~1345 cm^{-1} assigned to the G and D bands of *a*-C (see Fig. 4.7(b)).[74–76]

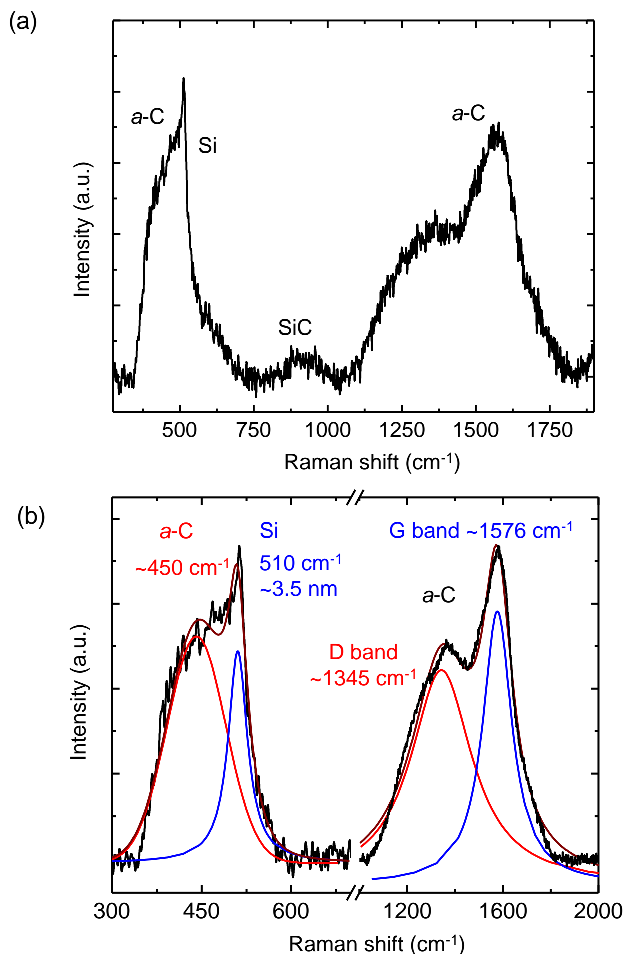

Figure 4.7. (a) Raman spectrum showing the presence of *c*-Si NPs, *a*-C, and 3C-SiC for carbon-coated *c*-Si NPs grown at 135 W rf power to the C_2H_2 plasma. (b) The *c*-Si region was fit using a Lorentzian line shape centered at 510 cm^{-1}, while the shoulder attributed to *a*-C, was fit with a Gaussian line shape centered at ~450 cm^{-1}. The *a*-C region was fit with a Lorentzian centered at ~1345 cm^{-1} (D band), and a Breit-Wigner-Fano line shape centered at ~1576 cm^{-1} (G band).

The G peak in the Raman spectrum for *a*-C is observed due to the sp^2 stretching vibrations of the aromatic or olefinic chain structures, while the D peak arises due to structural disorder, and requires the presence of six-membered aromatic rings.[74] Thus, the presence of the D band in the Raman spectrum confirms the presence of a graphitic fraction in the *a*-C coating.

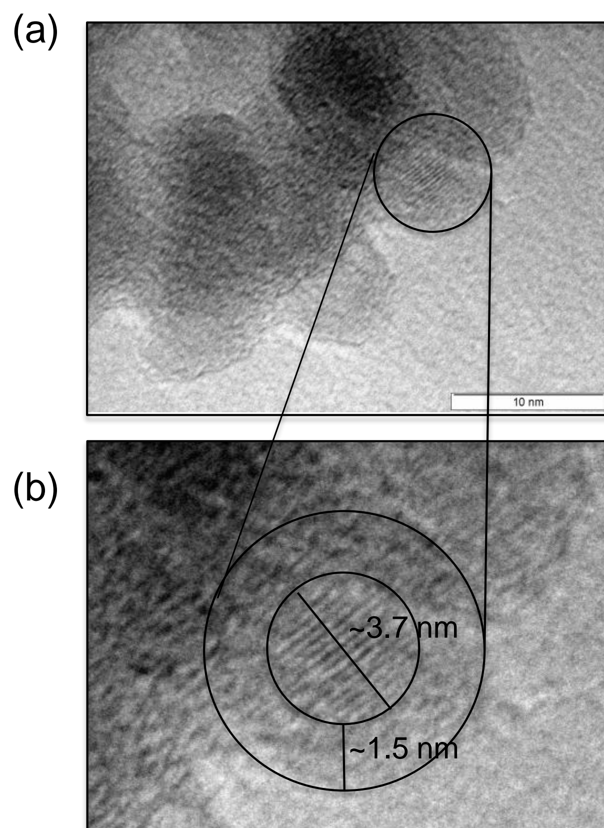

Figure 4.8. TEM images of carbon-coated *c*-Si NPs grown at 135 W rf power to the downstream C_2H_2 plasma. Image (b), which is a zoomed-in view of a particle that was observed in image (a), clearly shows a *c*-Si core of ~3.7 nm with a ~1.5-nm-thick coating.

Finally, in the Raman spectrum in Fig. 4.7(a), we also observed a band at ~940 cm^{-1}, which was assigned to the longitudinal optical phonon mode of 3C-SiC.[44] Thus, for the case of *c*-Si/*a*-C

core-shell NPs synthesized at 135 W rf power to the C_2H_2 plasma, the *c*-Si core size determined from the Raman analysis (~3.5 nm) agrees well with the size obtained from the PL (~3.2 nm) and XRD (~3.5 nm) analysis. Figure 4.8 (a) shows a TEM image of the *c*-Si NPs synthesized at C_2H_2 plasma power of 135 W. A zoomed-in view of image (a) is shown in image (b), which clearly shows a c-Si NP with a ~3.7 nm core with a ~1.5 nm coating. Thus, TEM analysis further

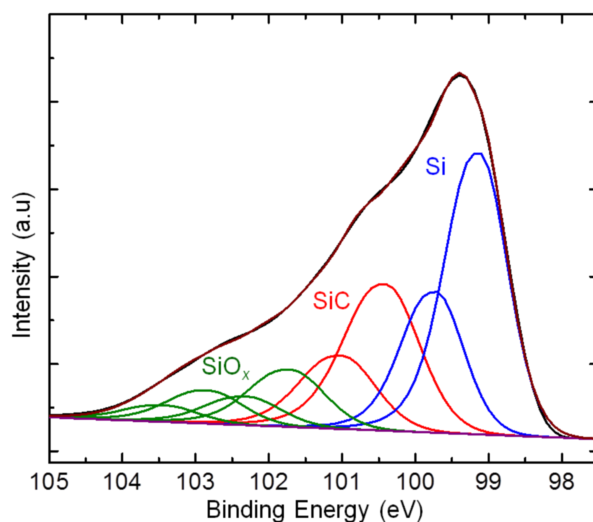

Figure 4.9. High resolution XPS scan of the Si 2p region for carbon-coated *c*-Si NPs synthesized at 135 W rf power to the C_2H_2 plasma.

confirms the size of the NPs as determined by Raman spectroscopy and XRD analysis. The quantitative XRD analysis combined with the TEM image analysis further allows us to estimate the composition of the coating around the *c*-Si core. In this particular experiment, from the XRD analysis we estimated that the thickness of the interfacial 3C-SiC layer was ~0.7 nm, which implies that the rest of the ~0.8 nm thick coating is the *a*-C film.

The elemental and chemical composition of the *c*-Si NPs was also obtained using XPS analysis. Since the size of the carbon-coated *c*-Si NPs is comparable to the escape depth of photoelectrons (~2-5 nm),[77] XPS analysis is not limited to just the surface of the NPs, but provides an estimate of the bulk composition. Given that the XPS analysis was performed *ex situ*, the surface of the *c*-Si NPs undergoes some degree of oxidation along with physisorption of hydrocarbons. Therefore, the carbon-coated *c*-Si NPs synthesized at 135 W rf power to the downstream C_2H_2 plasma show ~45 at.% C, 35 at.% Si, and 20 at.% O. A corresponding representative high-resolution Si 2p spectrum is shown in Figure 4.9, which was fitted with 4 sets of Gaussian-Lorentzian peaks, each consisting of two components, $2p_{3/2}$ and $2p_{1/2}$, separated by 0.6 eV. The $2p_{3/2}$ component of the first doublet is centered at 99.2±0.1 eV and attributed to elemental Si.[78,79] The second $2p_{3/2}$ component centered at 100.5±0.1 eV, and is due to SiC.[80,81] Doublets with $2p_{3/2}$ components located at 101.9 eV and 102.8 eV are due to various SiO_x species.[82–85] Based on these peak assignments, Si is present in these carbon-coated *c*-Si NPs primarily as elemental Si and SiC, with their respective concentrations of 45±5 % and 38.5 ±7 %, while the rest of the Si (~16.5±2 %) is bound to oxygen.

4.4.Conclusions

We have developed a single-step process to synthesize *a*-C-coated Si NPs < 10 nm in size using a dual-plasma setup. We have demonstrated that the sp^2-to-sp^3 hybridization ratio of the *a*-C coating as well as the thickness of the interfacial 3C-SiC layer can be manipulated through the downstream C_2H_2 plasma rf power, which in turn controls the hydrocarbon radical flux and plasma-induced heating of the NPs. The 3C-SiC layer has direct implications for the use of these NPs in LIBs. While 3C-SiC conducts Li ions, it does not undergo lithiation. Therefore, this

interfacial layer does not contribute to the lithiation capacity of the *a*-C-coated Si NPs thereby reducing the effective charge capacity of LIBs.[4] Hence, the downstream C_2H_2 plasma should be operated under conditions which results in a high graphitic content in the *a*-C coating while minimizing the amount of 3C-SiC formed.

Acknowledgements

We gratefully acknowledge support from the NSF CAREER program
(Grant No. CBET-0846923). KdP acknowledges support from the Eindhoven University of Technology. The authors would like to thank H. A. MacPherson and Dr. C. R. Stoldt at the University of Colorado for the Raman measurements, and the surface analysis group at the National Renewable Energy Laboratory for support and access to the XPS.

References

[1] M. Armand and J.-M. Tarascon, Nature **451**, 652 (2008).

[2] J.-M. Tarascon and M. Armand, Nature **414**, 359 (2001).

[3] Y. Hwa, W.-S. Kim, S.-H. Hong, and H.-J. Sohn, Electrochim. Acta **71**, 201 (2012).

[4] U. Kasavajjula, C. Wang, and A.J. Appleby, J. Power Sources **163**, 1003 (2007).

[5] J.B. Goodenough and Y. Kim, Chem. Mater. **22**, 587 (2010).

[6] M. Gu, Y. Li, X. Li, S. Hu, X. Zhang, W. Xu, S. Thevuthasan, D.R. Baer, J.-G. Zhang, J. Liu, and C. Wang, ACS Nano **6**, 8439 (2012).

[7] B. Liu, P. Soares, C. Checkles, Y. Zhao, and G. Yu, Nano Lett. **13**, 3414 (2013).

[8] H. Wu and Y. Cui, Nano Today **7**, 414 (2012).

[9] J. Graetz, C.C. Ahn, R. Yazami, and B. Fultz, Electrochem. Solid-State Lett. **6**, A194 (2003).

[10] Y.-S. Hu, R. Demir-Cakan, M.-M. Titirici, J.-O. Müller, R. Schlögl, M. Antonietti, and J. Maier, Angew. Chem. Int. Ed. Engl. **47**, 1645 (2008).

[11] M.-H. Park, M.G. Kim, J. Joo, K. Kim, J. Kim, S. Ahn, Y. Cui, and J. Cho, Nano Lett. **9**, 3844 (2009).

[12] M. Yoshio, H. Wang, K. Fukuda, T. Umeno, N. Dimov, and Z. Ogumi, J. Electrochem. Soc. **149**, A1598 (2002).

[13] H. Wu, G. Zheng, N. Liu, T.J. Carney, Y. Yang, and Y. Cui, Nano Lett. **12**, 904 (2012).

[14] H. Wu, G. Chan, J.W. Choi, I. Ryu, Y. Yao, M.T. McDowell, S.W. Lee, A. Jackson, Y. Yang, L. Hu, and Y. Cui, Nat. Nanotechnol. **7**, 310 (2012).

[15] C.K. Chan, H. Peng, G. Liu, K. McIlwrath, X.F. Zhang, R. a Huggins, and Y. Cui, Nat. Nanotechnol. **3**, 31 (2008).

[16] W.-R. Liu, Z.-Z. Guo, W.-S. Young, D.-T. Shieh, H.-C. Wu, M.-H. Yang, and N.-L. Wu, J. Power Sources **140**, 139 (2005).

[17] L. Cui, R. Ruffo, C. Chan, H. Peng, and Y. Cui, Nano Lett. **9**, 491 (2008).

[18] S.-H. Ng, J. Wang, D. Wexler, K. Konstantinov, Z.-P. Guo, and H.-K. Liu, Angew. Chem. Int. Ed. Engl. **45**, 6896 (2006).

[19] X. Li, P. Meduri, X. Chen, W. Qi, M.H. Engelhard, W. Xu, F. Ding, J. Xiao, W. Wang, C. Wang, J.-G. Zhang, and J. Liu, J. Mater. Chem. **22**, 11014 (2012).

[20] N. Liu, H. Wu, M.T. McDowell, Y. Yao, C. Wang, and Y. Cui, Nano Lett. **12**, 3315 (2012).

[21] I. Ryu, J.W. Choi, Y. Cui, and W.D. Nix, J. Mech. Phys. Solids **59**, 1717 (2011).

[22] X. Liu, L. Zhong, S. Huang, S. Mao, T. Zhu, and J. Huang, ACS Nano **6**, 1522 (2012).

[23] Z. Ma, T. Li, Y. Huang, J. Liu, Y. Zhou, and D. Xue, RSC Adv. **3**, 7398 (2013).

[24] K.E. Aifantis, S.A. Hackney, and J.P. Dempsey, J. Power Sources **165**, 874 (2007).

[25] H. Kim, M. Seo, M.-H. Park, and J. Cho, Angew. Chem. Int. Ed. Engl. **49**, 2146 (2010).

[26] C. Kim, M. Noh, M. Choi, J. Cho, and B. Park, Chem. Mater. **17**, 3297 (2005).

[27] Y. Xu, Q. Liu, Y. Zhu, Y. Liu, A. Langrock, M.R. Zachariah, and C. Wang, NANO Lett. **13**, 470 (2013).

[28] L. Mangolini, E. Thimsen, and U. Kortshagen, Nano Lett. **5**, 655 (2005).

[29] U. Kortshagen, J. Phys. D. Appl. Phys. **42**, 113001 (22 pp) (2009).

[30] B.N. Jariwala, N.J. Kramer, M.C. Petcu, D.C. Bobela, M.C.M. van de Sanden, P. Stradins, C. V Ciobanu, and S. Agarwal, J. Phys. Chem. C **115**, 20375 (2011).

[31] S.L. Weeks, B. Macco, M.C.M. van de Sanden, and S. Agarwal, Langmuir **28**, 17295 (2012).

[32] B.N. Jariwala, O.S. Dewey, P. Stradins, C. V Ciobanu, and S. Agarwal, ACS Appl. Mater. Interfaces **3**, 3033 (2011).

[33] D.L. Crintea, U. Czarnetzki, S. Iordanova, I. Koleva, and D. Luggenhölscher, J. Phys. D. Appl. Phys. **42**, 045208 (11 pp) (2009).

[34] Y.Y. Lin, H.W. Wei, K.C. Leou, H. Lin, C.H. Tung, M.T. Wei, C. Lin, and C.H. Tsai, J. Vac. Sci. Technol. B **24**, 97 (2006).

[35] V.R. Rai and S. Agarwal, J. Vac. Sci. Technol. A **30**, 01A158 (2012).

[36] R. Gresback, Z. Holman, and U. Kortshagen, Appl. Phys. Lett. **91**, 093119 (2007).

[37] L. Mangolini and U. Kortshagen, Adv. Mater. **19**, 2513 (2007).

[38] D. Basa and F. Smith, Thin Solid Films **192**, 121 (1990).

[39] W.K. Choi, Y.M. Chan, C.H. Ling, Y. Lee, R. Gopalakrishnan, and K.L. Tan, J. Appl. Phys. **77**, 827 (1995).

[40] W.K. Choi, F.L. Loo, F.C. Loh, and K.L. Tan, J. Appl. Phys. **80**, 1611 (1996).

[41] W. Spitzer, D. Kleinman, and C. Frosch, Phys. Rev. **113**, 133 (1959).

[42] D. McKenzie, J. Phys. D. Appl. Phys. **18**, 1935 (1985).

[43] M. Kuenle, S. Janz, O. Eibl, C. Berthold, V. Presser, and K.-G. Nickel, Mater. Sci. Eng. B **159-160**, 355 (2009).

[44] D. Song, E.-C. Cho, Y.-H. Cho, G. Conibeer, Y. Huang, S. Huang, and M.A. Green, Thin Solid Films **516**, 3824 (2008).

[45] D. Song, E.-C. Cho, G. Conibeer, Y.-H. Cho, Y. Huang, S. Huang, C. Flynn, and M.A. Green, J. Vac. Sci. Technol. B **25**, 1327 (2007).

[46] P. Honeybone, R. Newport, J. Walters, W. Howells, and J. Tomkinson, Phys. Rev. B **50**, 839 (1994).

[47] P. Couderc and Y. Catherine, Thin Solid Films **146**, 93 (1987).

[48] A. Grill and V. Patel, Appl. Phys. Lett. **60**, 2089 (1992).

[49] C. Huang, W. Widdra, X.S. Wang, and W.H. Weinberg, J. Vac. Sci. Technol. A **11**, 2250 (1993).

[50] D. McKenzie, R. McPhedran, N. Savvides, and D. Cockayne, Thin Solid Films **108**, 247 (1983).

[51] L.J. Webb, S. Rivillon, D.J. Michalak, Y.J. Chabal, and N.S. Lewis, J. Phys. Chem. B **110**, 7349 (2006).

[52] G. Socrates, *Infrared and Raman Characteristic Group Frequencies* (John Wiley & Sons Ltd., West Sussex, England, 2001).

[53] P.K. Chu and L. Li, Mater. Chem. Phys. **96**, 253 (2006).

[54] S.P. Louh, C.H. Wong, and M.H. Hon, Thin Solid Films **498**, 235 (2006).

[55] G. Le Dû, N. Celini, F. Bergaya, and F. Poncin-Epaillard, Surf. Coatings Technol. **201**, 5815 (2007).

[56] B.N. Jariwala, C. V. Ciobanu, and S. Agarwal, J. Appl. Phys. **106**, 073305 (2009).

[57] L. Zajíčková, S. Rudakowski, H. Becker, D. Meyer, M. Valtr, and K. Wiesemann, Thin Solid Films **425**, 72 (2003).

[58] N.J. Kramer, R.J. Anthony, M. Mamunuru, E.S. Aydil, and U.R. Kortshagen, J. Phys. D. Appl. Phys. **47**, 075202 (8 pp) (2014).

[59] M. Nadler, T. Donovan, and A. Green, Thin Solid Films **116**, 241 (1984).

[60] J. Gonzalez-Hernandez, B.S. Chao, and D.A. Pawlik, J. Vac. Sci. Technol. A **7**, 2332 (1989).

[61] P. Kelires, Phys. Rev. B **47**, 1829 (1993).

[62] R. Kalish, Y. Lifshitz, K. Nugent, and S. Prawer, Appl. Phys. Lett. **74**, 2936 (1999).

[63] A.C. Ferrari, B. Kleinsorge, N.A. Morrison, A. Hart, V. Stolojan, and J. Robertson, J. Appl. Phys. **85**, 7191 (1999).

[64] S. Takabayashi, K. Okamoto, H. Sakaue, T. Takahagi, K. Shimada, and T. Nakatani, J. Appl. Phys. **104**, 043512 (2008).

[65] F. Mangolini, F. Rose, J. Hilbert, and R.W. Carpick, Appl. Phys. Lett. **103**, 161605 (2013).

[66] G. Ledoux, O. Guillois, D. Porterat, C. Reynaud, F. Huisken, B. Kohn, and V. Paillard, Phys. Rev. B **62**, 15942 (2000).

[67] C.J. Murphy and J.L. Coffer, Appl. Spectrosc. **56**, 16A (2002).

[68] F.A. Reboredo, A. Franceschetti, and A. Zunger, Phys. Rev. B **61**, 13073 (2000).

[69] B. Cullity and S. Stock, *Elements of X-Ray Diffraction* (Prentice-Hall Inc. New Jersey, 2001).

[70] H. Richter, Z. Wang, and L. Ley, Solid State Commun. **39**, 625 (1981).

[71] C.M. Hessel, J. Wei, D. Reid, H. Fujii, M.C. Downer, and B.A. Korgel, J. Phys. Chem. Lett. **3**, 1089 (2012).

[72] G. Faraci, S. Gibilisco, P. Russo, A.R. Pennisi, and S. La Rosa, Phys. Rev. B **73**, 033307 (2006).

[73] C. Casari, A. Li Bassi, A. Baserga, L. Ravagnan, P. Piseri, C. Lenardi, M. Tommasini, A. Milani, D. Fazzi, C. Bottani, and P. Milani, Phys. Rev. B **77**, 195444 (2008).

[74] A. Ferrari and J. Robertson, Phys. Rev. B **61**, 14095 (2000).

[75] J. Schwan, S. Ulrich, V. Batori, H. Ehrhardt, and S.R.P. Silva, J. Appl. Phys. **80**, 440 (1996).

[76] C. Casiraghi, A. Ferrari, and J. Robertson, Phys. Rev. B **72**, 085401 (2005).

[77] D. Briggs and P. Seah, *Practical Surface Analysis: Auger and X-Ray Photoelectron Spectroscopy* (John Wiley and Sons, Chichester, 1990).

[78] S. Salimian and M. Delfino, J. Appl. Phys. **70**, 3970 (1991).

[79] T. Grehk, L. Johansson, S. Gray, M. Johansson, and A. Flodstrom, Phys. Rev. B **52**, 16593 (1995).

[80] M.P. Delplancke, J. Vac. Sci. Technol. A **9**, 450 (1991).

[81] L. Muehlhoff, W.J. Choyke, M.J. Bozack, and J.T. Yates, J. Appl. Phys. **60**, 2842 (1986).

[82] G. Hollinger, Appl. Surf. Sci. **8**, 318 (1981).

[83] W.A.M. Aarnink, A. Weishaupt, and A. van Silfhout, Appl. Surf. Sci. **45**, 37 (1990).

[84] R. Alfonsetti, G. De Simone, L. Lozzi, M. Passacantando, P. Picozzi, and S. Santucci, Surf. Interface Anal. **22**, 89 (1994).

[85] L.-A. O'Hare, B. Parbhoo, and S.R. Leadley, Surf. Interface Anal. **36**, 1427 (2004).

CHAPTER 5

PLASMA-ASSISTED SYNTHESIS OF CARBON-COATED GE AND SN NANOPARTICLES

Rohan P. Chaukulkar,[1] Koen de Peuter,[2] Jacob A. Ghodes,[1] Paul Stradins,[3] and Sumit Agarwal[*1]

[1]Department of Chemical and Biological Engineering, Colorado School of Mines, Golden, Colorado, 80401

[2]Department of Applied Physics, Eindhoven University of Technology, 5600 MB Eindhoven, The Netherlands

[3]National Center for Photovoltaics, National Renewable Energy Laboratory, Golden, Colorado, 80401

Abstract

We have developed a non-thermal plasma based technique to synthesize carbon-coated Ge and Sn nanoparticles (NPs) for potential application as high capacity anode materials in Li^+ batteries. We use two capacitively-coupled, radio frequency (rf) plasmas in series to synthesize these core-shell nanostructures. The use of two plasmas, which operate practically independent of each other, allows us separate control over the synthesis of the Ge or Sn NPs in the upstream plasma, and the structure and composition of the amorphous carbon coating in the downstream plasma. For the case of Ge, the a-C:H coating provides a conductive layer. While Sn NPs are conductive, the in-flight a-C:H coating was essential to prevent agglomeration of molten Sn NPs on the

substrate since the melting temperature of Sn is much lower than Ge. The reactor setup can be used to synthesize various core-shell nanostructures using different kinds of precursor sources.

5.1 Introduction

The combustion of fossil fuels leads to the emission of greenhouse gases which adversely affect the environment.[1,2] A large portion of these emissions is through the burning of fossil fuels in transportation vehicles which can be reduced by the use of electric vehicles.[3,4] However, this requires batteries with high capacities to power the vehicles over long distances. Of the various rechargable battery technologies, Li-ion batteries (LIBs) have some of the highest energy and power densities.[5–8] But before LIBs can be used in electric vehicles they need significant improvement in capacity, cost as well as durability. One way to improve the charge capacity of LIB is the use of novel anode materials with capacities significantly higher than the conventional anode material, graphite.[9–11] Theoretically, one atom of Si/Ge/Sn can react with 4.4 atoms of Li to form alloys of the stoichiometry $Li_{4.4}X$ (X - Si/Ge/Sn).[10,12] Thus, Si/Ge/Sn have significantly higher charge capacities than graphite. However, upon lithiation, these materials undergo a significant volume expansion, upto ~300%, which results in electrode pulverization due to the mechanical stress and a subsequent loss of battery capacity.[9–13] Compared to Si, Ge has ~15 times higher diffusivity of Li, and a lower specific volume change during the lithiation and delithiation cycles.[11,13] In addition, due to the minimal native oxide formation on Ge, Li-Ge is a model system to study group IV elements in LIB environments.[13] To prevent the loss in capacity in Ge/Sn based anodes, it has been proposed to use nanometer sized particles.[10,11,14] Additionally, to avoid local pulverization by generating uniform stress/strain over the entire electrode, the particles need to have a narrow size distribution.[10] Dispersing the particles in a conducting

matrix like carbon would lead to an efficient electrical contact thus sustaining battery capacity over a large number of cycles. Therefore, carbon-coated Ge/Sn nanoparticles are attractive

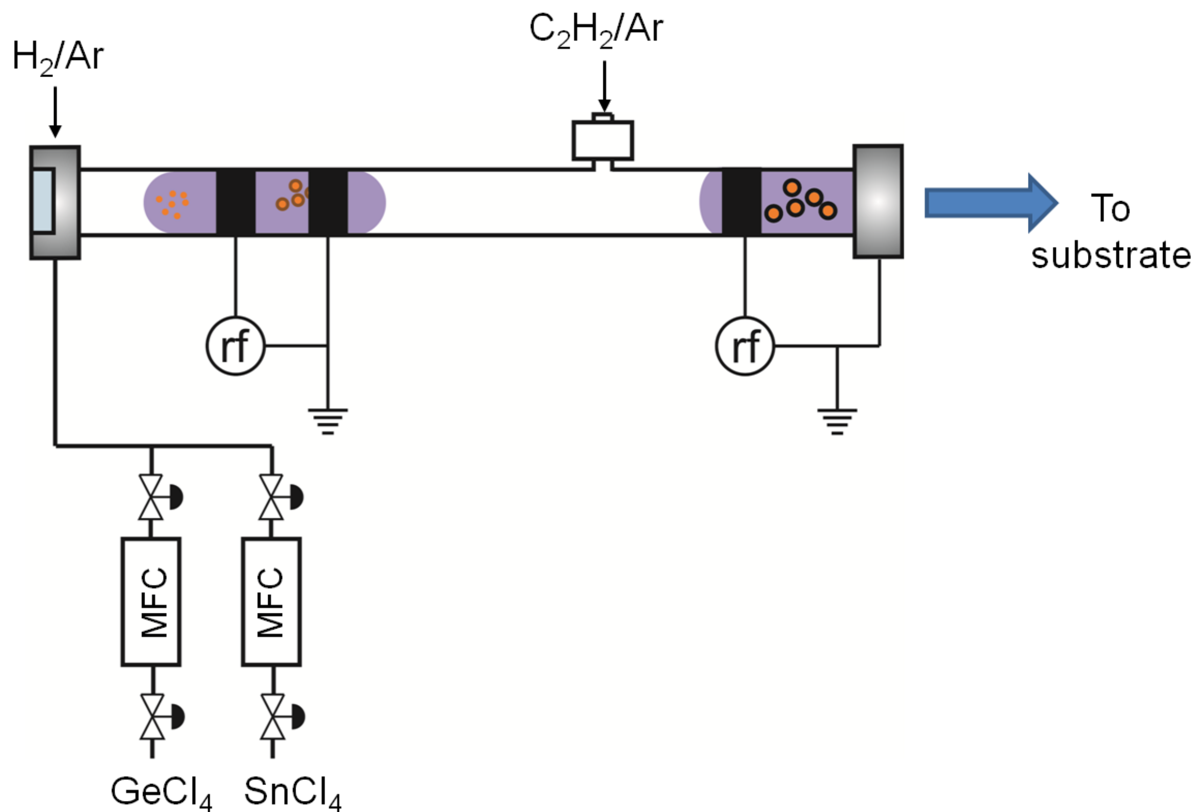

Figure 5.1. Schematic of the tubular quartz reactor used to synthesize *a*-C:H coated Ge and Sn NPs. The Ge and Sn NPs were synthesized in the upstream plasma using $GeCl_4$ and $SnCl_4$, respectively, diluted in a H_2-Ar gas mixture. The NPs are coated with *a*-C:H in the downstream C_2H_2-Ar plasma.

candidates for anode materials in LIBs.[10,11,15]

Here, we describe a versatile, single-step, non-thermal plasma based technique to synthesize carbon-coated Ge (Ge@C) as well as carbon-coated Sn (Sn@C) nanoparticles (NPs) using the same reactor setup. Non-thermal plasma synthesis has been previously shown to be a

scalable technique to synthesize monodisperse crystalline semiconductor NPs.[16,17] To synthesize carbon-coated Ge/Sn NPs, we employ two capacitively-coupled plasma sources in series in a tubular reactor. Previously, we have used a similar reactor setup to synthesize carbon-coated Si NPs using SiH_4 and C_2H_2 as precursors. Here, we have extended the technique to synthesize carbon-coated Ge/Sn NPs using chloride-based precursors. Ge/Sn NPs are first synthesized in the upstream plasma using $GeCl_4$/$SnCl_4$ as precursors. The as-synthesized Ge/Sn NPs are then transported by gas flow to the downstream C_2H_2 plasma where they are coated with *a*-C. The two plasmas operate practically independent of each other thus enabling us to control the nature of the carbon coating without affecting the core of the nanostructures. We have used infrared spectroscopy, X-ray diffraction (XRD) and Raman spectroscopy to study the core-shell structures. XRD analysis was used to characterize the morphology of the core of the nanostructures while infrared and Raman spectroscopy techniques were used to characterize the nature of the *a*-C coating. Our studies indicate that the graphitic nature of the *a*-C coating can be controlled by the applied rf plasma power to the downstream plasma, similar to our previous observation.

5.2 Experimental Setup

5.2.1 Nanoparticle synthesis setup

Schematic in Fig. 5.1 shows the tubular quartz reactor used to synthesize the Ge@C as well as the Sn@C NPs. The setup was similar to the one reported previously by Mangolini, Kortshagen, and coworkers for the synthesis of *c*-semiconductor NPs.[16,18] The reactor is equipped with two non-thermal, capacitively-coupled plasmas generated using rf power supplied via Cu ring electrodes. The quartz tube had an outer diameter and tube wall thickness of 9.5 mm

and 1 mm respectively, while the Cu ring electrodes had an inner diameter and width of 9.5 mm and 10 mm, respectively. The upstream plasma, generated by placing the rf-powered and grounded electrodes 60 and 90 mm, respectively, from the upstream vacuum flange, was primarily a NP synthesis plasma where pure Ge and Sn NPs were synthesized using $GeCl_4$ and $SnCl_4$ as precursors. C_2H_2 and Ar were injected into the tubular reactor beyond the afterglow region of the upstream plasma (90 mm downstream of the grounded electrode). The NPs synthesized in the upstream plasma were coated with *a*-C in the downstream plasma, which was generated by placing the rf-powered electrode 30 mm from the downstream flange. The downstream flange was used as the grounded electrode. The tube pressure was monitored using a capacitance manometer placed just upstream of the quartz tube.

5.2.2 Synthesis of Ge@C NPs

Pure Ge NPs were synthesized in the upstream plasma using a gas mixture of $GeCl_4$ (~1 sccm), H_2 (30 sccms), and Ar (200 sccms). The $GeCl_4$ (vapor pressure ~75 torr @ 20 °C) was delivered using a pressure-based mass flow controller (MKS 1640, Fig. 5.1) while the rest of the gases were delivered using thermal mass flow controllers (MKS 1640). The upstream plasma was operated at an applied rf power of 125 W. C_2H_2 (30 sccms) and Ar (300 sccms) were injected beyond the afterglow region of the upstream plasma. The NPs were transported by gas flow to the downstream plasma (operated at 60-90 W) where they were coated with *a*-C. The tube operating pressure was maintained at ~6.5 torr.

5.2.3 Synthesis of Sn@C NPs

The Sn NPs were synthesized in the upstream plasma using a gas mixture of $SnCl_4$ (~1 sccm), H_2 (15 sccms) and Ar (100 sccms). $SnCl_4$ (vapor pressure ~ 18 torr @ 20 °C) too was

delivered using a pressure-based mass flow controller. The upstream plasma was operated at an applied rf power of 25 W. C_2H_2 (30 sccms) and Ar (350 sccms) were injected beyond the afterglow region of the upstream plasma. The downstream plasma was operated at an applied rf power of 90 W and the tube was maintained at a pressure of ~7 torr.

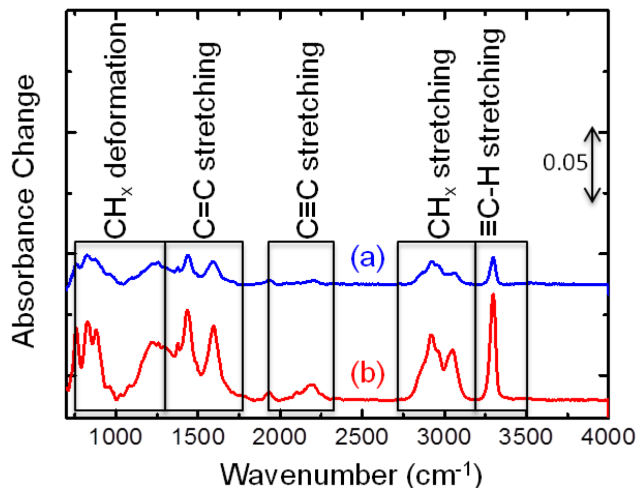

Figure 5.2. Infrared difference spectra of *a*-C coated Ge NPs synthesized at a downstream rf plasma power of (a) 60 W, and (b) 90 W.

5.2.3 NP characterization

The *a*-C coated NPs were collected on a Si (111) wafer for further *ex situ* characterization. Infrared data (Nicolet 6700) was recorded over the spectral range of 650-4000 cm^{-1} at a resolution of 4 cm^{-1} using 1000 averages. All infrared spectra were recorded as difference spectra, where a reference spectrum was collected using a bare Si wafer. The NPs were also characterized using X-ray diffraction (Philips X'Pert Pro Diffractometer, Cu Kα source), with the data recorded over 2θ = 20 - 65° with a resolution of 0.05°. Scherrer analysis was used to estimate the size of the NPs, with the full width at half maximum (FWHM) of the

diffraction peaks determined by fitting Gaussian line shapes. Raman spectroscopy (Jasco NRS-3100, 532 nm laser) was used to characterize the *a*-C coating deposited on the surface of the NPs.

5.3 Results and Discussion

Figure 5.2 shows the infrared difference spectra for *a*-C coated Ge NPs synthesized for different downstream rf plasma powers. Tube pressure and residence time in the reactor have been shown to affect the size of the as-synthesized NPs.[16–18] Therefore, to test the effect of the downstream C_2H_2 plasma on the surface of the as-synthesized NPs, the downstream rf plasma power was the only parameter varied in this work. C_2H_2 was injected downstream of the synthesis plasma at a position which ensured minimal back diffusion to the upstream synthesis plasma. This enabled the synthesis of pure Ge/Sn NPs in the upstream plasma which were then coated with *a*-C in the downstream C_2H_2 plasma. Infrared spectroscopy allows us to study the surface of these carbon-coated NPs. In Fig. 5.2 we see an increase in absorbance in the 950-1400, 1400-1700, 2000-2300, and 2800-3400 cm^{-1} regions which have been assigned to the CH_x deformation modes, C=C stretching modes, C≡C stretching modes, and the CH_x stretching modes, respectively.[19–24] This indicates the formation of *a*-C coating in the downstream C_2H_2 plasma. To further characterize the structure of the *a*-C coating we deconvoluted the CH_x stretching region based on the hybridization of the C atom. Figure 5.3 shows the deconvolution of the CH_x stretching regions, performed using Gaussian line-shapes, for carbon-coated Ge NPs synthesized at different downstream rf plasma powers. Based on the deconvolution, the vibrational modes in the 2800-2980 cm^{-1} region were assigned to sp^3-hybridized CH_x ($x = 1,2,3$) species while the modes in the 2980-3100 cm^{-1} region were assigned to the sp^2-hybridized CH_x

(x = 1,2) bonds. The integrated absorbance of an infrared peak is directly proportional to the bond density and the infrared absorption cross-section.[25,26] Therefore, we can compare the percent sp^2 content of the *a*-C coating synthesized at different downstream rf plasma powers by comparing the ratios of the total integrated absorbance of the sp^2 and sp^3 hybridized CH_x species. We found that the ratio of the integrated absorbance of the sp^2 modes to that of the sp^3 modes increased from 0.23 to 0.6 when the downstream rf plasma power was increased from 60 to 90 W. This indicates that the sp^2 (graphitic) content of the *a*-C coating increases with increasing downstream rf plasma power. Thermal annealing has been previously shown to increase the sp^2 content of *a*-C thin films.[19,23,27–30] The increase in sp^2 content of the films has been attributed to the thermal desorption of atomic H from sp^3 hybridized C in the *a*-C network and the subsequent rearrangement to sp^2 hybridization.[19,23,27–30] Therefore we propose that the increase in applied rf plasma power may lead to the NPs reaching a higher temperature in the plasma due to plasma-induced heating,[16,31] thus leading to a more graphitic content in the *a*-C coating. Similar observations were made by our group during the synthesis of carbon-coated Si NPs using a similar dual-plasma setup.

Figure 5.4 shows the XRD pattern for Ge NPs synthesized at a downstream rf plasma power of 90 W. The crystalline nature of the NPs is evident from the finite but narrow shape of the diffraction peaks at ~27.3, ~45.4 and ~53.8 °, which correspond to the (111), (220) and (311) crystallographic planes of Ge. Scherrer analysis was used to estimate the size of the NPs using the formula,[32]

$$d = \frac{k \cdot \lambda}{B \cdot \cos \theta_B}$$

where, d is the diameter of the particle, k is the correction factor assumed to be 0.9 for spherical particles, λ is the wavelength of the Cu Kα X-ray source, B is the FWHM of the diffraction peak,

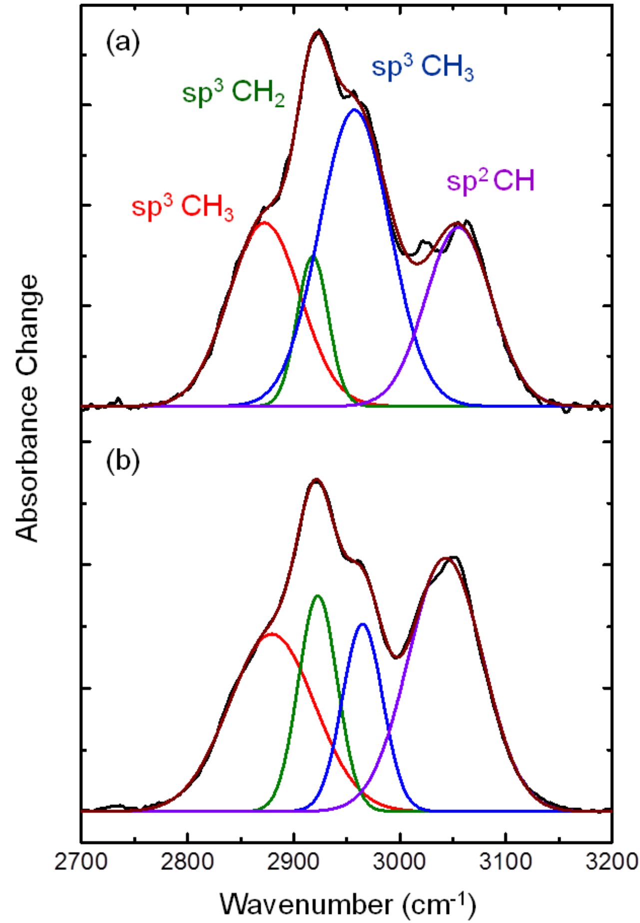

Figure 5.3. Infrared difference spectra of the CH_x stretching region for *a*-C coated Ge NPs synthesized at a downstream rf plasma power of (a) 60 W, and (b) 90 W. The peaks were fit using a Gaussian line shape. The ratio of the integrated absorbance of the sp^2 region to that of the sp^3 region was found to increase with an increase in downstream plasma power.

and θ_B is the Bragg angle for the diffraction peak. Using the above formula, the size of the Ge NPs was estimated to be ~4 nm.

The *a*-C coated Sn NPs were synthesized using the same reactor setup but with $SnCl_4$ as the precursor. The detailed procedure is explained above. Plasma-induced heating of the NPs has

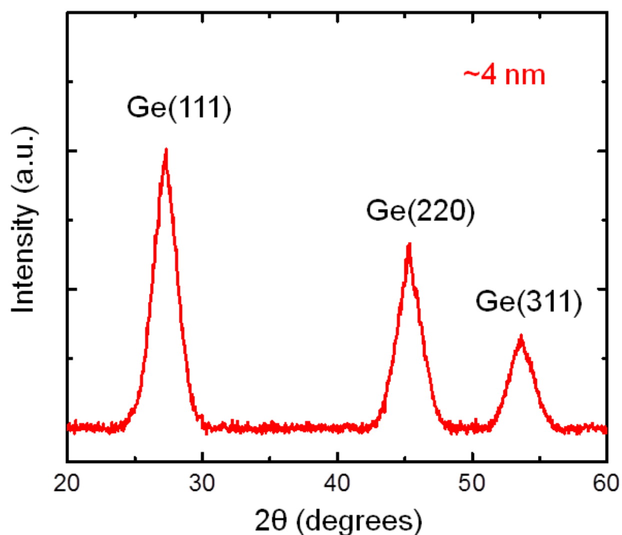

Figure 5.4: X-ray diffraction pattern of *a*-C coated *c*-Ge NPs synthesized at a downstream plasma power of 90 W. The position of the peaks corresponding to the (111), (220) and (311) crystallographic planes is similar to that in bulk *c*-Ge. The size of the NPs was estimated using Scherrer analysis.

been shown to occur in the non-thermal plasma environment.[31,33] The maximum temperature attained by the NPs in the plasma is dependent on the applied rf plasma power.[31,33] Since, metallic Sn has a relatively low melting point (~232 °C)[34] which is further reduced to <220 °C for 10 nm Sn NPs,[35] the upstream plasma had to be operated at low rf plasma powers (25 W) for the synthesis of Sn NPs. Operating the plasma at high powers lead to melting and subsequent agglomeration of the Sn NPs.

The XRD pattern for carbon-coated Sn NPs synthesized at a downstream rf plasma power of 90 W is shown in Fig. 5.5. The crystalline nature of the Sn NPs is evidenced from the

diffractions peaks at 30.6, 31.8, 43.7 and 44.6 °, corresponding to the (200), (101), (220) and (221) crystallographic peaks of metallic Sn with a tetragonal crystal structure.[32] The size of the

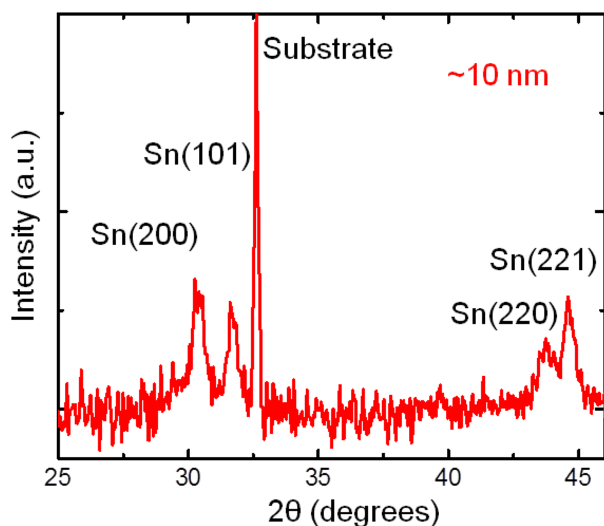

Figure 5.5. X-ray diffraction pattern of *a*-C coated 10 nm *c*-Sn NPs. Scherrer analysis was used to estimate the size of the NPs.

Sn NPs was estimated to be ~10 nm using Scherrer analysis.

Figure 5.6 shows the Raman spectrum for carbon-coated Sn NPs synthesized at a downstream rf plasma power of 90 W. The Raman peak over the 1200-1700 cm-1 region was deconvoluted using a Lorentzian line shape centered at ~1390 cm^{-1}, and a Breit-Wigner-Fano line shape centered at ~1585 cm^{-1} which were assigned to the D and G band of *a*-C respectively.[36,37] The graphitic nature of the *a*-C is confirmed by the presence of the D band, which arises due to structural disorder and requires the presence of six-membered aromatic rings. The G peak in the Raman spectrum for *a*-C is observed due to the sp^2 stretching vibrations of the aromatic or olefinic chain structures. We observed similar peaks during the Raman

characterization of the *a*-C coating when carbon-coated Si NPs were synthesized using a similar dual-plasma setup.

5.4 Conclusions

We have demonstrated a dual-non-thermal plasma technique to synthesize carbon-coated Ge and Sn NPs from chloride precursors. The single-step technique was previously used to

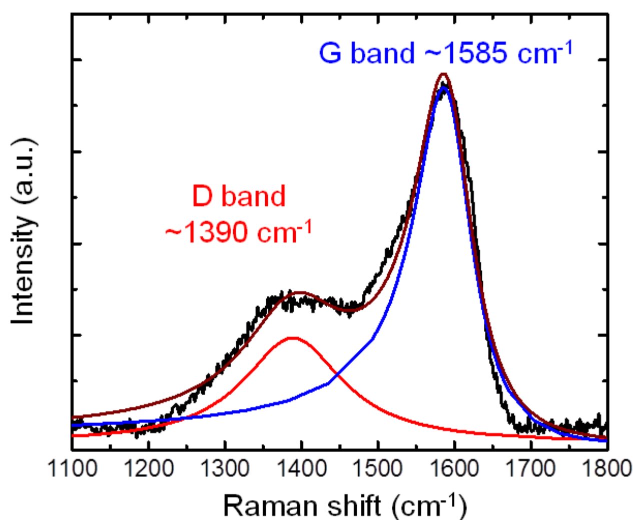

Figure 5.6. Raman spectrum of the *a*-C coating around the Sn NPs, synthesized at a downstream rf plasma power of 90 W. The two peaks were fit using the Lorentzian line shape centered at ~1390 cm^{-1} (D band), and a Breit-Wigner-Fano line shape centered at ~1585 cm^{-1} (G band).

synthesize carbon-coated Si NPs using SiH_4 as the precursor. This demonstrates the versatility of the setup to synthesize various core-shell nanostructures from different kinds of precursor sources. The use of two plasmas in series allows us to control the nature of the *a*-C coating independently of the synthesis of the NPs. Our results indicate that the graphitic content of the *a*-C coating increases on increasing the downstream rf plasma power. Thus, this technique allows

us to synthesize carbon-coated core-shell nanostructures which may be used in high capacity LIBs.

Acknowledgements

We gratefully acknowledge support from the NSF CAREER program (Grant No. CBET-0846923). KdP acknowledges support from the Eindhoven University of Technology. The authors would like to thank Dr. C. R. Stoldt at the University of Colorado for the Raman measurements, and the surface analysis group at the National Renewable Energy Laboratory for support and access to the XPS.

References

[1] C. A. Wolden, J. Kurtin, J.B. Baxter, I. Repins, S.E. Shaheen, J.T. Torvik, A. A. Rockett, V.M. Fthenakis, and E.S. Aydil, J. Vac. Sci. Technol. A **29**, 030801 (2011).

[2] J. Hansen, P. Kharecha, M. Sato, V. Masson-Delmotte, F. Ackerman, D.J. Beerling, P.J. Hearty, O. Hoegh-Guldberg, S.-L. Hsu, C. Parmesan, J. Rockstrom, E.J. Rohling, J. Sachs, P. Smith, K. Steffen, L. Van Susteren, K. von Schuckmann, and J.C. Zachos, PLoS One **8**, e81648 (2013).

[3] M.M. Thackeray, C. Wolverton, and E.D. Isaacs, Energy Environ. Sci. **5**, 7854 (2012).

[4] V. Etacheri, R. Marom, R. Elazari, G. Salitra, and D. Aurbach, Energy Environ. Sci. **4**, 3243 (2011).

[5] J.B. Goodenough and K.-S. Park, J. Am. Chem. Soc. **135**, 1167 (2013).

[6] J.B. Goodenough and Y. Kim, Chem. Mater. **22**, 587 (2010).

[7] J.-M. Tarascon and M. Armand, Nature **414**, 359 (2001).

[8] M. Armand and J.-M. Tarascon, Nature **451**, 652 (2008).

[9] U. Kasavajjula, C. Wang, and A.J. Appleby, J. Power Sources **163**, 1003 (2007).

[10] Y. Xu, Q. Liu, Y. Zhu, Y. Liu, A. Langrock, M.R. Zachariah, and C. Wang, NANO Lett. **13**, 470 (2013).

[11] G. Cui, L. Gu, L. Zhi, N. Kaskhedikar, P. a. van Aken, K. Müllen, and J. Maier, Adv. Mater. **20**, 3079 (2008).

[12] H. Wu and Y. Cui, Nano Today **7**, 414 (2012).

[13] J. Graetz, C.C. Ahn, R. Yazami, and B. Fultz, J. Electrochem. Soc. **151**, A698 (2004).

[14] M.G. Kim and J. Cho, J. Electrochem. Soc. **156**, A277 (2009).

[15] G. Derrien, J. Hassoun, S. Panero, and B. Scrosati, Adv. Mater. **19**, 2336 (2007).

[16] U. Kortshagen, J. Phys. D. Appl. Phys. **42**, 113001 (22 pp) (2009).

[17] R. Gresback, Z. Holman, and U. Kortshagen, Appl. Phys. Lett. **91**, 093119 (2007).

[18] L. Mangolini, E. Thimsen, and U. Kortshagen, Nano Lett. **5**, 655 (2005).

[19] P. Couderc and Y. Catherine, Thin Solid Films **146**, 93 (1987).

[20] A. Grill and V. Patel, Appl. Phys. Lett. **60**, 2089 (1992).

[21] C. Huang, W. Widdra, X.S. Wang, and W.H. Weinberg, J. Vac. Sci. Technol. A **11**, 2250 (1993).

[22] G. Socrates, *Infrared and Raman Characteristic Group Frequencies* (John Wiley & Sons Ltd., West Sussex, England, 2001).

[23] S.P. Louh, C.H. Wong, and M.H. Hon, Thin Solid Films **498**, 235 (2006).

[24] B.N. Jariwala, C. V. Ciobanu, and S. Agarwal, J. Appl. Phys. **106**, 073305 (2009).

[25] S.L. Weeks, B. Macco, M.C.M. van de Sanden, and S. Agarwal, Langmuir **28**, 17295 (2012).

[26] B.N. Jariwala, O.S. Dewey, P. Stradins, C. V Ciobanu, and S. Agarwal, ACS Appl. Mater. Interfaces **3**, 3033 (2011).

[27] M. Nadler, T. Donovan, and A. Green, Thin Solid Films **116**, 241 (1984).

[28] J. Gonzalez-Hernandez, B.S. Chao, and D.A. Pawlik, J. Vac. Sci. Technol. A **7**, 2332 (1989).

[29] R. Kalish, Y. Lifshitz, K. Nugent, and S. Prawer, Appl. Phys. Lett. **74**, 2936 (1999).

[30] S. Takabayashi, K. Okamoto, H. Sakaue, T. Takahagi, K. Shimada, and T. Nakatani, J. Appl. Phys. **104**, 043512 (2008).

[31] N.J. Kramer, R.J. Anthony, M. Mamunuru, E.S. Aydil, and U.R. Kortshagen, J. Phys. D. Appl. Phys. **47**, 075202 (8 pp) (2014).

[32] B. Cullity and S. Stock, *Elements of X-Ray Diffraction* (Prentice-Hall Inc. New Jersey, 2001).

[33] B.N. Jariwala, N.J. Kramer, M.C. Petcu, D.C. Bobela, M.C.M. van de Sanden, P. Stradins, C. V Ciobanu, and S. Agarwal, J. Phys. Chem. C **115**, 20375 (2011).

[34] G. Cui, Y. Hu, L. Zhi, D. Wu, and I. Lieberwirth, Small **3**, 2066 (2007).

[35] H. Jiang, K. Moon, H. Dong, F. Hua, and C.P. Wong, Chem. Phys. Lett. **429**, 492 (2006).

[36] A. Ferrari and J. Robertson, Phys. Rev. B **61**, 14095 (2000).

[37] J. Schwan, S. Ulrich, V. Batori, H. Ehrhardt, and S.R.P. Silva, J. Appl. Phys. **80**, 440 (1996).

CHAPTER 6

SINGLE-STEP NON-THERMAL PLASMA SYNTHESIS OF 3C-SIC NANOPARTICLES

Rohan P. Chaukulkar,[1] Koen de Peuter,[2] Jacob A. Ghodes,[1] Jacqueline E. Cloud,[3] Yongan Yang,[3] Svitlana Pylypenko,[4] Paul Stradins,[5] and Sumit Agarwal[1]

[1]Department of Chemical and Biological Engineering, Colorado School of Mines, Golden, Colorado, 80401

[2]Department of Applied Physics, Eindhoven University of Technology, 5600 MB Eindhoven, The Netherlands

[3]Department of Chemistry and Geochemistry, Colorado School of Mines, Golden, CO 80401

[4]Department of Metallurgical and Materials Engineering, Colorado School of Mines, Golden, CO 80401

[5]National Center for Photovoltaics, National Renewable Energy Laboratory, Golden, CO, 80401

Abstract

We present a scalable, single-step, non-thermal plasmas synthesis technique for the growth of sub-5-nm, amorphous carbon (*a*-C) coated 3C-SiC nanoparticles (NPs). We first nucleate and grow *c*-Si NPs in an upstream SiH_4/Ar plasma. These *c*-Si NPs are then transported by gas flow to a downstream C_2H_2/Ar plasma, and carburized in-flight by carbon-containing radicals and ions to 3C-SiC NPs. X-ray diffraction and transmission electron microscopy indicate a NP size

of ~4.2 nm. X-ray photoelectron spectroscopy analysis confirms that the *c*-Si NPs are completely carburized to 3C-SiC. Fourier transform infrared spectroscopy shows that the surface of the 3C-SiC NPs is coated with *a*-C with some alkenyl termination, which can facilitate further solution-based surface functionalization for biomedical applications.

6.1 Introduction

Silicon carbide (SiC) is a wide band gap semiconductor with excellent thermal, mechanical, and chemical properties including high thermal conductivity, mechanical strength, wear resistance, and corrosion stability.[1–3] As a result, SiC has applications in various fields such as high-power electonics,[4–6] light emitting diodes,[7,8] gas sensors,[6,9] and quantum-computing.[10,11] Quantum-confined SiC nanostructures with dimensions comparable to the Bohr exciton radius in SiC, ~2.7 nm,[12] show improved properties compared to the bulk form.[9,13] In particular, quantum-confined SiC nanoparticles (NPs) or quantum dots (QDs) show enhanced optical properties including a size-tunable band gap, and enhanced light absorption and emission compared to the bulk form.[14] Quantum confinement effects in 3C-SiC NPs have previously been observed over the size range of 1-6 nm.[15]

More recently, 3C-SiC QDs have been proposed as fluorescent probes in biomedical applications,[16–22] such as labeling and diagnostics.[17,23–25] Compared to the traditional organic flurophores, semiconductor quantum dots are highly photostable, i.e., they do not undergo photobleaching, have high absorption coefficients over a wide spectral range, and have size-tunable narrow emission spectra.[22,25–27] Compared to other semiconductor materials such as CdSe, which have also been proposed as candidates for biological labeling,[22,28,29] SiC is considered highly biocompatible and nontoxic. In previous studies, the biocompatibility of SiC

has been carefully demonstrated in orthopedic and dental implants.[1,27,30,31] In addition, is has been shown that SiC is chemically inert, and does not corrode in a biological environment.[1] Luminescence from 3C- as well as 6H-SiC QDs has also been reported previously within the context of numerous potential biomedical applications,[15,24,32–34] however, the controlled synthesis of SiC QDs that are <10 nm in diameter remains challenging.

Traditionally, SiC nanostructures have been synthesized via high-temperature, >1500 °C, carburization of SiO_2 nanostructures, which is an energy-intensive process.[35,36] The use of metal reducing agents, such as Mg or Na, has enabled the synthesis of SiC nanostructures from SiO_2 nanostructures via the carbothermal reduction process at temperatures as low as 600-700 °C.[37,38] However, these are multistep processes, which require nanostructured SiO_2 precursors as well as additional purification/separation steps to obtain the desired SiC nanostructures. The most common low-temperature method for the preparation of SiC NPs is the electrochemical etching of bulk SiC[15,23,32,39] followed by either sonication or milling to break down the porous layers formed after the etching step.[24,27] Using this method, 3C- or 6H-SiC NPs have been synthesized based on the polytype of the bulk SiC substrate. This synthesis technique, in addition to being a multistep process, also results in a wide size distribution, which in turn requires additional steps such as centrifugation to remove the larger particles and obtain a narrow size distribution (1-8 nm).[40] Besides electrochemical etching, there are only a few reports in the literature on the synthesis of SiC NPs that use low-temperature techniques, each with its own drawbacks. For example, electroless wet chemical etching[34] is a solution based technique with similar drawbacks as the electrochemical etching process. A low-temperature microwave plasma approach has been reported using tetramethylsilane as the single-source precursor. However, the authors reported amorphous SiC NPs,[9] which were non-stoichiometric. Another low-temperature synthesis

technique studied is laser-assisted chemical vapor deposition, where the agglomeration of the SiC NPs may be an issue.[41,42] Thus, a low-temperature single-step process is required to enable the synthesis of SiC QDs with the desired size and a narrow size distribution.

To this end, we report a commercially-scalable, single-step, non-thermal plasma synthesis technique to synthesize hydrogenated amorphous carbon (*a*-C:H) coated 3C-SiC NPs. In this synthesis method, we have used a tubular reactor with two plasma sources in series to synthesize *a*-C coated 3C-SiC NPs that are ~4.2 nm in size, using SiH_4 and C_2H_2 diluted in Ar as the growth precursors. In the first upstream plasma source, crystalline Si (*c*-Si) NPs were synthesized using a SiH_4/Ar mixture. These *c*-Si NPs were transported by gas flow into a second downstream C_2H_2/Ar plasma where they were completely carburized by hydrocarbon radicals to 3C-SiC NPs. We have characterized the NPs using Fourier transform infrared (FTIR) spectroscopy, X-ray diffraction (XRD), X-ray photoelectron spectroscopy (XPS), and transmission electron microscopy (TEM). The infrared data indicated that the surface of the 3C-SiC NPs was partially alkenyl terminated, which can facilitate further functionalization or solvation of these NPs for biomedical applications. XRD patterns show SiC NPs with only the 3C-SiC phase with a diameter of ~4.2 nm based on the Scherrer's analysis. The XPS data confirms that the SiC NPs were stoichiometric. TEM analysis showed that the NPs size is consistent with the Scherrer's analysis with a ~1-nm-thick *a*-C:H coating around the 3C-SiC core.

6.2 Experimental Setup

Figure 6.1 shows a schematic of the tubular plasma reactor used to synthesize the 3C-SiC NPs. The setup was similar to the one reported previously by Mangolini, Kortshagen, and

coworkers for the synthesis of *c*-Si NPs.[43,44] The reactor consists of a quartz tube with an outer diameter and tube wall thickness of 9.5 and 1 mm, respectively. The two non-thermal, capacitively-coupled plasmas were generated using radio-frequency (rf) power at 13.56 MHz supplied via Cu ring electrodes wrapped around the quartz tube. The Cu ring electrodes had an

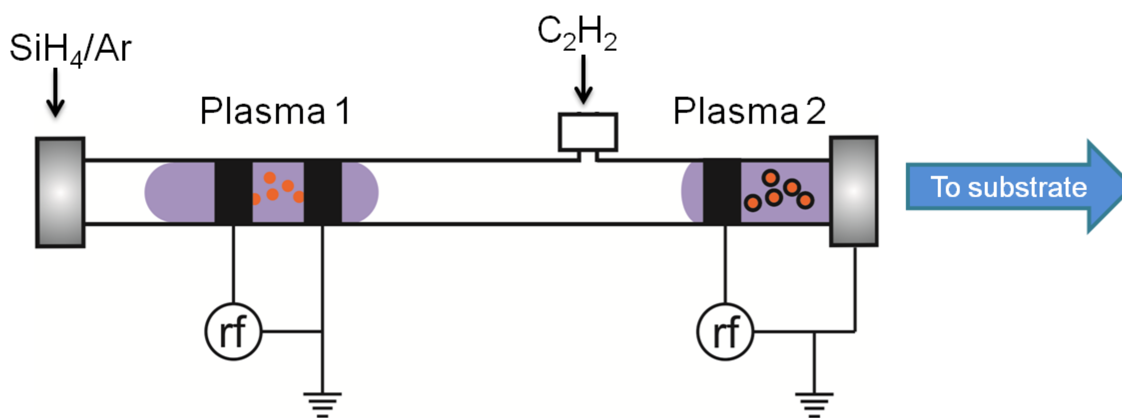

Figure 6.3. Schematic of the quartz tube plasma reactor used for the synthesis of 3C-SiC NPs using SiH_4 and C_2H_2 as precursors. The reactor is equipped with two capacitively-coupled rf plasma sources. *c*-Si NPs grow in the upstream SiH_4/Ar plasma, and are carburized in the downstream C_2H_2/Ar plasma to 3C-SiC NPs.

internal diameter and width of 9.5 and 10 mm, respectively. For the upstream plasma (denoted by Plasma 1 in Fig. 6.1), which was operated at an rf power of 50W, the rf-powered and grounded electrodes were placed 60 and 90 mm, respectively, from the upstream vacuum flange. A gas mixture containing SiH_4 (1.4 standard cm^3/min (sccm)) heavily diluted is Ar (275 sccm) was injected into the quartz tube via the upstream vacuum flange as shown in Fig. 6.1. C_2H_2 (150 sccm) was injected into the quartz tube, ~180 mm from the upstream vacuum flange, which was beyond the afterglow region of Plasma 1, and there was no back-diffusion of C_2H_2 or its radical fragments to the upstream SiH_4/Ar plasma.[45] For the downstream plasma (denoted by Plasma 2

in Fig. 6.1), which was operated at an rf power of 150 W, the rf-powered electrode was place 30 mm from the downstream vacuum flange, which acted as the grounded electrode. 3C-SiC NPs were synthesized at an operating upstream tube pressure of ~6.5 Torr. The 3C-SiC NPs were collected on a Si(100) wafer for further characterization.

The infrared spectra (Nicolet 6700) were recorded over the range of 650-4000 cm^{-1} at a resolution of 4 cm^{-1} using 1000 averages. All infrared spectra were recorded as difference spectra, where a reference spectrum was collected before the NPs were deposited onto the Si wafer. The NPs were additionally characterized using X-ray diffraction (Philips X'Pert Pro Diffractometer, Cu Kα source), with the data recorded over 2θ = 20 - 65° with a resolution of 0.05°. The full width at half maximum (FWHM) of the diffraction peaks was calculated by fitting Gaussian line shapes. X-ray photoelectron spectroscopy (XPS) analysis of the NPs was performed using a monochromatic Al Kα source (Kratos Nova) operated at 300 W. The NPs were pressed onto a non-conductive adhesive tape, and during data acquisition the NPs' surface was subject to charge compensation using low-energy electrons. A high-resolution scan of the Si 2p region was performed at a pass energy of 20 eV, and the data was analyzed using the CasaXPS software. The energy scale in the spectrum was calibrated by setting the Au 4f peak to 84.0 eV. The Si 2p region was fit with Gaussian-Lorentzian line shapes to include the $2p_{3/2}$ and $2p_{1/2}$ components. The $2p_{3/2}$ and $2p_{1/2}$ peaks were constrained to have an area ratio of 0.67, and a separation of 0.6 eV. TEM images were obtained on a Philips CM200 microscope. The TEM samples were prepared by dispersing the sample in ethanol (Pharmco-AAPER, ACS reagent from Fisher) using sonication, dropping that solution onto an Ultrathin carbon-coated copper grid (Ted Pella 01824), and then drying it in a vacuum desiccator.

6.3 Results

Figure 6.2 shows the infrared spectrum for the *a*-C:H coated 3C-SiC NPs. The spectrum

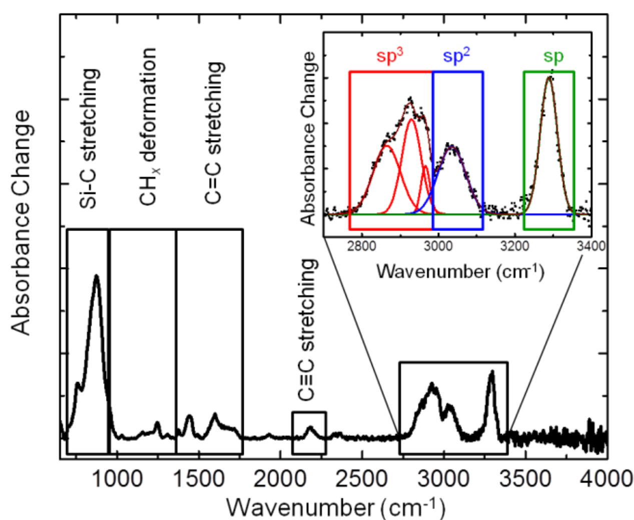

Figure 6.2. Infrared difference spectrum for 3C-SiC NPs. The formation of SiC is indicated by the transverse optical phonon mode of SiC in the 750-950 cm^{-1} region. Various vibrational modes assigned to the C-C and CH_x bonds show that an *a*-C:H coating exists around the NPs with a partial alkenyl termination. The structure of the *a*-C:H coating can be further characterized based on the hybridization of the C atoms as shown in the inset.

shows an absorption band in the 750-950 cm^{-1} region, which was assigned to the Si-C transverse optical (TO) phonon stretching mode in SiC.[46–49] In addition, the presence of *a*-C:H was confirmed by the increase in absorbance over the 950-1400, 1400-1700, 2130-2250, and 2800-3400 cm^{-1} regions, which have been assigned to the CH_x deformation modes, C=C stretching modes, C≡C stretching modes, and CH_x (x = 1,2,3) stretching modes, respectively.[50–55] The structure of the *a*-C:H coating was further characterized by carefully analyzing the different absorption bands in the CH_x (x = 1,2,3) stretching region (see inset in Fig. 6.2). Specifically, the

vibrational modes in the 2800-2980 cm^{-1} region were assigned to sp^3-hybridized CH_x ($x = 1,2,3$) species while the modes in the 2980-3100 cm^{-1} region indicate the presence of sp^2-hybridized CH_x ($x = 1,2$) bonds. The peak centered at ~3300 cm^{-1} was assigned to the stretching mode of sp-

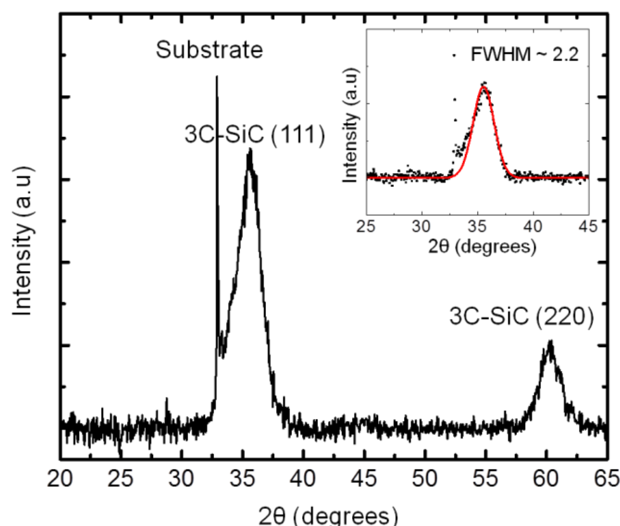

Figure 6.3. XRD pattern for *a*-C:H-coated 3C-SiC NPs. The (111) and (220) crystallographic planes of 3C-SiC indicate that the NPs are crystalline. The size of the NPs was estimated to be ~4.2 nm using Scherrer analysis. Inset shows the peak fit for the (111) peak using Gaussian line shapes. The sharp peak is due to the (200) reflection for the Si(100) wafer used as the substrate.

hybridized CH bonds.[52,53] Thus, the infrared data shows that the surface of the 3C-SiC NPs is coated with *a*-C:H with some alkenyl termination. Depending on the application, the alkenyl termination can facilitate further surface functionalization via solution-based processing.[17]

Figure 6.3 shows the X-ray diffraction pattern for the SiC NPs. The cubic phase of SiC is confirmed by the diffraction peaks observed at ~36° and ~60°, which correspond to the (111) and (220) crystallographic planes of 3C-SiC. The finite but narrow shape of the diffraction peaks indicates small NPs. The FWHM of the diffraction peaks was used to estimate the size of the

NPs using the Scherrer equation,[56,57] $d = k \cdot \lambda / B \cdot \cos\theta_B$, where d is the particle diameter, k is the correction factor assumed to be 0.9 for spherical particles, λ is the wavelength of the X-ray source, B is the FWHM of the diffraction peak, and θ_B is the Bragg angle for the diffraction peak. Using the Scherrer formula, the average size of the 3C-SiC NPs was estimated to be ~4.2 nm.

Figure 6.4 shows high-resolution XPS scans for the as-synthesized 3C-SiC NPs for the Si 2p region. Since the size of the NPs was comparable to the escape depth of the photoelectrons (~2-5 nm),[58] XPS analysis allowed us to directly probe the bulk composition of the NPs. The spectrum in Fig. 6.4 was deconvoluted with just two Gaussian-Lorentzian peaks with the constraints for the peak area ratio and separation stated in the previous section. Specifically, the peaks centered at 100.5±0.1 and 101.1±0.1 eV were assigned to Si $2p_{3/2}$ and Si $2p_{1/2}$ in SiC.[59,60] The results from XRD and XPS analysis were confirmed by TEM. Figure 6.5 (a) shows a TEM micrograph of the 3C-SiC NPs. Image (b) is a zoomed in view of the image (a), which shows a ~4.4 nm NP with a ~1.3 nm coating, which is in good agreement with the size of the 3C-SiC NPs estimated using the Scherrer equation.

6.4 Discussion

To our knowledge, this is the first report on the synthesis of 3C-SiC NPs using a low-temperature gas-phase technique. Interestingly, 3C-SiC NPs were only obtained in experiments with two plasma sources where *c*-Si NPs grown in the upstream SiH_4/Ar plasma were carburized to 3C-SiC in the downstream C_2H_2/Ar. In contrast, in experiments where SiH_4 and C_2H_2 were co-introduced into the upstream plasma with no downstream plasma, over a wide range of flow rates and rf power settings, no 3C-SiC powder was synthesized. Similarly, when rf power to the upstream plasma source (Plasma 1 in Fig. 6.1) was turned off, and only the downstream plasma

was operated at the same conditions and flow rates for all the gases as those described in the Experimental section, there was no growth of 3C-SiC NPs. Therefore, nucleation and growth of *c*-Si NPs indeed occurs first, which is followed by carburization to 3C-SiC NPs. Based on our

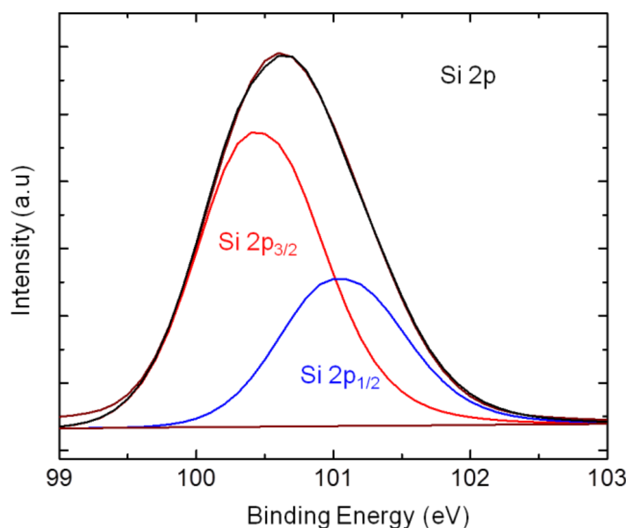

Figure 6.4. High-resolution XPS scan of the Si 2p region for *a*-C:H-coated 3C-SiC NPs synthesized using the dual-plasma setup.

experimental observations and previous studies on the synthesis of *c*-Si NPs, we propose the following growth mechanism for 3C-SiC NPs.

Using optical emission spectroscopy, we have previously shown with that there was minimal back-diffusion of C_2H_2 or its radical fragments to the upstream SiH_4/Ar plasma.[45] At very similar conditions in the upstream plasma, our previous measurements show that ~90% of the SiH_4 was consumed during the formation of the *c*-Si NPs or due to deposition of hydrogenated amorphous Si on the tube walls.[61] Since the second C_2H_2/Ar plasma contained only a small volume fraction of the undissociated SiH_4, the operating parameters for the two plasma sources could be set almost independent of each other. This suggests that the *c*-Si NPs,

which nucleate and grow in upstream plasma (see Fig. 6.1), are transported by gas flow into the downstream C_2H_2/Ar plasma where they are completely carburized by C-containing radicals and ionic species to form 3C-SiC NPs. Complete carburization of Si is confirmed by absence of any diffraction peaks corresponding to *c*-Si in the XRD pattern in Fig.6.3, and by the XPS data in Fig.6. 4, which shows no Si 2p peaks for Si^0. The size reported previously by our group for *c*-Si NPs grown at almost identical operating tube pressures was ~ 5 nm,[61] which translates to a 3C-SiC NP of ~4 nm upon carburization taking into account the difference in density and assuming the number of Si atoms in the NPs remains constant during carburization. This size estimate for the 3C-SiC NPs is very close to the size of ~4.2 nm obtained from the Scherrer analysis of the XRD pattern in Fig. 6.3 and the TEM image in Fig. 6.5.

Carburization of *c*-Si to SiC has been previously reported. Li and Ishigaki[62] performed in-flight carburization of micron-sized *c*-Si powder using a Ar-H_2-CH_4 high-temperature thermal plasma in an aerosol reactor. These authors reported incomplete carburization of the Si microstructures, which resulted in the formation of a uniform distribution of nano-sized SiC grains on the surface of *c*-Si core to form Si-SiC composites. Complete carburization of the Si nanostructures did not occur most likely due to the large *c*-Si particle size. Using a thermodynamic model, these authors predicted carburization proceeded via the reaction of liquid Si with carbon-containing species generated in the plasma, with the surrounding gas temperature between ~700-2700 ºC. Recently, Latu-Romain *et al.*[63] reported the conversion of *c*-Si nanowires (NWs) to 3C-SiC nanotubes through carburization at 1100 °C in a CH_4/Ar/H_2 environment. Tsakalakos *et al.*[64] performed thermal carburization of *c*-Si NWs using a C_3H_8/H_2 or CH_4/H_2 environment to synthesize SiC nanowires. They observed that higher temperatures and longer treatment times were needed to achieve complete carburization. The efficiency of carburization

of the Si NPs in our setup, even at the low residence times expected in the flow reactor, can be attributed to the highly reactive plasma environment as well as the small size (~5 nm) of the Si NPs synthesized in Plasma 1. It has previously been shown, that during the non-thermal plasma

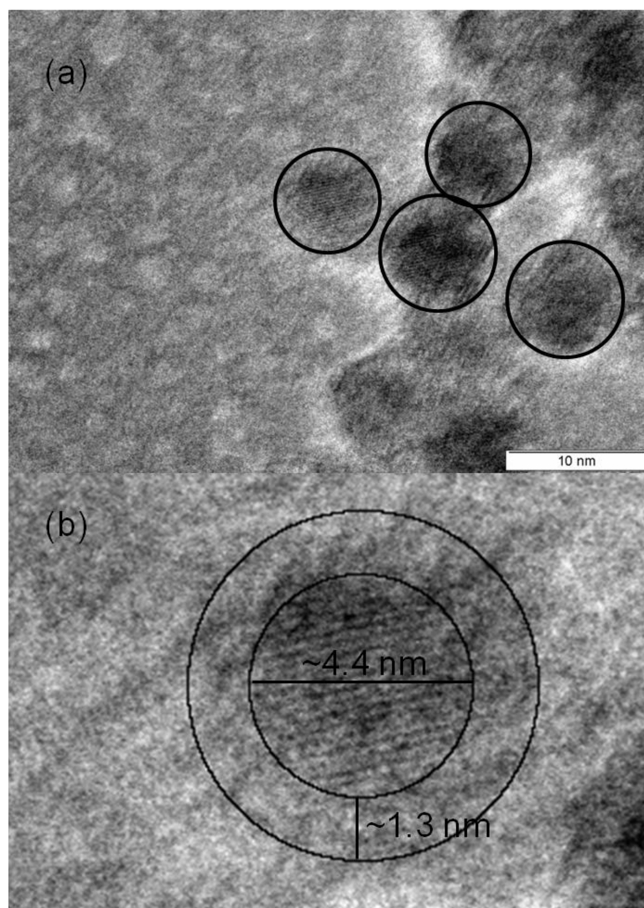

Figure 6.5. TEM images of *a*-C:H coated 3C-SiC nanoparticles. Image (b), which is a zoomed in view of a particle in image (a), shows a ~4.4 nm 3C-SiC core with a ~1.3 nm thick *a*-C:H coating.

synthesis of Si NPs, the size of the NPs can be controlled via the gas flow rates and pressure in the quartz tube reactor.[44] Therefore, by varying the upstream pressure in the reactor, the size of the Si NPs synthesized in Plasma 1 can be varied, and thus provides control over the size of the

resulting 3C-SiC NPs. Therefore, the ability to control the size of the NPs synthesized in Plasma 1 is a critical advantage of our synthesis technique.[44]

Crystallization of Si NPs synthesized in a non-thermal plasma environment has been investigated previously.[43,61,65,66] It has been proposed that exothermic ion-electron and neutral-neutral recombination reactions that occur on the Si NP surface in the plasma environment leads to heating of the NPs to temperatures high enough for crystallization.[65] On the other hand, Lopez and Mangolini recently studied the kinetics of the amorphous to crystalline transition in Si NPs, and concluded that plasma-induced heating alone would not explain the crystallization of these NPs in a low-temperature plasma environment.[66] Given this study, it is even more surprising that we obtained 3C-SiC NPs since the melting point of bulk 3C-SiC is almost twice that of bulk Si (melting point of Si = 1687 K, melting point of 3C-SiC = 3103 K). Irrespective of the crystallization mechanism, the formation of stoichiometric 3C-SiC NPs in a low-temperature process is a unique advantage of our synthesis technique. As a comparison, Lin and coworkers[9] previously synthesized SiC NPs using tertramethylsilicon as a single-source precursor in a non-thermal microwave plasma. These authors however reported amorphous SiC NPs that needed a further thermal annealing step for crystallization, which resulted in sub-stoichiometric carbon-rich SiC. Therefore, we speculate that it may be difficult to directly nucleate 3C-SiC NPs in a non-thermal plasma compared to growth of *c*-Si NPs, which can be readily carburized to 3C-SiC.

6.5 Summary

We have developed a scalable technique for the synthesis of *a*-C:H coated 3C-SiC NPs using a quartz tube reactor equipped with two non-thermal rf plasma sources. *c*-Si NPs nucleate

and grow in an upstream plasma, which uses a SiH_4/Ar gas mixture. These *c*-Si NPs are transported by gas flow to the downstream C_2H_2/Ar rf plasma source where C-containing radicals and ions carburize *c*-Si to 3C-SiC. When the rf power to the upstream plasma was turned off, no NP growth was observed in the downstream plasma at otherwise identical gas flow rates and pressure (6.5 Torr). The size of the 3C-SiC NPs, ~4.2 nm, was estimated using XRD and TEM analysis. This size is comparable to the Bohr exciton radius of SiC (2.7 nm), and thus within the size range where quantum confinement effects have been observed in SiC.[12] Therefore, this plasma synthesis technique can be used to synthesize 3C-SiC QDs for potential biomedical applications, such as fluorescent markers. The surface of the 3C-SiC NPs was partially alkenyl terminated, which can also facilitate further surface functionalization for biomedical applications.

Acknowledgements

We gratefully acknowledge support from the NSF CAREER program (Grant No. CBET 0846923). KdP acknowledges support from the Eindhoven University of Technology. The authors would also like to thank the surface analysis group at the National Renewable Energy Laboratory for support and access to the XPS.

References

[1] A. Oliveros, A. Guiseppi-Elie, and S.E. Saddow, Biomed. Microdevices **15**, 353 (2013).

[2] T. Sahu, B. Ghosh, S.K. Pradhan, and T. Ganguly, Int. J. Electrochem. **2012**, 1 (2012).

[3] R. Andrievski, Rev. Adv. Mater. Sci **22**, 1 (2009).

[4] C.R. Eddy and D.K. Gaskill, Science **324**, 1398 (2009).

[5] N.G. Wright, A.B. Horsfall, and K. Vassilevski, Mater. Today **11**, 16 (2008).

[6] C.I. Harris, S. Savage, A. Konstantinov, M. Bakowski, and P. Ericsson, Appl. Surf. Sci. **184**, 393 (2001).

[7] R.M. Potter, J. Appl. Phys. **40**, 2253 (1969).

[8] F. Fuchs, V. A. Soltamov, S. Väth, P.G. Baranov, E.N. Mokhov, G. V Astakhov, and V. Dyakonov, Sci. Rep. **3**, 1637 (2013).

[9] H. Lin, J. A. Gerbec, M. Sushchikh, and E.W. McFarland, Nanotechnology **19**, 325601 (2008).

[10] V.A. Soltamov, A.A. Soltamova, P.G. Baranov, and I.I. Proskuryakov, Phys. Rev. Lett. **108**, 226402 (2012).

[11] Y. Liu, G. Wang, S. Wang, J. Yang, L. Chen, X. Qin, B. Song, B. Wang, and X. Chen, Phys. Rev. Lett. **106**, 87205 (2011).

[12] J.Y. Fan, X.L. Wu, P.Q. Zhao, and P.K. Chu, Phys. Lett. A **360**, 336 (2006).

[13] P. Mélinon, B. Masenelli, F. Tournus, and A. Perez, Nat. Mater. **6**, 479 (2007).

[14] T. Takagahara and K. Takeda, Phys. Rev. B **46**, 578 (1992).

[15] X. Wu, J. Fan, T. Qiu, X. Yang, G. Siu, and P. Chu, Phys. Rev. Lett. **94**, 026102 (2005).

[16] X. Michalet, F. Pinaud, L. Bentolila, and J. Tsay, Science **307**, 538 (2005).

[17] D. Beke, Z. Szekrényes, D. Pálfi, G. Róna, I. Balogh, P.A. Maák, G. Katona, Z. Czigány, K. Kamarás, B. Rózsa, L. Buday, B. Vértessy, and A. Gali, J. Mater. Res. **28**, 205 (2012).

[18] M. Bruchez, M. Moronne, P. Gin, S. Weiss, and A. P. Alivisatos, Science **281**, 2013 (1998).

[19] F. Erogbogbo, K. Yong, I. Roy, and G. Xu, ACS Nano **2**, 873 (2008).

[20] M. De, P.S. Ghosh, and V.M. Rotello, Adv. Mater. **20**, 4225 (2008).

[21] J.M. Klostranec and W.C.W. Chan, Adv. Mater. **18**, 1953 (2006).

[22] A.P. Alivisatos, W. Gu, and C. Larabell, Annu. Rev. Biomed. Eng. **7**, 55 (2005).

[23] J.Y. Fan, X.L. Wu, and P.K. Chu, Prog. Mater. Sci. **51**, 983 (2006).

[24] J. Botsoa, J.M. Bluet, V. Lysenko, O. Marty, D. Barbier, and G. Guillot, J. Appl. Phys. **102**, 083526 (2007).

[25] J. Botsoa, V. Lysenko, A. Géloën, O. Marty, J.M. Bluet, and G. Guillot, Appl. Phys. Lett. **92**, 173902 (2008).

[26] X. Gao, L. Yang, J. A. Petros, F.F. Marshall, J.W. Simons, and S. Nie, Curr. Opin. Biotechnol. **16**, 63 (2005).

[27] D. Beke, Z. Szekrényes, I. Balogh, Z. Czigány, K. Kamarás, and A. Gali, J. Mater. Res. **28**, 44 (2012).

[28] R.E. Bailey and S. Nie, J. Am. Chem. Soc. **125**, 7100 (2003).

[29] N. Sozer and J.L. Kokini, Food Res. Int. **57**, 142 (2014).

[30] J. Will, A. Hoppe, F. A. Müller, C.T. Raya, J.M. Fernández, and P. Greil, Acta Biomater. **6**, 4488 (2010).

[31] C. Torres-Raya, D. Hernandez-Maldonado, J. Ramirez-Rico, C. Garcia-Gañan, A.R. de Arellano-Lopez, and J. Martinez-Fernandez, J. Mater. Res. **23**, 3247 (2011).

[32] J.Y. Fan, X.L. Wu, H.X. Li, H.W. Liu, G.G. Siu, and P.K. Chu, Appl. Phys. Lett. **88**, 041909 (2006).

[33] J. Fan, H. Li, J. Jiang, L.K.Y. So, Y.W. Lam, and P.K. Chu, Small **4**, 1058 (2008).

[34] D. Beke, Z. Szekrényes, I. Balogh, M. Veres, E. Fazakas, L.K. Varga, K. Kamarás, Z. Czigány, and A. Gali, Appl. Phys. Lett. **99**, 213108 (2011).

[35] G.W. Meng, Z. Cui, L.D. Zhang, and F. Phillipp, J. Cryst. Growth **209**, 801 (2000).

[36] M. Dehghanzadeh, A. Ataie, and S. Heshmati-Manesh, Int. J. Mod. Phys. Conf. Ser. **05**, 263 (2012).

[37] M. Dasog, L.F. Smith, T.K. Purkait, and J.G.C. Veinot, Chem. Commun. (Camb). **49**, 7004 (2013).

[38] J. Hu, Q. Lu, K. Tang, and B. Deng, J. Phys. Chem. B **104**, 5251 (2000).

[39] J. Zhu, Z. Liu, X.L. Wu, L.L. Xu, W.C. Zhang, and P.K. Chu, Nanotechnology **18**, 365603 (2007).

[40] J. Fan, H. Li, J. Wang, and M. Xiao, Appl. Phys. Lett. **101**, 131906 (2012).

[41] Y. Kamlag, A. Goossens, I. Colbeck, and J. Schoonman, Chem. Vap. Depos. **9**, 125 (2003).

[42] F. Huisken, B. Kohn, and R. Alexandrescu, J. Nanoparticle Res. **1**, 293 (1999).

[43] L. Mangolini, E. Thimsen, and U. Kortshagen, Nano Lett. **5**, 655 (2005).

[44] U. Kortshagen, J. Phys. D. Appl. Phys. **42**, 113001 (22 pp) (2009).

[45] R.P. Chaukulkar, K. de Peuter, P. Stradins, S. Pylypenko, J. P. Bell, Y. Yang, and S. Agarwal, In Press (2014).

[46] D. Basa and F. Smith, Thin Solid Films **192**, 121 (1990).

[47] W.K. Choi, T.Y. Ong, L.S. Tan, F.C. Loh, and K.L. Tan, J. Appl. Phys. **83**, 4968 (1998).

[48] D. McKenzie, J. Phys. D. Appl. Phys. **18**, 1935 (1985).

[49] W. Spitzer, D. Kleinman, and C. Frosch, Phys. Rev. **113**, 133 (1959).

[50] P. Couderc and Y. Catherine, Thin Solid Films **146**, 93 (1987).

[51] A. Grill and V. Patel, Appl. Phys. Lett. **60**, 2089 (1992).

[52] C. Huang, W. Widdra, X.S. Wang, and W.H. Weinberg, J. Vac. Sci. Technol. A **11**, 2250 (1993).

[53] G. Socrates, *Infrared and Raman Characteristic Group Frequencies* (John Wiley & Sons Ltd., West Sussex, England, 2001).

[54] S.P. Louh, C.H. Wong, and M.H. Hon, Thin Solid Films **498**, 235 (2006).

[55] B.N. Jariwala, C. V. Ciobanu, and S. Agarwal, J. Appl. Phys. **106**, 073305 (2009).

[56] B. Cullity and S. Stock, *Elements of X-Ray Diffraction* (Prentice-Hall Inc. New Jersey, 2001).

[57] J.I. Langford and A.J.C. Wilson, J. Appl. Crystallogr. **11**, 102 (1978).

[58] D. Briggs and P. Seah, *Practical Surface Analysis: Auger and X-Ray Photoelectron Spectroscopy* (John Wiley and Sons, Chichester, 1990).

[59] M.P. Delplancke, J. Vac. Sci. Technol. A **9**, 450 (1991).

[60] L. Muehlhoff, W.J. Choyke, M.J. Bozack, and J.T. Yates, J. Appl. Phys. **60**, 2842 (1986).

[61] B.N. Jariwala, N.J. Kramer, M.C. Petcu, D.C. Bobela, M.C.M. van de Sanden, P. Stradins, C. V Ciobanu, and S. Agarwal, J. Phys. Chem. C **115**, 20375 (2011).

[62] Y. Li and T. Ishigaki, J. Ceram. Soc. Japan **723**, 717 (2007).

[63] L. Latu-Romain, M. Ollivier, A. Mantoux, G. Auvert, O. Chaix-Pluchery, E. Sarigiannidou, E. Bano, B. Pelissier, C. Roukoss, H. Roussel, F. Dhalluin, B. Salem, N. Jegenyes, G. Ferro, D. Chaussende, and T. Baron, J. Nanoparticle Res. **13**, 5425 (2011).

[64] L. Tsakalakos and J. Fronheiser, Mater. Res. Soc. Symp. Proc. **963**, Q11 (2006).

[65] N.J. Kramer, R.J. Anthony, M. Mamunuru, E.S. Aydil, and U.R. Kortshagen, J. Phys. D. Appl. Phys. **47**, 075202 (8 pp) (2014).

[66] T. Lopez and L. Mangolini, Nanoscale **6**, 1286 (2013).

CHAPTER 7

CONCLUSIONS AND FUTURE WORK

This chapter summarizes the key conclusions drawn from the work performed in this dissertation. As described in the previous chapters, we have used metal-oxide thin films, and non-thermal plasma treatments, to engineer the surfaces of Group IV materials. We have used *in situ* ATR-FTIR spectroscopy combined with various *ex situ* characterization techniques to gain a comprehensive understanding of the process as well as the interface. Based on the results obtained in this work we also propose some future pathways for investigations which will enhance our understanding gained from this work.

7.1 Chemical passivation of *c*-Si by Al_2O_3

We have studied the mechanism of chemical passivation of *c*-Si by Al_2O_3 using ATR-FTIR spectroscopy combined with minority carrier lifetime measurements. Our results indicate, H is preserved at the interface after deposition of Al_2O_3 on H-terminated Si. The H is then lost during the thermal annealing via thermal desorption and restructuring. Restructuring at the interface also leads to the formation of an interfacial SiO_x layer. The use of dueterated precursors allows us to study the role of H in the mechanism of chemical passivation. Within the sensitivity of our setup we do not observe any migration of H from Al_2O_3 to the *c*-Si interface during the annealing step. This leads us to conclude that the restructuring at the interface is what leads to the reduction of the interface defect density upon thermal annealing. We have also observed better passivation quality upon annealing under oxidizing environments which further

emphasizes the importance of the interfacial SiO_x layer. The use of Si IRCs for these studies would greatly enhance our understanding of the effect of the annealing environments on the chemical composition of the interface and should be considered for future studies.

7.2 ALD of TiO_2 using metal-alkoxide as the oxygen source

We have demonstrated the ALD of TiO_2 using a combination of a metal halide and metal alkoxide as precursors without the use of an oxygen source such as H_2O, O_3, or an O_2 plasma. The growth per cycle of 0.7 Å was higher than the values reported for other thermal ALD processes at similar temperatures. This suggests that the process is more suited for high volume processing than other thermal processes. The surface reactions during the ALD process follow the alkyl-transfer mechanism over the temperature range of 150-250 °C. At 250 °C, TTIP starts to decompose thermally on the TiO_2 surface; however, this decomposition process is much slower than the alkyl-transfer reactions and is not expected to affect the self-saturation nature of the ALD process. The surface passivation of *c*-Si by TiO_2 deposited using this process should be considered for future studies. The process can also be used to deposit mixed metal oxides and hence, the use of this process to deposit doped TiO_2 should be considered for future investigations.

7.3 Single-step synthesis of carbon-coated Group IV nanoparticles

We have developed a single-step process to synthesize *a*-C-coated Si NPs < 10 nm in size using a dual-plasma setup. We have demonstrated that the sp^2-to-sp^3 hybridization ratio of the *a*-C coating as well as the thickness of the interfacial 3C-SiC layer can be manipulated through the downstream C_2H_2 plasma rf power, which in turn controls the hydrocarbon radical flux and

plasma-induced heating of the NPs. The 3C-SiC layer has direct implications for the use of these NPs in LIBs. While 3C-SiC conducts Li ions, it does not undergo lithiation. Therefore, this interfacial layer does not contribute to the lithiation capacity of the *a*-C-coated Si NPs thereby reducing the effective charge capacity of LIBs. Therefore, we have extended this technique to synthesize carbide-free *a*-C coated Ge and Sn NPs. We synthesize the *a*-C coated Ge and Sn NPs from chloride precursors which demonstrates the versatility of the process. The process can be used to synthesize various *a*-C coated Group IV NPs using different precursor combinations. The synthesis of Sn NPs suggests this process can potentially be extended to synthesize other low-melting metal NPs. The use of this technique to form shells/coatings other than *a*-C, like oxide or nitride, can be explored.

We have also used this technique to synthesize *a*-C:H coated 3C-SiC NPs. The size of the 3C-SiC NPs, ~4.2 nm, was estimated using XRD and TEM analysis. This size is comparable to the Bohr exciton radius of SiC (2.7 nm), and thus within the size range where quantum confinement effects have been observed in SiC. Therefore, this plasma synthesis technique can be used to synthesize 3C-SiC QDs for potential biomedical applications, such as fluorescent markers. The surface of the 3C-SiC NPs was partially alkenyl terminated, which can also facilitate further surface functionalization for biomedical applications. For future investigations, the effect of the tube pressure on the size of the as-synthesized 3C-SiC NPs should be considered.

APPENDIX A

QUANTITATIVE XRD ANALYSIS

The relative intensity of diffraction peaks in a diffraction pattern of a multicomponent mixture depends on the relative concentrations of the components. Therefore, by comparing the ratio of integrated diffraction intensities for a particular *hkl* plane for each component in an XRD pattern for a binary mixture, the concentration of the two components can be calculated.

The intensity of the diffracted beam for component α in a binary mixture can be expressed as,

$$I_\alpha(hkl) = \left(\frac{I_0 A \lambda^3}{32\pi r}\right)\left[\left(\frac{\mu_0}{4\pi}\right)\frac{e^4}{m^2}\right]\left(\frac{1}{v_\alpha^2}\right)\left[\left|F_\alpha(hkl)\right|^2 p\left(\frac{1+\cos^2 2\theta}{\sin^2\theta\cos\theta}\right)\right]\left(\frac{e^{-2M}}{2\mu_\alpha}\right)V_\alpha \tag{A.1.1}$$

where, $I_\alpha(hkl)$ is the integrated intensity for the (*hkl*) reflection of phase α; $\left(\frac{I_0 A \lambda^3}{32\pi r}\right)\left[\left(\frac{\mu_0}{4\pi}\right)^2\frac{e^4}{m^2}\right]\left(e^{-2M}\right)$ contains the instrumentation parameters and physical constants;

$\left|F(hkl)\right|^2$ is the structure factor calculated from the atomic scattering factor, f; p is the multiplicity factor for reflection (*hkl*); $\frac{1+\cos\ 2\theta}{\sin^2\theta\cos\theta}$ is the Lorentz-polarization factor, L_α, calculated from the 2θ position of the diffraction peak; μ_α is the linear absorption coefficient for component α; V_α is the volume fraction of the component α, and v_α is the volume of unit cell for component α.

Thus, based on Eq. A.1.1, for a binary mixture containing Si and SiC, the ratio of the integrated intensities for the (111) reflection for the two phases is given by,

$$\frac{I_{Si}(111)}{I_{SiC}(111)} = \left(\frac{|F_{Si}(111)|^2}{|F_{SiC}(111)|^2}\right)\left(\frac{L_{Si}}{L_{SiC}}\right)\frac{\mu_{SiC} v_{SiC}^2 V_{Si}}{\mu_{Si} v_{Si}^2 V_{SiC}}. \quad \text{(A.1.2)}$$

Since $V_{SiC} = 1 - V_{Si}$, the volume fractions of the two components can be calculated from Eq. A.1.2. The linear absorption coefficient for SiC, μ_{SiC}, is calculated using the expression,

$$\left(\frac{\mu_{SiC}}{\rho_{SiC}}\right) = w_{Si}\left(\frac{\mu_{Si}}{\rho_{Si}}\right) + w_c\left(\frac{\mu_C}{\rho_C}\right),$$

(A.1.3)

where, w_{Si} and w_C are the weight fractions of Si and C in SiC, and ρ is the density.

Calculation of *c*-Si Core Size and 3C-SiC Coating Thickness: The initial size of the H-terminated *c*-Si NP is denoted by d_1, the final size of the *c*-Si core of the carbon-coated NP is denoted by d_2, and the thickness of the SiC layer is denoted by t. Therefore, the volume fraction of the c-Si core, VSi, is given by

$$\frac{d_2^3}{(d_2 + 2t)^3} = V_{Si}. \quad \text{(A.1.4)}$$

Initial moles of Si in the H-terminated c-Si NP, N_{Si}^i, is given by

$$N_{Si}^i = \frac{4\pi d_1^3 \rho_{Si}}{24 m_{Si}}, \quad \text{(A.1.5)}$$

where, m_{Si} is the atomic weight of Si. The final moles of Si, N_{Si}^{f}, which are conserved in the core-shell structure are given by,

$$N_{Si}^{f} = \frac{4\pi d_2^3 \rho_{Si}}{24 m_{Si}} + \frac{4\pi\left[(d_2 + 2t)^3 - d_2^3\right]\rho_{SiC}}{24 m_{SiC}}, \qquad \text{(A.1.6)}$$

where, m_{SiC} is the molecular weight of SiC. Given that the moles of Si are conserved, we can write,

$$\frac{d_1^3 \rho_{Si}}{m_{Si}} = \frac{d_2^3 \rho_{Si}}{m_{Si}} + \frac{\left[(d_2 + 2t)^3 - d_2^3\right]\rho_{SiC}}{m_{SiC}}. \qquad \text{(A.1.7)}$$

Thus, using equations A.1.4 and A.1.7, combined with the values of the various parameters reported in literature, the final diameter of the *c*-Si NP, d_2, and the thickness of the 3C-SiC layer, t, were calculated.

APPENDIX B

LOW TEMPERATURE HYDROGEN PLASMA-ASSISTED ATOMIC LAYER DEPOSITION OF COPPER STUDIED USING *IN SITU* INFRARED REFLECTION ABSORPTION SPECTROSCOPY

Based on a paper published in The Journal of Vacuum Science & Technology A

Rohan P. Chaukulkar[1] Nick F. W. Thissen,[2] Vikrant R. Rai,[1] and Sumit Agarwal[1]

[1]Department of Chemical and Biological Engineering, Colorado School of Mines, Golden, Colorado, 80401

[2]Department of Applied Physics, Eindhoven University of Technology, 5600 MB Eindhoven, The Netherlands

Abstract

Atomic layer deposition (ALD) is an ideal technique to deposit ultrathin, conformal, and continuous metal thin films. However, compared to the ALD of binary materials such as metal oxides and metal nitrides, the surface reaction mechanisms during metal ALD are not well understood. In this study, we have designed and implemented an *in situ* reflection-absorption infrared spectroscopy (IRAS) setup to study the surface reactions during the ALD of Cu on Al_2O_3 using Cu hexafluoroacetylacetonate [Cu(hfac)$_2$] and a remote H_2 plasma. Our infrared data show that complete ligand-exchange reactions occur at a substrate temperature of 80 °C in the absence of surface hydroxyl groups. Based on our infrared data and previous studies, we propose that Cu(hfac)$_2$ dissociatively chemisorbs on the Al_2O_3 surface, where the Al-O-Al bridge acts as

the surface reactive site, leading to surface O-Cu-hfac and O-Al-hfac species. Surface saturation during the $Cu(hfac)_2$ half-cycle occurs through blocking of the available chemisorption sites. In the next half-reaction cycle, H radicals from an H_2 plasma completely remove these surface hfac ligands. Through this study, we have demonstrated the capability of *in situ* IRAS as a tool to study surface reactions during ALD of metals. While transmission and internal reflection infrared spectroscopy are limited to the first few ALD cycles, IRAS can be used to probe all stages of metal ALD starting from initial nucleation to the formation of a continuous film.

B.1 Introduction

Copper is the preferred interconnect material in integrated circuits because of its low bulk resistivity, and high resistance to electromigration and stress migration.[1–7] Additionally, Cu also has a low temperature coefficient of resistance and good thermal stability.[2] Current processes to fabricate interconnects include electroplating Cu, which typically requires a thin continuous seed layer.[3–6,8–10] A Cu seed layer not only provides a conducting substrate for the electroplating process, but also improves adhesion and nucleation of the electroplated Cu.[3,6,8,10] A discontinuous or non-conformal seed layer can lead to the formation of voids during the electroplating process, which hampers the performance of the interconnects by increasing the resistance.[3,4,6,8] Physical vapor deposition (PVD) processes have conventionally been used to deposit such Cu seeds layers.[4,8–10] With the continuous scaling of microelectronic devices, these seed layers have to be conformally deposited over high-aspect-ratio structures, which is increasingly difficult with PVD.[2,4,6,8–10]

Atomic layer deposition (ALD) is a thin-film deposition technique with the ability to deposit excellent quality pin-hole-free films with high conformality on high-aspect-ratio

structures with digital control over the film thickness.[11–13] ALD has been used to deposit a variety of materials, including metals.[10,14–19] The ALD process involves sequential, self-limiting

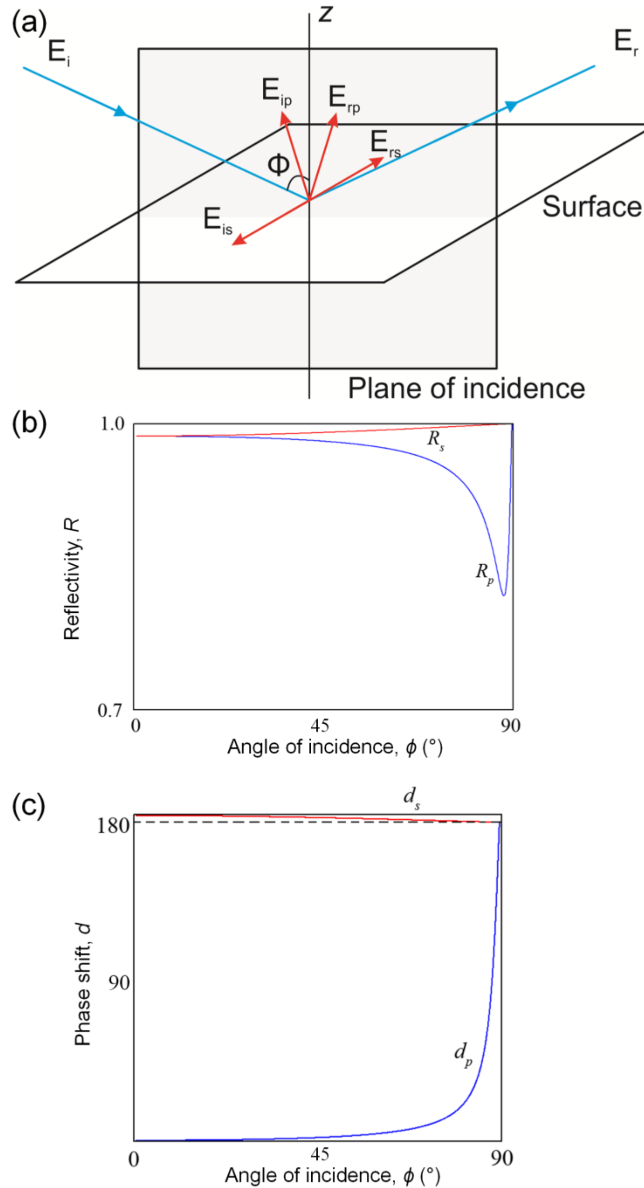

Figure B.1. (a) Schematic showing the *s* and *p* components of the electric field associated with the incident and reflected light. **(b)** A plot of the reflectance, R, as a function of the angle of incidence, ϕ, using the expression in Eqns. 3 and 4 with n = 3 and k = 30. The plot in (b) shows that $R_s \approx 1$ for all angles of incidence, while R_p shows a minimum for near-grazing values of ϕ.

(c) The graph shows phase shift, *d*, upon reflection for the *s* and *p* polarized light plotted as a function of the angle of incidence, ϕ, using Eqns. 5 and 6. The *s* component of the electric field undergoes an almost constant phase shift of ~180° resulting in a negligible electric field parallel to the surface for all angles of incidence.

surface reactions during both half-reaction cycles, which play a crucial role in determining the properties of the deposited film. Therefore, it is essential to study these surface reactions to better control film growth during ALD, and to develop novel ALD chemistries.[13] Various techniques including transmission Fourier transform infrared (FTIR) spectroscopy,[20–23] attenuated total reflection (ATR) FTIR spectroscopy,[13,24–28] X-ray photoelectron spectroscopy,[28,29] spectroscopic ellipsometry,[30,31] quartz crystal microbalance,[32,33] and quadrupole mass spectrometry[33,34] have been used to study these surface reactions. Various reports in the literature,[20–23] including previous work by our group[24–28] has shown surface infrared spectroscopy is particularly valuable for obtaining insight into the surface reaction mechanisms during ALD. However, the use of transmission and internal reflection infrared spectroscopy to study the ALD of metals is restricted to the nucleation phase[23] due to free-electron absorption in metals, which makes the deposition substrate opaque in the infrared radiation even for ultrathin metal films. Herein, we report on the surface reactions during H_2 plasma assisted ALD of Cu using copper hexafluroacetylacetonate hydrate [$Cu(hfac)_2 \cdot xH_2O$] (IUPAC name - 1,1,1,5,5,5-hexafluro-2,4-pentanedione copper) studied using *in situ* infrared reflection-absorption spectroscopy (IRAS). We report on the initial nucleation and growth of Cu on an Al_2O_3 surface, and identify the surface reactive sites for $Cu(hfac)_2$ chemisorption. IRAS has been previously used to study the

ALD of metal oxides[35,36], but to our knowledge there are no reports on the use of *in situ* IRAS to study the ALD of metals.

B.2. Experimental Details

B.2.1 Infrared reflection-absorption spectroscopy

Figure B.1a shows a schematic for the reflection of an infrared beam from a metal surface. The electric field of the infrared radiation incident on metal surfaces interacts with both

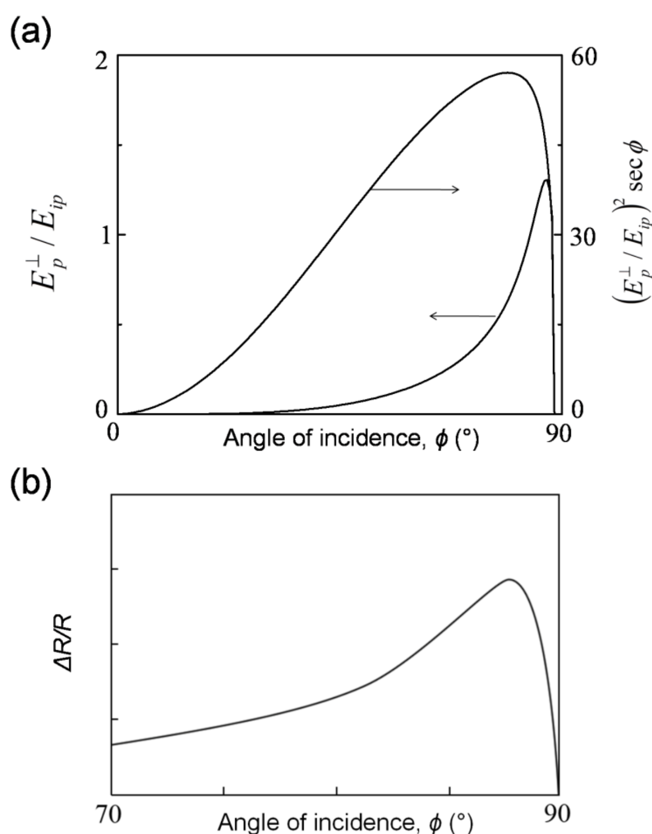

Figure B.2. (a) A plot of the ratio of the perpendicular component of the electric field to the total incident electric field for the *p* component of light ($E_p^{\perp}/E_{ip}$) as a function of the angle of incidence, ϕ. The quantity ($E_p^{\perp}/E_{ip}$)^{2}sec ϕ, which is proportional to the experimentally-observed

infrared absorbance, is also plotted as a function of ϕ. **(b)** Absorbance or change in reflectance, $\Delta R/R$ plotted as a function of the angle of incidence, ϕ, for an Al (n = 6.8, k = 32) film coated with ~10 nm of Al_2O_3 (n = 1.3, k = 0.1).

the dipole of the adsorbed molecule and the free electrons of the metal. However, under most conditions, infrared absorption is dominated by the dielectric behavior of the metal,[37] except at grazing angles of incidence used in IRAS. Below, we briefly describe the principle for IRAS and its implementation in our ALD reactor, which was originally designed for ATR-FTIR spectroscopy.[13] We demonstrate that implementation of IRAS in deposition chambers is not limited by the availability of access ports for grazing incidence. We also address additional important considerations, such as multiple external reflections and the use of a polarizer, to improve the signal-to-noise ratio.

In the reflection geometry in Fig. B.1a, the electric field associated with the incident beam (E_i) has two components: E_{is} is the s component parallel to the reflecting surface, and E_{ip} is the p component parallel to the plane of incidence. Similarly, the electric field associated with the reflected beam (E_r) from the metal surface has two components E_{rs} and E_{rp}, which are parallel to the reflecting surface and the plane of incidence, respectively. This metallic reflecting surface can be described with a two-phase model consisting of vacuum and the metal substrate with a complex index of refraction, $\varepsilon = n + i \cdot k$, where n is the refractive index and k is the extinction coefficient. Using Fresnel's equations, the corresponding reflection coefficients for s and p polarized light can be expressed as [37–39]

$$r_s = \frac{E_{rs}}{E_{is}} = \frac{\cos\phi - (n + i \cdot k)}{\cos\phi + (n + i \cdot k)} \quad \text{(B.1)} \quad \text{and} \quad r_p = \frac{E_{rp}}{E_{ip}} = \frac{1 - (n + i \cdot k)\cos\phi}{1 + (n + i \cdot k)\cos\phi}, \quad \text{(B.2)}$$

respectively, where ϕ is the angle of incidence. The corresponding reflectance for each component, R_s and R_p, are given by

$$R_s = r_s^2 = \frac{(n - \sec\phi)^2 + k^2}{(n + \sec\phi)^2 + k^2} \quad \text{(B.3)} \quad \text{and} \quad R_p = r_p^2 = \frac{(n - \cos\phi)^2 + k^2}{(n + \cos\phi)^2 + k^2}. \quad \text{(B.4)}$$

Finally, the phase shifts, d_s and d_p, upon reflection for the *s* and *p* components are given by

$$d_s = \tan^{-1}\left[\frac{\mathrm{Im}(r_s)}{\mathrm{Re}(r_s)}\right] \quad \text{(B.5)} \quad \text{and} \quad d_p = \tan^{-1}\left[\frac{\mathrm{Im}(r_p)}{\mathrm{Re}(r_p)}\right], \quad \text{(B.6)}$$

respectively.

Figure B.1b shows R_s and R_p as a function of ϕ (Eqns. B.3 and B.4) for $n = 3$ and $k = 30$, which are representative values for a typical metal. The corresponding phase shifts upon reflection, d_s and d_p as a function of ϕ, are plotted in Fig. 1c (Eqns. B.5 and B.6). The resultant electric field at the surface for the *s* component, E_s, remains parallel to the reflecting surface for all ϕ, and is given by

$$E_s = E_{is}[\sin\phi + r_s \sin(\phi + d_s)]. \quad \text{(B.7)}$$

Since $r_s \approx 1$ for all ϕ ranging from 0-90° (see Fig. 1b), with $d_s \approx 180°$ (see Fig. B.1c), $E_s \approx 0$.[37,38] On the other hand, the resultant electric field at the surface for the *p* polarized light, E_p, has two components, which are parallel ($E_p^{\Rightarrow}$) and perpendicular ($E_p^{\perp}$) to the reflecting surface. These resultant electric fields for the *p* component can be expressed as,

$$E_p^{\Rightarrow} = E_{ip} \cos\phi \cdot [\sin\phi - r_p \sin(\phi + d_p)] \qquad \text{(B.8)}$$

$$E_p^{\perp} = E_{ip} \sin\phi \cdot [\sin\phi + r_p \sin(\phi + d_p)]. \qquad \text{(B.9)}$$

At low angles of incidence, the parallel component of the resulting *p* polarized electric field, $E_p^{\Rightarrow}$ $\approx$ 0, since $r_p \approx 1$ and $d_p \approx 0$ (see Fig. B.1b, B.1c and Eqn. B.8). On the other hand, the perpendicular components of the resulting *p*-polarized electric field, $E_p^{\perp}$, combine constructively. The ratio $E_p^{\perp}/E_{ip}$ increases with the angle of incidence as the sine terms in Eq. 9 approach unity (see Fig. B.2a). This has two consequences: 1) only the surface vibrational modes with a component of the oscillating dipole oriented perpendicular to the metal surface are infrared-active,[37,39–42] and 2) the total infrared absorption is maximum at near-grazing incidence as $E_p^{\perp}$ is maximized (see Fig. B.2a), and the number of surface adsorbates interacting with the electric field, proportional to secϕ, are also maximized (see Fig. B.2a).[43]

To investigate the adsorption of species on non-metallic surfaces, the reflecting metal surface can be coated with a thin dielectric layer such as a metal oxide. However, the infrared light now interacts with the dielectric function of the oxide layer in addition to that of the metal surface. Thus, the optical system is described by a three-component model consisting of vacuum, the oxide layer, and the metal surface. The absorbance, *A*, due to the additional oxide layer is calculated based on the reflectance as,[37,38,44]

$$A = \frac{R^0 - R}{R^0} = \frac{\Delta R}{R^0}\ . \qquad \text{(B.10)}$$

where R^0 and R are the reflectances without and with the oxide layer, respectively. McIntyre and Aspnes[38] analyzed this optical model by assuming the three components to be isotropic with dielectric functions defined as, $\varepsilon_j = n_j + i \cdot k_j$ (j = 1, 2 and 3 for vacuum, the oxide layer, and the metal surface respectively; $\varepsilon_1 = 1$ for vacuum). For infrared wavelengths λ = 2.5 – 20 μm, and film thicknesses d < 100 nm, $d/\lambda \ll 1$, the absorbance for the s and p components is given by,

$$\frac{\Delta R_s}{R_s} = \frac{8\pi d \cos\phi}{\lambda} \mathrm{Im}\left(\frac{\varepsilon_2 - \varepsilon_3}{1 - \varepsilon_3} \right) \tag{B.11}$$

and

$$\frac{\Delta R_p}{R_p} = \frac{8\pi d \cos\phi}{\lambda} \mathrm{Im}\left\{ \left(\frac{\varepsilon_2 - \varepsilon_3}{1 - \varepsilon_3} \right) \left(\frac{1 - \left(\frac{1}{\varepsilon_2 \varepsilon_3} \right)(\varepsilon_2 + \varepsilon_3)\sin^2\phi}{1 - \left(\frac{1}{\varepsilon_3} \right)(1 + \varepsilon_3)\sin^2\phi} \right) \right\}, \tag{B.12}$$

respectively.

Since for typical metals and metal oxides, such as Al and Al_2O_3, $\varepsilon_3 \gg \varepsilon_2$, the change in reflectance for the s component is negligible. Figure 2b shows the absorbance due to a thin dielectric layer (30 nm) for the p component as a function of ϕ, which is maximum at a grazing angle of incidence. Thus, this demonstrates that even in the presence of thin adsorbate layers, absorbance is maximum at high angles of incidence (≈85°),[37–39] and only the oscillating dipoles with a component perpendicular to the reflecting surface are infrared-active.

Greenler[41] studied the possibility of using multiple reflections for enhancing the signal-to-noise ratio in IRAS. However, loss in signal intensity after each reflection due to absorption

by the metal limits the maximum number of reflections the infrared light can undergo. As a result, it was shown that for most metals a single reflection is sufficient, and in most cases optimum, to obtain IRAS data.

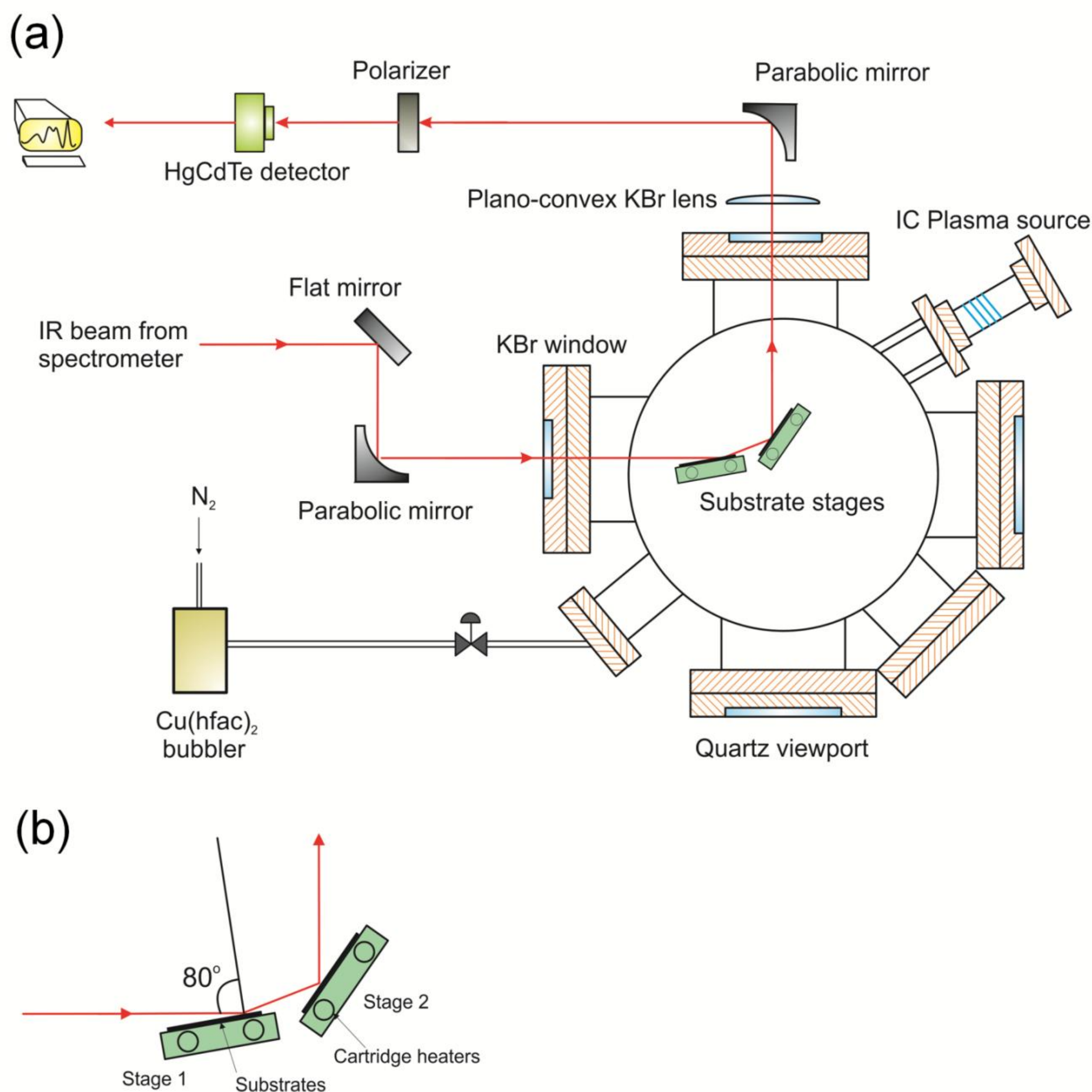

Figure B.3. (a) Schematic top view of the reactor equipped with the *in situ* IRAS setup. The chamber is also equipped with a remote inductively coupled plasma source. The infrared beam from the spectrometer is focused onto the first substrate stage at grazing incidence. The reflected beam from the first mirror is then collected and focused onto a MCT-A detector after reflection

from a second redirecting mirror. (b) A zoomed-in view of the schematic showing the substrate stage and the diverting mirror. Both reflecting surfaces can be heated using the cartridge heaters mounted inside the stages.

Since the *s* component of the electric field does not couple with the oscillating dipole on the surface, a polarizer in the infrared beam path can be used to conduct the experiment with only the *p*-component. Song et al. quantitatively analyzed the effect of a polarizer in IRAS experiments, and showed that eliminating the *s* component of the electric field can enhance the absorbance by a factor of 2-3.[45] The infrared detector noise can be minimized by cooling the detector to cryogenic temperatures. The noise in the experiment is then background limited, which is proportional to the intensity at the detector. The polarizer reduces the intensity by roughly half, which in turn reduces the noise level proportionally resulting in a net enhancement in the signal-to-noise ratio.[46,47]

B.2.2. In situ IRAS setup

The surface analysis vacuum chamber, described previously,[13] is equipped with an *in situ* ATR-FTIR spectroscopy setup,[13,24,26,28] which used a 50 × 10 × 1 mm trapezoidal internal reflection crystal with the short faces beveled at 45°. In this setup, the beam undergoes a 90° change in angle as it is internally reflected through the trapezoid. To conduct IRAS in the same vacuum chamber using the same external optical setup (see Ref. 13), we obtained a total of 90° deflection of the incident beam via two mirrors placed inside the chamber, as shown in Figs. 3a and 3b. The infrared beam from the spectrometer was focused onto the first reflecting mirror at grazing incidence (≈80°) and a second mirror at ≈45°. However, as discussed above (see Fig. B.2b), change in absorbance observed in the infrared spectra are primarily sensitive to absorbates

on the first mirror due to the grazing angle of incidence (see Fig. 3b). The two reflecting mirrors, henceforth referred to as deposition substrates, were clamped onto the large faces of two 38 × 38 × 12 mm identical stainless-steel blocks, which were heated using cartridge heaters and maintained at identical temperatures. Both substrates were prepared using a two-step process: first, a ~15-20 nm layer of Al metal was evaporated onto HF-treated *c*-Si wafers at a rate of ~1 Å/sec. Second, ~30 nm of Al_2O_3 was deposited on these Al-coated Si wafers via plasma-enhanced chemical vapor deposition using trimethyl aluminum and O_2 plasma as precursors.[48]

The IR spectra were recorded as difference spectra, where a fresh reference spectrum was collected before each half-reaction cycle. Thus, an infrared difference spectrum collected after the completion of the purge step following a certain half-reaction cycle, enabled us to directly probe the changes in the surface composition in a given half-reaction cycle. The spectra were recorded with an HgCdTe (MCT-A) detector at 4 cm^{-1} resolution and averaged over 500 scans, unless otherwise stated. A 25-mm-diameter ZnSe wire grid polarizer (Edmund Optics) was placed directly in front of the detector with an orientation that only allowed the *p*-polarized component of the infrared radiation to the detector (see Fig B.3a). It should be noted that experiments conducted without a polarizer produced spectra with absorbance features that were not discernible from the noise.

B.2.3. Cu atomic layer deposition

Copper films were deposited at a substrate temperature of 80 °C using $Cu(hfac)_2$ hydrate (Sigma-Aldrich) and a remote H_2/Ar inductively-coupled plasma. $Cu(hfac)_2$ was used as-

received and maintained at ~130 °C in a stainless steel container. Precursor flow, without any carrier gas, was controlled with a metering needle valve (Swagelok SS-4L). H_2 and Ar were each delivered at 50 standard cm^3/min using mass flow controllers, and the same gas mixture was also used to purge the chamber in between each half-reaction cycle. $Cu(hfac)_2$ was pulsed for 10 s, followed by a 30-s purge. After the purge step, the H_2/Ar-plasma, operated at a radio-frequency power of 100 W at 13.56 MHz, was turned on for 30 s followed by a 30-s purge. Isotope

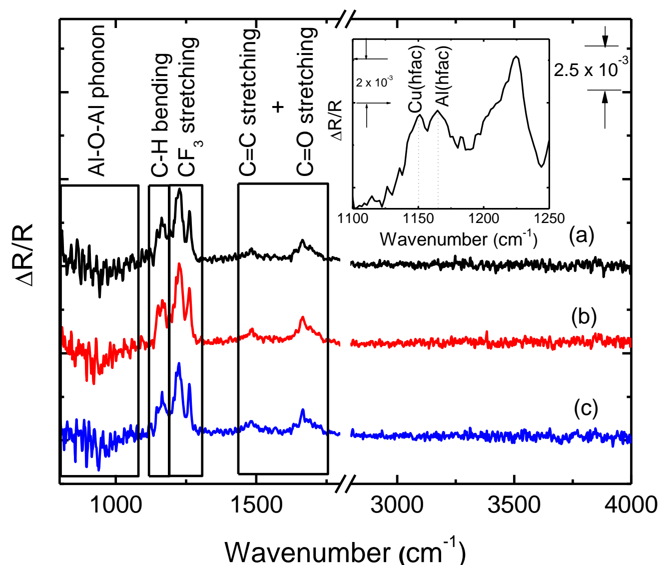

Figure B.4. Infrared difference spectra showing the absorbance change for the $Cu(hfac)_2$ half-reaction cycle collected (a) after a 10-s precursor exposure, (b) after an additional 10-s precursor exposure and (c) after a 30-s purge-step using a gas mixture of Ar and H_2. The identical absorbance in the three spectra suggests self-saturating chemisorption of $Cu(hfac)_2$ onto the substrate, and the lack of reactivity between surface-chemisorbed $Cu(hfac)_2$ and molecular H_2 at a substrate temperature of 80 °C. The inset in Fig. 4 shows the CH bending region in detail.

exchange experiments using D_2 plasma were carried out under almost identical conditions. The

chamber was maintained at a base pressure of ~5 mTorr, and the pressure rose to ~30 mTorr during the Cu(hfac)$_2$ pulse and to ~200 mTorr during H_2/Ar the purge and plasma cycles.

B.3. Results and Discussion

Figure B.4 shows infrared difference spectra collected after Cu(hfac)$_2$ half-reaction cycles at a substrate temperature of 80 °C with respect to a background spectrum collected prior to Cu(hfac)$_2$ exposure. These spectra were recorded after two complete Cu ALD cycles on the Al_2O_3 surface and, thus, correspond to the very initial nucleation stage in the ALD process. Specifically, in Fig. B.4 (spectrum a), we observed an increase in the 1130-1180, 1200-1300, 1500-1700 cm^{-1} regions, which have been assigned to the CH bending, CF_3 stretching, and C=C and C=O stretching modes, respectively, in surface chemisorbed hfac ligands.[49–55] Previously, chemisorption of Cu(hfac)$_2$ has been reported to proceed on a variety of metal surfaces via the fragmentation of the parent molecule to form surface-bound -Cu(hfac) and -hfac species.[50] Further analysis of the infrared spectrum in the 1130-1180 cm^{-1} region (see inset in Fig. B.4) reveals two distinct modes at ~1151 and ~1165 cm^{-1}. Based on the vibrational frequencies reported by Morris et al. for various metal hfac molecules, we have been assigned the modes at ~1151 and ~1165 cm^{-1} to CH bending in Cu(hfac) and Al(hfac),[51,54,55] respectively, which is consistent with the dissociative chemisorption of Cu(hfac)$_2$. Goldstein and George studied the chemisorption of Pd(hfac)$_2$ on hydroxylated Al_2O_3, and identified two vibrational modes at ~ 1155 and 1169 cm^{-1}, which were assigned to CH bending in surface-chemisorbed Pd(hfac)and Al(hfac), respectively. In addition, they observed two modes at ~1607 and ~1659 cm^{-1}, which were assigned to C=O stretching vibrations in Pd(hfac)and Al(hfac), respectively. On the other hand, in our data shown in Fig. B.4, a single peak was observed for the C=O stretching mode at

~1650 cm^{-1} for both Cu(hfac) and Al(hfac) species, which is consistent with previously reported vibrational frequencies for $Cu(hfac)_2$ and $Al(hfac)_3$.[55] We also observed a decrease in absorbance

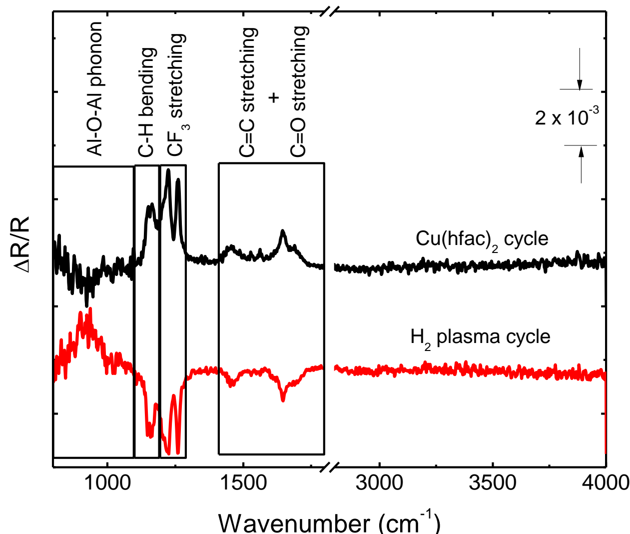

Figure B.5. Infrared difference spectra showing the change in absorbance due to different surface species in the two half-reaction cycles during the ALD of Cu using $Cu(hfac)_2$ and a H_2 plasma. The almost identical change in absorbance during the two half-reaction cycles suggests a one-to-one ligand exchange typical of an ALD process.

in the ~920 cm^{-1} region, which has been assigned to the longitudinal optical phonon mode for γ-Al_2O_3.[26,56] A previous study by Goldstein and George reported the formation of surface Al(hfac) upon exposure of a hydroxylated Al_2O_3 surface to Hhfac molecules with H_2O as the reaction product.[51] This may suggest that the surface –OH species are required for $Cu(hfac)_2$ chemisorption on Al_2O_3. However, in our experiments, the initial Al_2O_3 film deposited by plasma enhanced chemical vapor deposition had minimal surface –OH groups,[48,57] due to which chemisorption on the Al-O-Al bridges was the dominant mechanism for precursor chemisorption. The decrease in absorbance in the ~920 cm^{-1} region in Fig. B.4 may be due to the

breaking of the Al-O bond upon dissociative chemisorption of $Cu(hfac)_2$ or the chemical

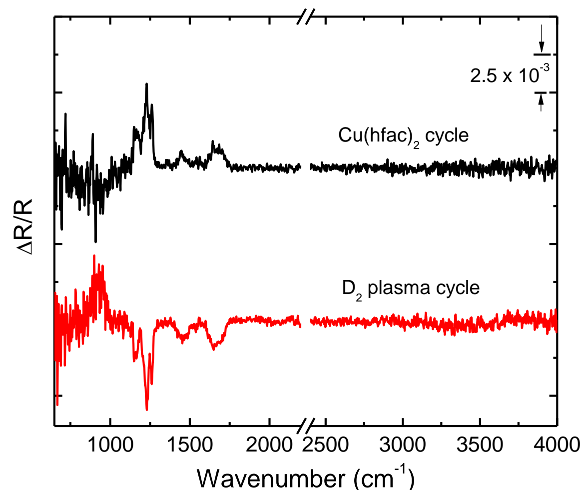

Figure B.6. Infrared difference spectra showing the absorbance change for the $Cu(hfac)_2$ (black) and the D_2 plasma (red) half-reaction cycles at a substrate temperature of 80 °C.

interaction of the Cu(hfac) and hfac species with surface O and Al atoms, respectively, without the cleavage of the Al-O bond.[23,58] The dielectric screening due to the interaction of these ligands with the Al_2O_3 surface can change the oscillator strength of the Al-O bond, which can manifest as an observed decrease in absorbance for the phonon mode.[23,36,58] Regardless, our infrared spectra show surface –OH groups are not required for the chemisorption of $Cu(hfac)_2$ on Al_2O_3 surfaces at 80 °C. This observation is consistent with the infrared "spectrum a" in Fig. 4, where we did not observe a decrease in absorbance in the –OH stretching region (3200-3800 cm^{-1}) during the $Cu(hfac)_2$ cycle.[26]

To confirm that the spectral features observed in the topmost spectrum "a" in Fig. B.4 were indeed due to chemisorption of $Cu(hfac)_2$ on the Al_2O_3 surface (and not physisorption), we exposed the surface to additional 10-s pulse of $Cu(hfac)_2$. First, a difference spectrum (Fig. B.4,

spectrum b) was collected with respect to the reference spectrum recorded prior to the first $Cu(hfac)_2$ pulse. Next, the chamber was purged for 30 s, after which another difference spectrum was recorded using the same original reference spectrum. Since spectra "b" and "c" in Fig. B.4 show identical change in absorbance compared to spectrum "a", we conclude that $Cu(hfac)_2$ chemisorption on Al_2O_3 is self-saturating and produces stable surface species. A mixture of H_2 and Ar was used to purge the chamber (see Experimental section), which further indicates that $Cu(hfac)_2$ does not react with molecular H_2 at a substrate temperature of 80 °C over the time scale of an ALD half-reaction cycle.

Figure B.5 shows infrared spectra, averaged over 2500 scans, for a complete Cu ALD cycle carried out after three complete ALD cycles on the plasma-deposited Al_2O_3 surface. In the H_2 plasma half-reaction cycle, following the $Cu(hfac)_2$ half-reaction cycle, we observe a decrease in absorbance in the spectral regions assigned above to surface-chemisorbed -Cu(hfac) and -Al(hfac). Since the change in absorbance in the two half-reaction cycles was almost identical, the spectra in Fig. B.5 indicate complete removal of the surface-chemisorbed hfac ligands by the H_2 plasma. Goldstein and George have reported that during Pd ALD on Al_2O_3 (~200 °C) using $Pd(hfac)_2$ and formalin, surface -Al(hfac) species formed during the $Pd(hfac)_2$ cycle could not be completely removed during the formalin cycle, which led to surface poisoning via site blocking. On the other hand, our infrared spectra show that H radicals generated in a H_2 are more efficient in removing surface -Al(hfac) species at significantly lower temperatures (80 °C).[51] Based on this result, we speculate that a H_2 plasma half-reaction cycle would also be effective during ALD of other metals using β-diketonate precursors, where site poisoning may prevent film nucleation.

While the chemisorption mechanism for $Cu(hfac)_2$ can be established based on our infrared spectra, the question remains how these surface sites are regenerated during the initial

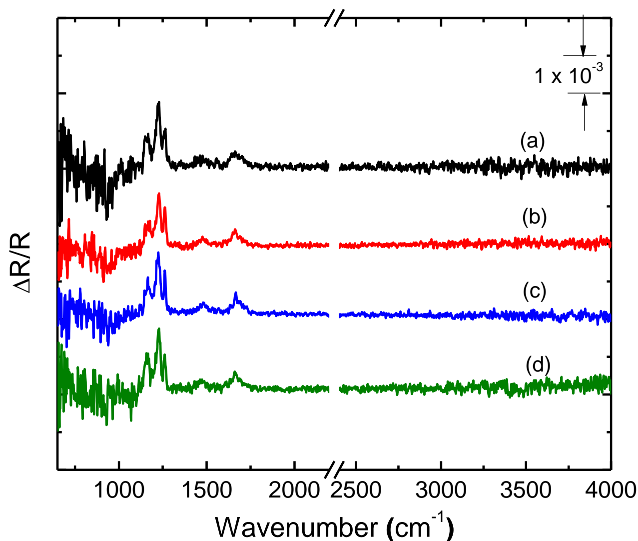

Figure B.7. Infrared difference spectra showing the absorbance change for $Cu(hfac)_2$ half-reaction cycles collected following 80 complete ALD cycles. The spectra (a), (b), (c) and (d) are for the 81st, 82nd, 83rd, and 84th $Cu(hfac)_2$ half-reaction cycle, respectively. Similar absorbance in all the spectra indicates that IRAS can be used to study the surface reactions during ALD of metals well beyond the initial nucleation stage. The corresponding spectra for the H_2-plasma half-reaction cycle show a one-to-one ligand exchange, and are not shown here for clarity.

growth period. In Fig. B.5, for the H_2-plasma half reaction cycle, an increase in absorbance in the ~920 cm^{-1} region, assigned to the Al-O-Al phonon mode, suggests reformation of Al-O-Al bonds upon removal of the surface ligands or an increase in the oscillator strength of the Al-O bond during the H_2 plasma cycle. This effect, coupled with the agglomeration of Cu on the surface following the H_2 plasma half-reaction cycle,[23] restores the surface reactive sites for $Cu(hfac)_2$ chemisorption, restores the surface reactive sites for $Cu(hfac)_2$ chemisorption. This observation

of Al-O-Al bond regeneration can be explained based on previous studies on adsorption of Cu adatoms on the Al_2O_3 surface. Specifically, it is known that Cu adsorption of Al_2O_3 depends on the presence of surface –OH species.[59–62] In the absence of –OH groups, Cu is bound very weakly to Al_2O_3 in the Cu(0) oxidation state.[60,62] On the other hand, in the presence of -OH groups, at low coverages, Cu adsorbs on to surface -OH sites in the Cu(I) oxidation state by replacing H atoms in -OH groups.[60,62] In this latter case, further growth results in the Cu(0) oxidation state as the Cu atoms bind to each other to form three-dimensional islands.[60,62] Thus, an increase in the Al-O-Al phonon band in our infrared spectra during the H_2-plasma half-reaction cycle (Fig. B.5) suggests that Cu atoms on the surface are in the weakly adsorbed Cu(0) oxidation state even prior to island growth. This is consistent with the fact that there is no change in absorbance in the –OH stretching region (Fig. B.5). We have also considered an alternative explanation for the regeneration of Al-O-Al bonds during the H_2/Ar plasma cycle due to etching of Cu. However, Cu etching is reported to be ion-assisted,[63] which is highly unlikely due to the remote plasma source used in this study.

We have also considered the possibility that there may be multiple reactive sites on the surface for $Cu(hfac)_2$ chemisorption. For example, it is possible to form surface CuH bonds during the H_2-plasma half-reaction cycle. $Cu(hfac)_2$ could then chemisorb onto these sites by forming surface Cu-Cu-hfac and gas-phase Hhfac, which would be purged. The stretching mode for CuH species is reported in the 1700-2300 cm^{-1} region.[23,64,65] The weak absorbance due to CuH species may be masked by the strong decrease in absorbance due to removal of C=O species during the H_2 plasma cycle. To further examine the possibility of formation of surface copper hydrides and their role in the ALD process, we conducted an isotope exchange experiment where we replaced H_2 with D_2 under otherwise identical conditions. Due to the

difference in the reduced mass for the oscillators, the stretching vibration for CuD is expected to be downshifted with respect to CuH by approximately a factor of $\sqrt{2}$. However, the infrared spectra recorded during both half-reaction cycles for ALD with H_2 are identical to the spectra for ALD with D_2 indicating that it is unlikely that the CuH and CuD species play a significant role in the initial ALD process. Another possibility for the lack of distinct infrared absorption features corresponding to CuH or CuD vibrations is the formation of H or D bridges due to the bonding of the H or D atoms to several Cu atoms. The bridge configuration weakens the absorption band intensity of the CuH/CuD mode, which may lie below the detection limit of our setup.[23,65]

Finally, in Fig. B.7, we demonstrate that IRAS may be used to study surface reactions during metal ALD beyond the very initial nucleation stage. As discussed earlier, transmission- and ATR-FTIR spectroscopy techniques are not suitable beyond the first few ALD cycles due to free-electron absorption in metals. Figure B.7 shows infrared difference spectra collected after the 81st, 82nd, 83rd and 84th $Cu(hfac)_2$ half-reaction cycles. The similar change in absorbance in these spectra compared to those in Fig. B.5 suggests that there is no change in the detection sensitivity even after 80 ALD cycles. This clearly demonstrates the advantage of IRAS over other surface infrared spectroscopy techniques to study metal ALD, where the signal-to-noise ratio starts to decrease after the first few ALD cycles.[23]

B.4 Conclusions

Using *in situ* IRAS, we have studied the surface reaction mechanism during the ALD of Cu on Al_2O_3 with $Cu(hfac)_2$ and H_2 plasma as precursors. In the absence of surface –OH groups, at a substrate temperature of 80 °C, $Cu(hfac)_2$ chemisorption on Al_2O_3 occurred on the Al-O-Al bridge to form Cu(hfac) and Al(hfac) species. The surface-chemisorbed Cu(hfac) species were

reduced to metallic Cu in the subsequent H_2 plasma half-reaction cycle accompanied by the reformation of the Al-O-Al bonds.

ACKNOWLEDGMENTS

We gratefully acknowledge support from the NSF CAREER program (Grant No. CBET-0846923). NFWT acknowledges support from the Eindhoven University of Technology.

References

[1] R. Rosenberg, D.C. Edelstein, C.-K. Hu, and K.P. Rodbell, Annu. Rev. Mater. Sci. **30**, 229 (2000).

[2] B.H. Lee, J.K. Hwang, J.W. Nam, S.U. Lee, J.T. Kim, S.-M. Koo, A. Baunemann, R.A. Fischer, and M.M. Sung, Angew. Chem. Int. Ed. Engl. **48**, 4536 (2009).

[3] L. Wu and E. Eisenbraun, Electrochem. Solid-State Lett. **11**, H107 (2008).

[4] D.-Y. Moon, D.-S. Han, S.-Y. Shin, J.-W. Park, B.M. Kim, and J.H. Kim, Thin Solid Films **519**, 3636 (2011).

[5] Z. Li, A. Rahtu, and R.G. Gordon, J. Electrochem. Soc. **153**, C787 (2006).

[6] L. Wu and E. Eisenbraun, J. Vac. Sci. Technol. B **25**, 2581 (2007).

[7] Y.K. Chae, Y. Shimogaki, and H. Komiyama, J. Electrochem. Soc. **145**, 4226 (1998).

[8] L. Wu and E. Eisenbraun, J. Electrochem. Soc. **156**, H734 (2009).

[9] C. Jezewski, W.A. Lanford, C.J. Wiegand, J.P. Singh, P.-I. Wang, J.J. Senkevich, and T.-M. Lu, J. Electrochem. Soc. **152**, C60 (2005).

[10] A. Niskanen, A. Rahtu, T. Sajavaara, K. Arstila, M. Ritala, and M. Leskelä, J. Electrochem. Soc. **152**, G25 (2005).

[11] S.M. George, Chem. Rev. **110**, 111 (2010).

[12] M. Leskelä and M. Ritala, Angew. Chem. Int. Ed. Engl. **42**, 5548 (2003).

[13] V.R. Rai and S. Agarwal, J. Vac. Sci. Technol. A **30**, 01A158 (2012).

[14] M. Ritala, K. Kukli, A. Rahtu, P. I. Raisanen, M. Leskelä, T. Sajavaara, and J. Keinonen, Science **288**, 319 (2000).

[15] H.B. Profijt, S.E. Potts, M.C.M. van de Sanden, and W.M.M. Kessels, J. Vac. Sci. Technol. A **29**, 050801 (2011).

[16] S.M. George, A.W. Ott, and J.W. Klaus, J. Phys. Chem. **100**, 13121 (1996).

[17] Y.J. Lee and S.W. Kang, J. Vac. Sci. Technol. A **20**, 1983 (2002).

[18] O.K. Kwon, S.H. Kwon, H.S. Park, and S.W. Kang, J. Electrochem. Soc. **151**, C753 (2004).

[19] G. A. Ten Eyck, J. J. Senkevich, F. Tang, D. Liu, S. Pimanpang, T. Karaback, G. C. Wang, T. M. Lu, C. Jezewski, and W. A. Lanford, Chem. Vap. Depos. **11**, 60 (2005).

[20] E. Langereis, J. Keijmel, M.C.M. van de Sanden, and W.M.M. Kessels, Appl. Phys. Lett. **92**, 231904 (2008).

[21] W.M.M. Kessels, H.C.M. Knoops, S. a. F. Dielissen, a. J.M. Mackus, and M.C.M. van de Sanden, Appl. Phys. Lett. **95**, 013114 (2009).

[22] S.M. George, B. Yoon, and A.A. Dameron, Acc. Chem. Res. **42**, 498 (2009).

[23] M. Dai, J. Kwon, M.D. Halls, R.G. Gordon, and Y.J. Chabal, Langmuir **26**, 3911 (2010).

[24] V.R. Rai and S. Agarwal, J. Phys. Chem. C **112**, 9552 (2008).

[25] V.R. Rai and S. Agarwal, J. Phys. Chem. C **113**, 12962 (2009).

[26] V. Rai, V. Vandalon, and S. Agarwal, Langmuir **26**, 13732 (2010).

[27] V.R. Rai, V. Vandalon, and S. Agarwal, Langmuir **28**, 350 (2012).

[28] R.P. Chaukulkar and S. Agarwal, J. Vac. Sci. Technol. A **31**, 031509 (2013).

[29] M. Milojevic, F.S. Aguirre-Tostado, C.L. Hinkle, H.C. Kim, E.M. Vogel, J. Kim, and R.M. Wallace, Appl. Phys. Lett. **93**, 202902 (2008).

[30] J.L. van Hemmen, S.B.S. Heil, J.H. Klootwijk, F. Roozeboom, C.J. Hodson, M.C.M. van de Sanden, and W.M.M. Kessels, J. Electrochem. Soc. **154**, G165 (2007).

[31] E. Langereis, S.B.S. Heil, H.C.M. Knoops, W. Keuning, M.C.M. van de Sanden, and W.M.M. Kessels, J. Phys. D: Appl. Phys. **42**, 073001 (2009).

[32] M. Ritala, M. Leskela, L. Niinisto, and P. Haussalo, Chem. Mater. **5**, 1174 (1993).

[33] S.B.S. Heil, P. Kudlacek, E. Langereis, R. Engeln, M.C.M. van de Sanden, and W.M.M. Kessels, Appl. Phys. Lett. **89**, 131505 (2006).

[34] D.N. Goldstein, J.A. Mccormick, and S.M. George, J. Chem. Phys. **112**, 19530 (2008).

[35] B.A. Sperling, W.A. Kimes, and J.E. Maslar, Appl. Surf. Sci. **256**, 5035 (2010).

[36] B.A. Sperling, J. Hoang, W.A. Kimes, and J.E. Maslar, Appl. Spectrosc. **67**, 1003 (2013).

[37] F.M. Hoffmann, Surf. Sci. Rep. **3**, 107 (1983).

[38] J.D.E. Mcintyre and D.E. Aspnes, Surf. Sci. **24**, 417 (1971).

[39] R.G. Greenler, J. Chem. Phys. **44**, 310 (1966).

[40] R.G. Greenler, D.R. Snider, D. Witt, and R.S. Sorbello, Surf. Sci. **118**, 415 (1982).

[41] R. Greenler, J. Vac. Sci. Technol. A **12**, 1410 (1975).

[42] H. Pearce and N. Sheppard, Surf. Sci. **59**, 205 (1976).

[43] J. T. Yates Jr. and T. E. Madey, *Vibrational Spectroscopy of Molecules on Surfaces* (Plenum Press, Michigan 1987).

[44] V.M. Bermudez, J. Vac. Sci. Technol. A **10**, 152 (1992).

[45] Y. Song, M. Petty, and J. Yarwood, Vib. Spectrosc. **1**, 305 (1991).

[46] C.T. Elliott, N.T. Gordon, and A.M. White, Appl. Phys. Lett. **74**, 2881 (1999).

[47] P. Griffiths and J.A. De Haseth, *Fourier Transform Infrared Spectroscopy* (John Wiley & Sons, Inc. New Jersey 2007).

[48] S.F. Szymanski, P. Rowlette, and C. A. Wolden, J. Vac. Sci. Technol. A **26**, 1079 (2008).

[49] J.E. Parmeter, J. Phys. Chem. **97**, 11530 (1993).

[50] G.S. Girolami, P.M. Jeffries, and L.H. Dubois, J. Am. Chem. Soc. **115**, 1015 (1993).

[51] D.N. Goldstein and S.M. George, Thin Solid Films **519**, 5339 (2011).

[52] J. Farkas, M.J. Hampden-Smith, and T.T. Kodas, J. Phys. Chem. **98**, 6753 (1994).

[53] J. Farkas, M. J. Hampden-Smith, and T. T. Kodas, J. Phys. Chem. **98**, 6763 (1994).

[54] W. Lin, B.C. Wiegand, R.G. Nuzzo, and G.S. Girolami, J. Am. Chem. Soc. **118**, 5977 (1996).

[55] M.L. Morris, R.W. Moshier, and R.E. Sievers, Inorg. Chem. **1**, 411 (1962).

[56] G. Scarel, J.-S. Na, B. Gong, and G.N. Parsons, Appl. Spectrosc. **64**, 120 (2010).

[57] M.T. Seman, D.N. Richards, P. Rowlette, and C. A. Wolden, Chem. Vap. Depos. **14**, 296 (2008).

[58] J. Kwon, M. Dai, M.D. Hills, and Y.J. Chabal, Chem. Mater. **20**, 3248 (2008).

[59] Y. Wu, E. Garfunkel, and T.E. Madey, J. Vac. Sci. Technol. A **14**, 1662 (1996).

[60] J. A. Kelber, C. Niu, K. Shepherd, D. R. Jennison, and A. Bogicevic, Surf. Sci. **446**, 76 (2000).

[61] Q. Fu, T. Wagner, and M. Rühle, Surf. Sci. **600**, 4870 (2006).

[62] C. Niu, K. Shepherd, D. Martini, J. Tong, J. A. Kelber, D. R. Jennison, and A. Bogicevic, Surf. Sci. **465**, 163 (2000).

[63] F. Wu, G. Levitin, and D.W. Hess, ACS Appl. Mater. Interfaces **2**, 2175 (2010).

[64] L. Andrews and X. Wang, J. Am. Chem. Soc. **125**, 11751 (2003).

[65] J.C. Warf and W. Feitknecht, Helv. Chim. Acta **33**, 613 (1950).